ABSTRACT

BULLOCK, NOAH WILLIAM. Digital Pulse Pileup Deconvolution with Cerium (III) Bromide Scintillator. (Under the direction of Dr. John Mattingly.)

Gamma-ray spectroscopy in high count rate applications can be challenging with inorganic scintillators, due to their typical characteristically slow scintillation light emission rates, which contributes to pulse pile up that is difficult to mitigate using analog pulse processing. A relatively new inorganic scintillator, cerium (III) bromide ($CeBr_3$) has very fast timing for medium resolution, room temperature spectroscopic applications. It has a density of 5.2 g/cm^3 and emits approximately 68,000 photons per MeV of energy deposited, which is nearly twice as bright as sodium iodide. Using a Scionix 38.1mm (diameter) $\times$ 38.1mm (long) $CeBr_3$ detector which exhibits good resolution (3.9% at 662 keV) and fast timing (17 ns scintillation decay time), the ability to collect gamma-ray spectra in high count rate environments is possible. Using an XIA PIXIE-500, 500 megasample per second, 12-bit digitizer to digitally sample the $CeBr_3$ detectors anode signal, a deconvolution algorithm was developed that is able to deconvolve piled up pulses within nanoseconds of other pulses. Using an analytical model of the expected pulse shape to deconvolve overlapping digitized anode pulses, the algorithm was able to deconvolve pulses and maintain good resolution with little energy broadening in high count rate applications. Starting with a 5μCi ^{137}Cs source (gamma-rays incident on the detector $\approx 1.02 \times 10^3 \gamma/s$) at 5 inches we found our system could obtain an energy resolution of 4.19% (at 662 keV). Using a 4mCi ^{137}Cs source (gamma-rays incident on the detector $\approx 1.44 \times 10^5 \gamma/s$) at 1 foot, significant degradation was observed in the analog pulse height spectrum (PHS), while our deconvolution algorithm produced an accurate PHS with pulse time resolution of a few nanoseconds and energy resolution of 4.23%(at 662 keV). This validates the ability of the algorithm to use the digitized anode signal and produce accurate pulse height spectra.

Digital Pulse Pileup Deconvolution with Cerium (III) Bromide Scintillator

by
Noah William Bullock

A thesis submitted to the Graduate Faculty of
North Carolina State University
in partial fulfillment of the
requirements for the Degree of
Master of Science

Nuclear Engineering

Raleigh, North Carolina

2014

APPROVED BY:

_____   _____
Dr. Wolfgang Hennig   Dr. Robin Gardner

_____
Dr. John Mattingly
Chair of Advisory Committee

BIOGRAPHY

I received my BS in Physics at the College of Charleston in May of 2012. I was accepted to the nuclear engineering graduate program at North Carolina State University in August of 2012.

DEDICATION

I want to dedicate this work to all of my brothers and sisters that are in uniform, have served in uniform, or gave their lives while serving. Thank you for what you do, and have done for all of us. Hoo-Yah.

I also am dedicating this to my family. Thank you for...everything. I could never sum up in a few words what you mean to me.

ACKNOWLEDGEMENTS

I want to thank my advisor, Dr. John Mattingly for his guidance and support throughout my graduate career and research. Thank you for giving me the tools to succeed and the knowledge to use those tools effectively.

I want to thank my thesis committee members, Dr. Wolfgang Hennig and Dr. Robin Gardner. Dr. Hennig's insight and knowledge about the Pixie-500 was very important to utilize the equipment as efficiently and effectively as possible. Dr. Gardner's wealth of knowledge in high count rate applications and pervious work in pulse piled up deconvolution algorithms was invaluable to this project.

I want to thank Jack Linkous and Kyle Weinfurther for all of their help with learning MATLAB and in code writing skills. I started this endeavor never having opened MATLAB before, but with their help I was able to utilize the software and become very proficient in its use.

I also want to thank Kelsey Reamer and Kalene Hanson for the characterization of our cerium (III) bromide and sodium iodide detectors, excellent work.

This research was partly supported from a grant from the nuclear regulatory commission, and I would like to thank them for the support.

TABLE OF CONTENTS

LIST OF TABLES

LIST OF FIGURES

Chapter 1

Introduction

1.1   Motivation

In the field of nuclear engineering and physics, precise and accurate gamma-ray spectra are essential for moving research and technology forward. In the realm of high count rate environments this becomes very difficult. Whether it is analog or digital pulse processing there are always limitations of the equipment and/or techniques. As count rates increase in a detector, the probability of multiple gamma-ray interactions close in time increases. In analog pulse processing systems these manifest themselves in the spectrum as sum peaks or sometimes as gain shifts. These can be dealt with through pileup rejection circuitry, but in high count rate environments this circuitry can dramatically reduce the efficiency of the spectroscopic system.

The goal of this work was to develop a deconvolution algorithm that uses nonlinear regression on a digitized photomultiplier tube (PMT) anode signal from a $CeBr_3$ inorganic scintillator to minimize spectral distortion in very high count rate environments. A thallium activated, sodium iodide (NaI(Tl)) inorganic scintillator was used as a baseline to evaluate $CeBr_3$. This provided a measurable demonstration of the capabilities of $CeBr_3$ over a slow scintillator material, and the effectiveness of digitizing the $CeBr_3$ anode signal to create a pulse height spectrum (PHS) opposed to collecting analog PHS. The motivation to create this algorithm was due to significant

1
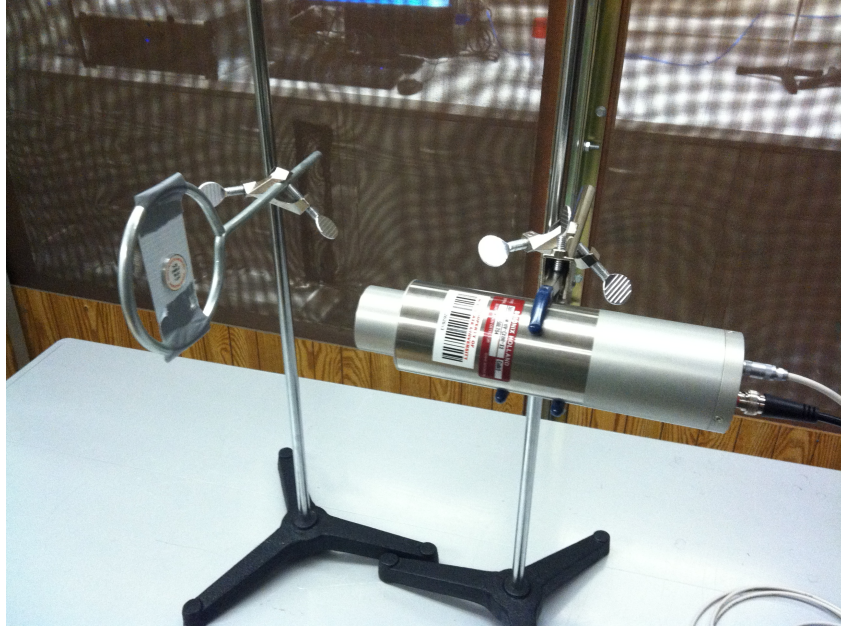
Figure 1.1: CeBr$_3$ with calibration source setup for collecting PHS.

spectral distortion caused by piled-up pulses in high count rate environments when standard multichannel analyzers (MCA) analog-to-digital (A/D) converters are used. Fig. 1.1 shows the setup of the 5μCi ^{137}Cs analog MCA experiment using our CeBr$_3$ detector.

Fig. 1.2 shows the effects of these spectral distortions when the analog PHS of a 4mCi ^{137}Cs was taken. The count rate seen by our CeBr$_3$ detector using a 5μCi ^{137}Cs at 5 inches was approximately 1.02×10^3 $\frac{\gamma}{s}$, where a 4mCi ^{137}Cs, with a source-to-detector distance of 3 feet was approximately 1.61×10^4 $\frac{\gamma}{s}$. The increased counts above the 662 keV peak (channel 850) is indicative of pulse pileup. The coincidence peak from two 662 keV gamma-rays interacting very close in time (between channels 1600 to 1800) is characteristic from PHS in high count rate environments with characteristic gamma-ray peaks emitted from a source. The backscatter peak seen around channel number 230 was due to the farther source-to-detector distance that created a higher number of backscattered gamma-rays that interacted inside the detector.

With a thorough study of the nuclear pulse processing, analytical models of the time-

2
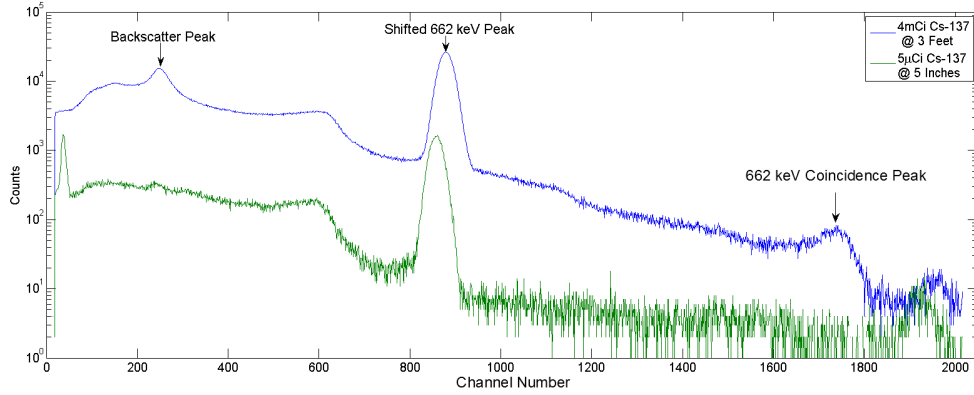
Figure 1.2: Comparison of analog PHS taken from a 38.1mm (diameter) $\times$ 38.1mm (long) CeBr$_3$ of a 5μCi ^{137}Cs at 5 inches and a 4mCi ^{137}Cs at 3 feet. Spectral distortion was shown, as well as a coincidence peak from the 662 keV gamma-rays (between channels 1600 to 1800).

dependent anode pulse shape can be used on digitized waveforms of the anode signal to deconvolve multiple overlapping pulses and mitigate these spectral distortions.

1.2 Prior Work in the Field

In the field of fusion reactors, gamma-rays with counting rates up to 10^6 counts per second (cps) are starting to be used for diagnosis of reactions[1]. For these applications scintillation compounds with fast decay times are needed. For Nocente's research a cerium activated, lanthanum bromide (LaBr$_3$(Ce)) inorganic scintillator was used in conjunction with a 400 megasample per second (MS/s). 14-bit digitizer that sampled the non-shaped, pre-amplified signal[1]. They postulated that the pulse shapes do not change, only the arrival times of the pulses, amplitude of the pulses, and the baseline change. They used a model that fits the pulse shape, but only due to mathematical equation that contains values that have no physical properties of the detector or PMT (discussed later in Section 4.5). Nocente's algorithm was able to measure gamma-ray spectra without degradation in the energy resolution up into the range of 2.6×10^6 cps.

Another area where high count rates are usually seen is in active neutron interrogation ap-

3

plications. Sources of neutrons can be from the spontaneous fission of Califorium-252 (^{252}Cf), Americium-Beryllium (AmBe) α-n reaction source, or deuterium-deuterium (D-D) and deuterium-tritium (D-T) generators that can output up to 10^{15} neutrons per second[2]. ^{252}Cf and AmBe sources constantly emit neutrons in a spectrum of energies, while D-D and D-T generators emit mono-energetic neutrons when turned on. These generators usually operate in a pulsed mode like in the work of H. Yang where the accelerator produced 5μs pulses with a maximum repetition rate of 600 Hz[3]. In homeland security, active neutron interrogation gamma-ray spectroscopy is becoming more widely used for the detection of special nuclear material (SNM)[3]. These pulsed neutrons create bursts of gamma-rays due to interactions with nuclei in very short pulse periods. To accumulate accurate spectra from a sample, these gamma-rays need to arrive at times not overlapping with other gamma-ray interactions. This is usually not possible, so techniques need to be developed to deconvolve piled up pulses with detectors that are resolved enough to accurately identify important peaks associated with SNM and/or other important isotopes.

In work done by H. Yang in 2008, they used the premise that the recorded signal is a convolution of the input signal and system response function[3]. Once they determined the system response function, they could deconvolve individual pulses. Their analysis assumed that noise is negligible. Their work was able to digitize a cerium activated, lanthanum chloride ($LaCl_3(Ce)$) anode signal with a 200 MS/s, 12-bit resolution digitizer at a rate greater than 10^6 cps with no dead time and no spectral shifts.

Another area of industry where high count rate environments are encountered is oil well logging. When boreholes are drilled, tools are lowered into the boreholes to test compositions on the surrounding environment. Conventional gamma-gamma density (GGD) logging tools use a ^{137}Cs source to collect spectra, while newer neutron-gamma density (NGD) tools have been developed that utilize pulsed neutron sources (D-D / D-T generators) to do active neutron interrogation[4]. This method collects gamma-rays produced from the inelastic interactions from fast neutrons for density measurements[4]. In each case, large gamma-ray fluxes from

4

neutron scattering and absorption can cause shifted spectra that create inaccurate spectral features due to pileup and gain shifts. The use of the NGD allows the deployment of this tool without the restrictions caused by the radioactive ^{137}Cs due to the use of D-D or D-T generators. In work done by Weijun Guo, et al, they used the assumption that the scintillator decay time and PMT decay time are "somewhat" constant and can be expressed as the average of many measured results. They digitized the shaped, pre-amplified signal from a Lu_2SiO_5 (LSO) scintillator detector with a 10 MS/s, 8-bit resolution digitizer. Guo utilized an analytical model that was derived by assuming the PMT was a simple RC circuit. Guo used a differential pulse discriminator to initially determine amplitude and pulse arrival times, then he used a least-squares algorithm to fit the parameters to the pulse shape. Guo et al. used a Monte Carlo radiation transport code that assumed no dead time in the digitizer to show that this method was able to deconvolve piled-up pulses and maintain spectral resolution at 4×10^6 cps[5].

1.3   Contributions of this Research

This research utilizes different aspects of the previous research to develop a new algorithm that will be more robust and able to deconvolve digitized pulses in high count rate environments accurately with the fast CeBr$_3$ scintillator. Previous research in scintillator pulse shapes have assumed that pulse shapes are constant and only vary in amplitude, arrival times, and baselines. Our approach uses an analytical model with multiple pulse parameters that will more accurately describe pulse shapes. It was shown that anode pulse shapes do in fact differ with pulse amplitudes, so treating scintillator and PMT decay times is needed for fitting a more accurate pulse shape. With slower scintillators it was found that individual pulses had two baselines, one before the pulse and one after the pulse. These additions allows for a more robust description of the pulse shape which will allow for more accurate determinations of the incoming gamma-ray energies.

Our deconvolution algorithm adopted ideas from previous works and includes new techniques and tools to include:

- CeBr$_3$: Ideal for high count rate environments,

  - Fast scintillation decay time (17 ns),

  - Good resolution (3.9% at 662 keV),

  - No intrinsic radioactivity,

  - Anode pulse widths $\approx$ 150 ns (NaI(Tl) $\approx$ 1050 ns),

- Directly digitizes the anode pulse,

  - Bypasses any pre-amplification and amplification pulse shaping or gain shifts,

- 500 MS/s, 12-bit digitizer

  - Voltage resolution in steps of 0.48mV,

  - Timing resolution of 2 ns,

- Varying scintillation & PMT decay times

- Pre- & post-trigger baselines

- Pulse detection by differentiation

  - Can identify pulses separated by $\approx$ 20 ns,

- Recursive fitting

  - Re-examines residuals for "missed" pulses

which used the 500MHz, 12-bit digitizer on our CeBr$_3$ detector. These techniques were applied to a generalized anode pulse shape model of the digitized anode signals.

6

Chapter 2

Theory

2.1 Scintillation Detectors

Inorganic scintillation detectors have two important common requirements that make them suitable for detecting gamma-rays. These compounds typically have high photoelectric absorption cross-sections, and the compound has to fluoresce in the visible spectrum (typically in the blue wavelengths $\approx 400\ nm$) so these photons can be detected by a photocathode. To ensure photoelectric absorption of these gamma-rays, compounds should have at least one high atomic number (high-Z) constituent. To ensure the emission of a photon from the gamma-ray absorption, compounds must have band levels that will allow electrons in the crystal to jump into the conduction band, then relax through an activator excited state that allow for the emission of photons able to be absorbed by the photocathode, before relaxing completely into the valence band again. This process is shown in Fig. 2.1.

$CeBr_3$ is a self-activated scintillator[6]. Visible photons are emitted through a 5d to 4f level transition in the cerium (Ce)[6]. (Discussed in Section 2.1.2). Fig. 2.2 shows the process for $CeBr_3$.

Although there are many factors that impact a scintillators energy resolution, in general a scintillation materials energy resolution depends on the light yield emitted from the crystals
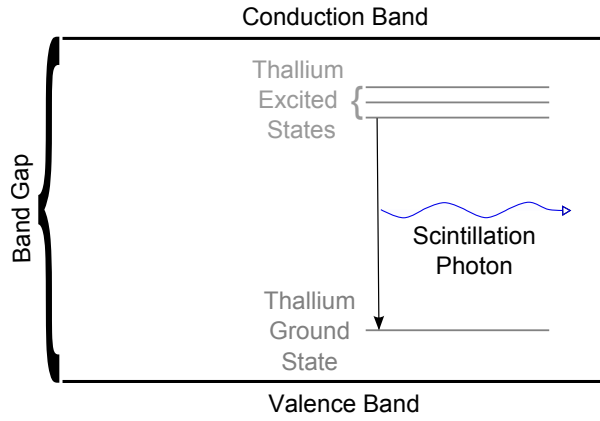
Figure 2.1: NaI(Tl) inorganic scintillation crystal electron band structure.
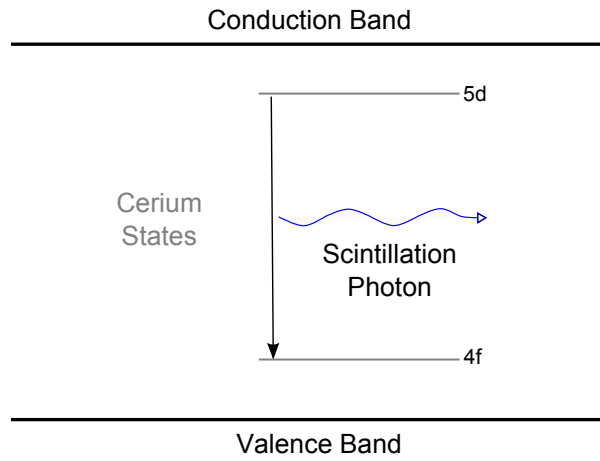
Figure 2.2: CeBr$_3$ inorganic scintillation crystal electron band structure.

following energy deposition by incoming gamma-rays. Higher light yields correspond to a higher energy resolution of the crystal. Since radiation counting statistics follow a Poisson distribution, its uncertainty is the square-root of the number of counts. This means, as NaI(Tl) emits approximately $38,000\pm195$ photons/MeV while the more resolved $CeBr_3$ emits $68,000\pm261$ photons/MeV, NaI(Tl) has a higher proportional uncertainty in energies from the incoming gamma-rays which equates to a lower energy resolution. The relaxation time of the crystal's fluorescent states controls the width of the light pulse. Scintillation compounds with fast relaxation times correspond to fast scintillators and compounds with slower relaxation times are considered slow scintillators.

The basic process of detecting a gamma-ray is shown in Fig.2.3. An incoming gamma-ray interacts with the scintillation material and is absorbed. Due to the atoms' crystalline structure, electrons are excited into the conduction band. As the electron de-excites, it cascades through the activator excited states until it emits scintillation photons and then relaxes back into the valence band. These scintillation photons then interact with the photocathode, where the incoming photons are absorbed and eject one or more photoelectrons about 20-30% of the time due to quantum efficiency[6]. These electrons are then accelerated towards the first dynode in the PMT. Electron multiplication occurs at each dynode by sequentially increasing the potential across the dynodes of the PMT until the last stage where the electrons are swept up by the anode and create a current flowing through the anode. The total charge at the anode is directly proportional to the incoming energy of the absorbed gamma-ray.

9
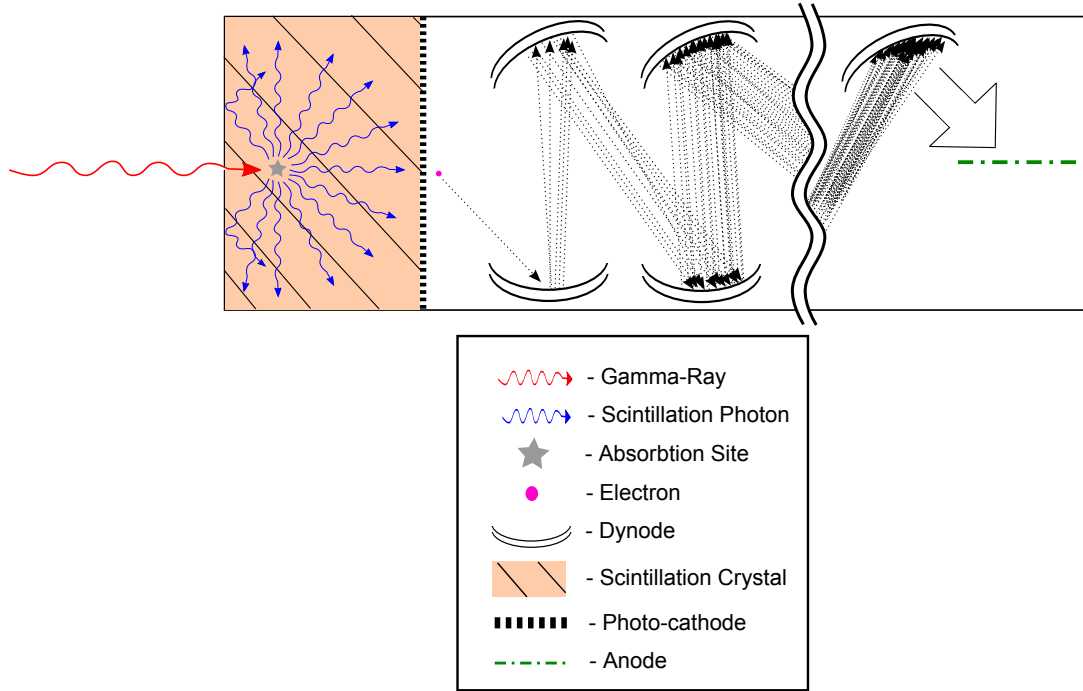
Figure 2.3: Gamma-ray detection through scintillation crystal.

2.1.1 Thallium-Activated Sodium Iodide (NaI(Tl))

Sodium iodide (NaI) doped with a thallium (Tl) activator is one of the most common and inexpensive inorganic scintillation detectors available. It is used as a baseline that other detectors are compared to. NaI has a relatively high average atomic number ($Z_{avg} = 32$) which gives the compound a high photoelectric absorption cross-section. Tl concentrations effect the prompt photon emission decay times. Low thallium concentrations gives the compound a scintillation decay time of around 350 ns, where thallium concentrations of 0.1% to 0.5% decrease the scintillation decay time to approximately 230 ns[7]. The compound emits photons that peak at a wavelength of 415nm and emits approximately 38,000 photons per MeV of energy deposited[6]. NaI(Tl) exhibits a non-linearity in light yield to deposited energy between 122keV to 1274 keV of about 9%[8]. Characterization of our 50.8mm (diameter) X 50.8mm (long) detector used during this research showed a resolution of 6.4% at 662 keV. Our detector also showed a typical

www.manaraa.com

pulse width of approximately 1050 ns. This makes NaI(Tl) a good choice for medium resolution spectroscopy. NaI(Tl) was chosen as a baseline scintillator for these experiments.

One drawback of NaI(Tl) is that is has some longer lived phosphorescence states that cause an "afterglow," and in high count rate environments these can cause the constant glowing of the crystal. The intermediate phosphorescence states of NaI(Tl) have a decay time of about 0.15 s that contribute to about 9% of the photoelectric yield[9]. Another phenomenon associated with high count rate environments occurs in the PMT. As the amount of electrons increase from each dynode, it can cause a gain shift due to the potential difference at different dynodes[10]. Even though this detector is not suited for high count rate environments, it will be used as a baseline detector since most of its characteristics are very well documented. Appendix C shows the characterization of the NaI(Tl) detector used in these experiments. It also contains some of the characteristics of the ET Enterprises 9266B PMT coupled to it.

2.1.2 Cerium(III) Bromide (CeBr$_3$)

Cerium (III) bromide is a self-activated crystal that has become more readily available and is showing impressive characteristics for room temperature medium resolution spectroscopy. CeBr$_3$ has a relatively high average atomic number (Z_{avg} = 40.75). The properties of this compound give it a Ce^{3+} which is the "luminescence center for the scintillation process[8]." This compound emits photons that have a peak wavelength of 371nm due to Ce^{3+} 5d to 4f transition, emits approximately 68,000 photons per MeV (i.e. this is approximately twice as bright as NaI(Tl)), has an estimated rise time of 0.1 ns, and has a very fast scintillation decay time of 17 ns[8]. CeBr$_3$ shows a non-linearity in light yield to deposited energy between 122 keV to 1274 keV of about 4%[8]. Characterization of our 38.1mm (diameter) X 38.1mm (long) detector used for this research showed a resolution of 3.9% at 662 keV. Our detector showed a typical pulse width of approximately 150 ns. Fig. 2.4 shows the difference in pulse widths of a CeBr$_3$ pulse and NaI(Tl) pulse with similar amplitudes. Due to its resolution and fast timing, CeBr$_3$ makes an excellent choice for medium resolution spectroscopy, and its fast scintillation decay time

11
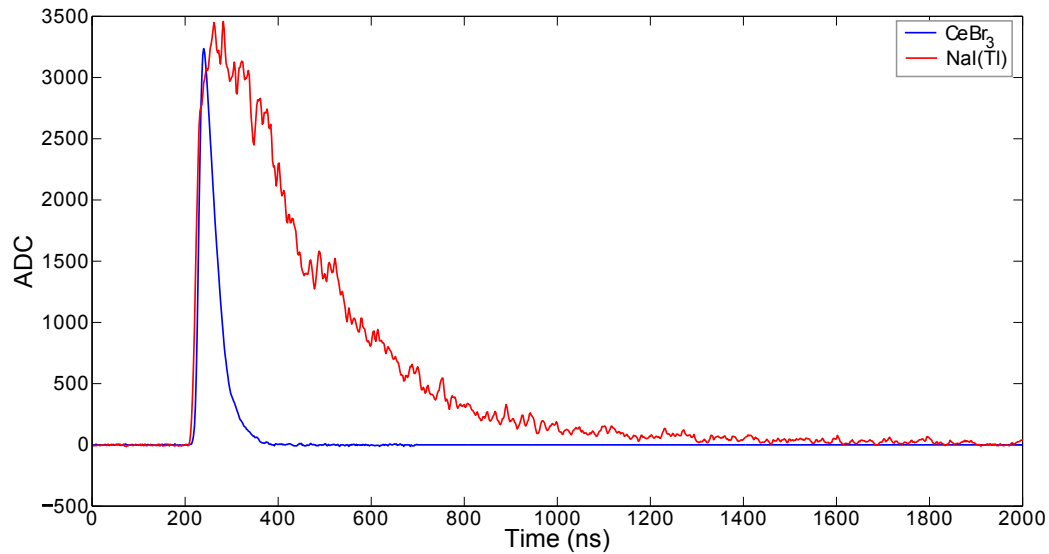
Figure 2.4: Pulse width comparison between CeBr$_3$ and NaI(Tl).

makes it well suited for high count rate applications. Appendix B shows the characterization of the detector used in these experiments. It also contains some of the characteristics of the Hamamatsu R6231 PMT coupled to it.

2.2 Electronics

2.2.1 Analog Pulse Processing

Analog pulse processing is a very effective and efficient way to collect pulse height spectra (PHS) from radionuclei. The average pulse processing time is $< 2\mu s$[11], which works very well in low to medium count rate environments. Once high count rates saturate the system, pulse pileup will distort the spectrum and system dead time will degrade the efficiency of the system. Fig. 2.5 shows the general pulse shape at each stage in the analog pulse processing system. At point 1, a gamma-ray interacts with the detector. At point 2, electron multiplication through the PMT creates an anode pulse millivolts in amplitude with varying rise and decay times

12
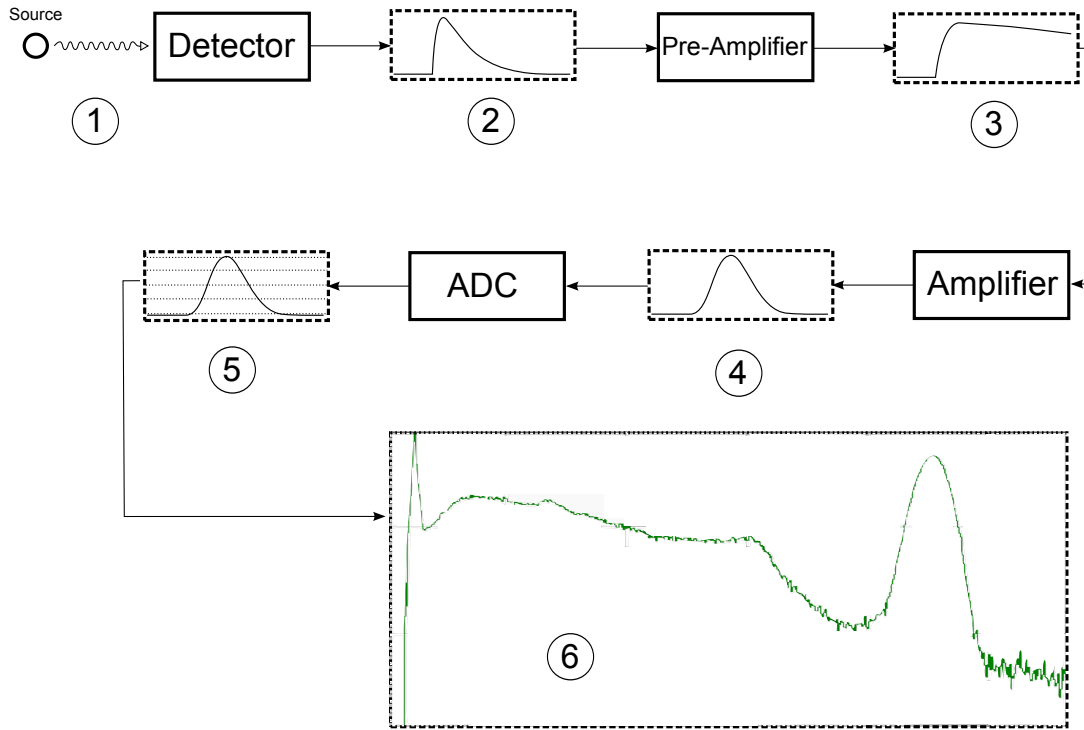
Figure 2.5: Analog pulse processing system with pulse shape at each stage.

depending on the scintillation decay time of the detector being used and the PMT decay time. At point 3, the pre-amplifier boosts the anode signal and has a shaping time long enough to allow complete charge collection ($\approx 200\mu$s). At point 4, the amplifier boosts the signal amplitude into the several-volt range and has varying shaping times in the microsecond range which gives the pulse an average width in the tens-of-microseconds range. At point 5, the multichannel analyzer (MCA) converts the peak analog signal voltage to a peak capture analog-to-digital conversion (ADC) value. The last stage at point 6, all of the digital ADC values are binned according to their value to build a pulse height spectrum (PHS).

2.2.2 Digitizer

The general operation of a digitizer is to sample an incoming signal and convert it into a digital value that can be recorded for post-processing. The digitizer waits for an incoming signal to

exceed a threshold level. Once this threshold has been passed, the digitizer samples the signal for a specific window length (set by the user) before passing the data to the buffer. By digitizing the incoming anode signal from a detector, different methods can be employed to get the area under the pulse, which is proportional to the total charge collected from the PMT. These values are then binned, and a PHS can be built from all the digitized pulses.

This work was done using an XIA Pixie-500. It is a 12-bit A/D converter (displayed in units of ADC) with a 500 MS/s sampling rate[12]. The Pixie-500 has a dynamic range of 2V, and with 12-bit resolution can resolve input voltages in steps of 0.48mV[13]. This makes the Pixie-500 a very suitable tool to digital sample the anode pulse from fast detectors like CeBr$_3$. For more information about the Pixie-500 please consult Ref.[12, 13].

2.3   Pulse Pileup

In high count rate environments, a common problem encountered in analog pulse processing is pulse pileup. Pulse pileup occurs when multiple gamma-rays interact within the detector in a short time window that causes the anode signal to contain multiple pulses that are sent to the pre-amplifier. Fig. 2.6 shows two incoming pulses and Fig. 2.7 has three incoming pulses. The voltage pulse measured by the MCA would be the sum of the total voltages of all the pulses after amplification. Fig.2.8 clearly shows the effect to a PHS due to pulse pileup. The spectrum in blue was from a 5μCi ^{137}Cs (low count rate), and the green spectrum was from a 4mCi ^{137}Cs (high count rate). In the 4mCi spectrum a shifted 662 keV peak and high counts above the 662 keV peak show the effects of pulse-pileup in the detector.

To mitigate the PHS shifts and pileup due to high count rates, the individual pulses must be identified and deconvolved so each individual pulse can be evaluated correctly. To do this an analytical model was used that will allow a fitting algorithm to fit pulse parameters so an accurate PHS can be created.

14
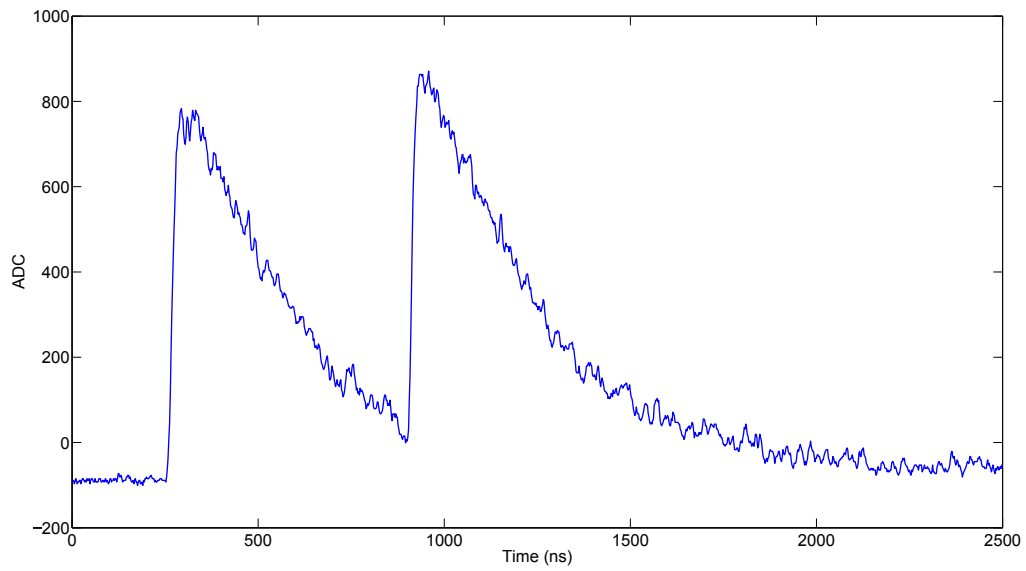
Figure 2.6: Two piled pulse pulses from a NaI(Tl) detector.
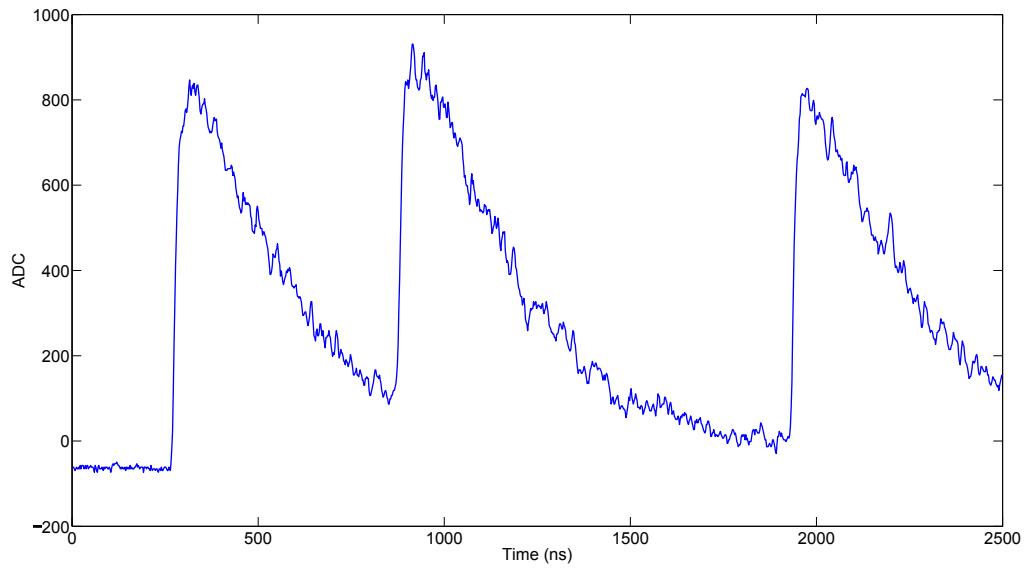
Figure 2.7: Three piled pulse pulses from a NaI(Tl) detector.

15
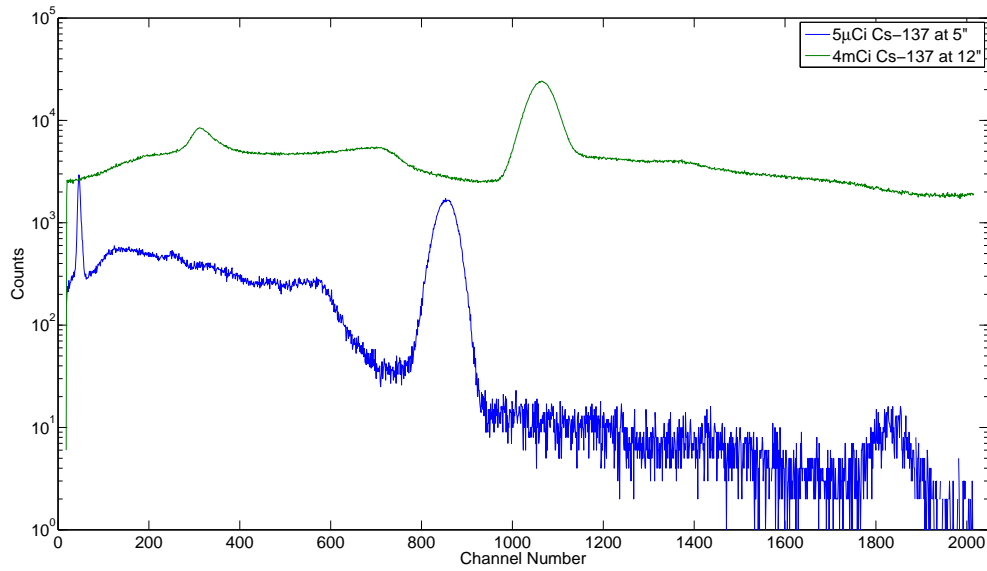
Figure 2.8: Showing the effects of pulse pileup of a ^{137}Cs in an NaI(Tl) analog pulse processing system.

2.4 Pulse Shape Modeling

For the proper fitting of pulses to determine pulse characteristics, an analytical model was used. With an understanding of the dynamics of scintillation and electron multiplication in the PMT, an equation can be developed that describes the pulse shape needed for pulse fitting.

2.4.1 Double Exponential Pulse Shape Model

Since the PMT is a series of parallel resistors (R) and capacitors (C), a simple idealized parallel RC circuit can be used to derive the current at the anode as shown in Fig. 2.9.

Starting with this simple equation[6]:

$$i(t) = i_0 e^{-\lambda_r t}, t > 0 \tag{2.1}$$

where $\lambda_r = {}^1/\tau_r$, and τ_r is the scintillation decay time, t is the pulse arrival time, and i_0 is the

16
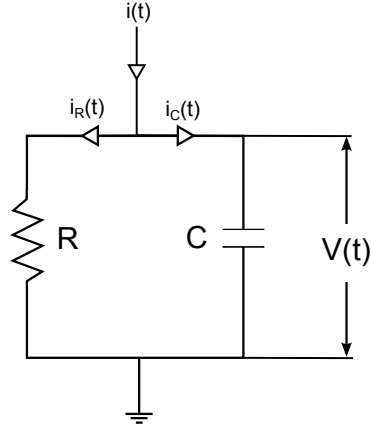
Figure 2.9: Simplified parallel RC circuit diagram of the PMT.

initial current. To get the total charge collected (Q), $i(t)$ needs to be integrated:

$$Q = \int_0^\infty i(t)dt \rightarrow Q = \frac{i_0}{\lambda_r}, \tag{2.2}$$

which now gives the value for i_0, and Eq. 2.1 can be written as:

$$i(t) = \lambda_r Q e^{-\lambda_r t}. \tag{2.3}$$

Since the current flowing from the anode is the sum of the current flowing through the capacitors and resistors, the total current is written as:

$$i(t) = i_R + i_C, \tag{2.4}$$

and this can be re-written as:

$$i(t) = C\frac{dV(t)}{dt} + \frac{V(t)}{R}. \tag{2.5}$$

Now Eq.2.3 can be inserted into Eq.2.5 can rearranged into:

17

$$\frac{\lambda_r Q}{C} e^{-\lambda_r t} = \frac{dV(t)}{dt} + \frac{V(t)}{RC}. \tag{2.6}$$

Eq.2.6 can now be solved with the initial condition at $t = 0$, $V(0) = 0$, which is:

$$V(t) = A \frac{\lambda_r}{\lambda_r - \lambda_f} (e^{-\lambda_f t} - e^{-\lambda_r t}), \tag{2.7}$$

where $A = Q/C$, $\lambda_f = 1/\tau_f$, and $\tau_f = RC$ which is the PMT decay time. To be able to fit a multiple pulses with different arrival times a Heaviside step function was added to the pulse shape model. Also, a pre- and post-trigger baseline was added to the pulse shape model shown in Eq.2.8:

$$V(t) = H(t) A \frac{\lambda_r}{\lambda_r - \lambda_f} (e^{-\lambda_f t} - e^{-\lambda_r t}) + (1 - H(t))B_- + H(t)B_+, \tag{2.8}$$

where B_- is the pre-trigger baseline value, and B_+ is the post-trigger baseline. $H(t)$ is the Heaviside step function:

$$H(t) = \int_t^\infty \delta(t)dt \ = \ \begin{cases} 1 & t \geq 0 \\ 0 & t < 0 \end{cases} \tag{2.9}$$

where $\delta(t)$ is the Dirac delta function. Since my research utilized MATLAB, it used a different form of the Heaviside step function shown in Eq. 2.10.

$$H(t) = \begin{cases} 1 & t > 0 \\ 1/2 & t = 0 \\ 0 & t < 0 \end{cases} \tag{2.10}$$

Fig. 2.10 shows the analytical model described in Eq. 2.8 fit to a single NaI(Tl) anode pulse. The analytical model with the correct pulse parameters closely fits the anode pulse. Fig. 2.11 shows the analytical model described in Eq. 2.8 fit to a single CeBr$_3$ anode pulse. Although

18
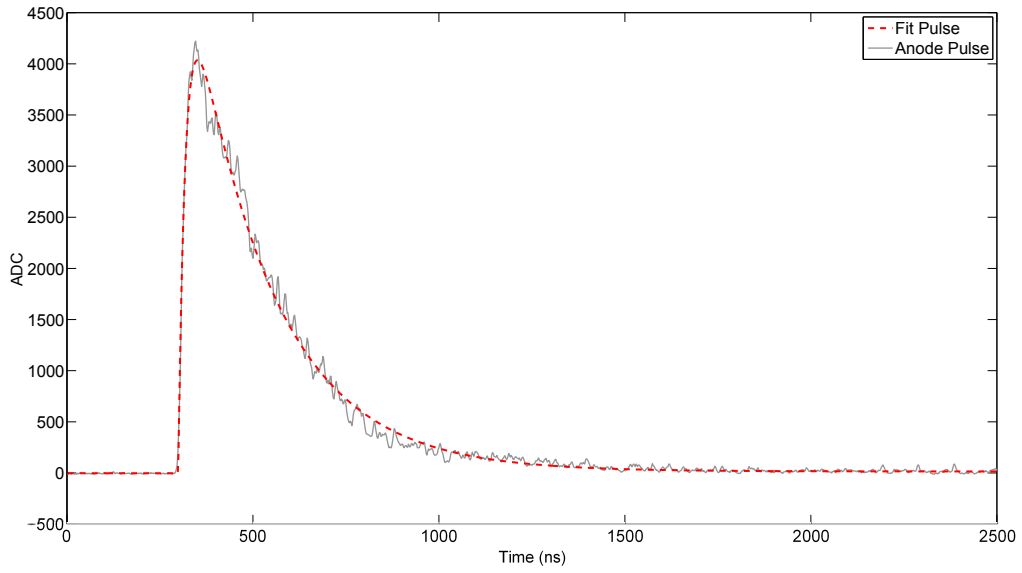
Figure 2.10: Single NaI(Tl) anode pulse fit to the analytical model described in Eq. 2.8.
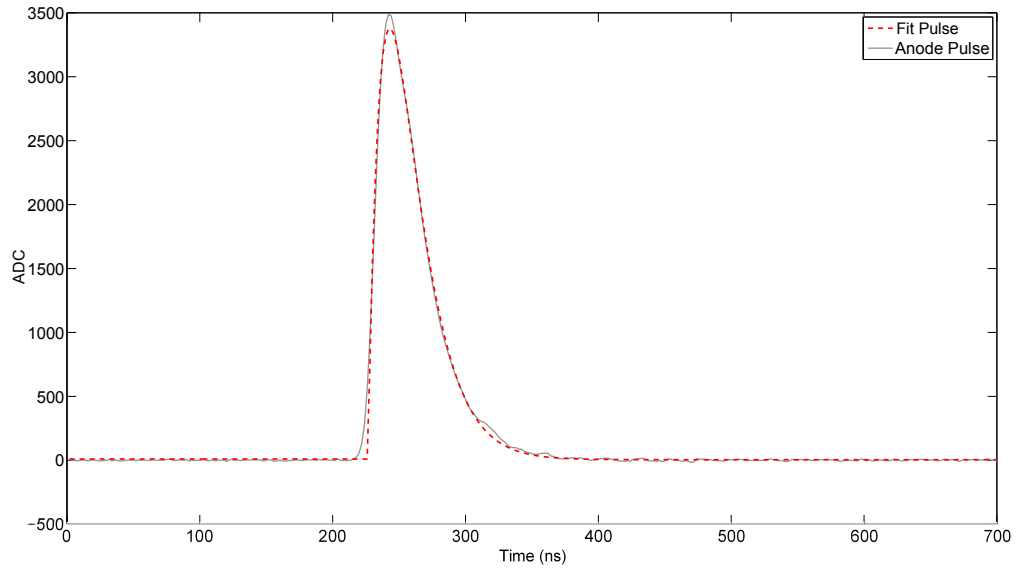
Figure 2.11: Single CeBr$_3$ anode pulse fit to the analytical model described in Eq. 2.8.

19

this analytical model's fit is optimal, CeBr$_3$ appears to have an exponential rise of the leading edge of the anode pulse which is not fully described by our analytical model.

Since the purpose of this work is to be able to fit multiple pulses in one trace window, models need to be created to do this. This was done by the superposition of multiple pulses given by Eq.2.11:

$$V_n(t) = H_n(t - t_n)A_n \frac{\lambda_{r_n}}{\lambda_{r_n} - \lambda_{f_n}}(e^{-\lambda_{f_n}(t-t_n)} - e^{-\lambda_{r_n}(t-t_n)}).$$ (2.11)

When Eq. 2.11 is incorporated with the pre- and post-trigger baseline values it becomes Eq. 2.12:

$$V(t) = (1 - H(t - t_1))B_- + H(t - t_1)B_+ + \sum_{n=1}^{N} V_n(t),$$ (2.12)

where N is the total number of pulses in a trace window. Now Eq.2.12 can fit multiple pulses per trace window and fit each pulses individual parameters. The pre- and post-trigger baseline is only evaluated from the time of the first pulse (t_1). Fig.2.12 shows multiple pulses in a NaI(Tl) trace window and Fig.2.13 is multiple pulses in a CeBr$_3$ trace window.
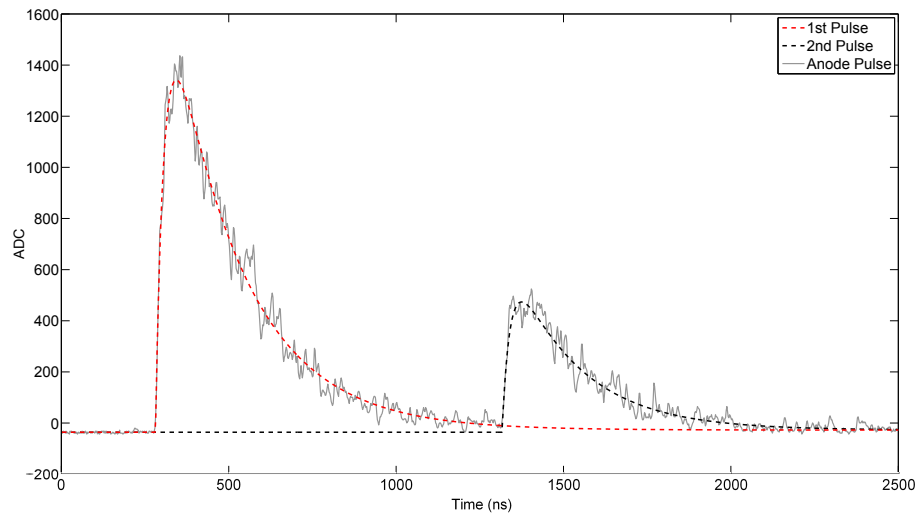
Figure 2.12: NaI(Tl) trace window fit to the analytical model that describes the superposition of multiple pulses as shown in Eq. 2.12.
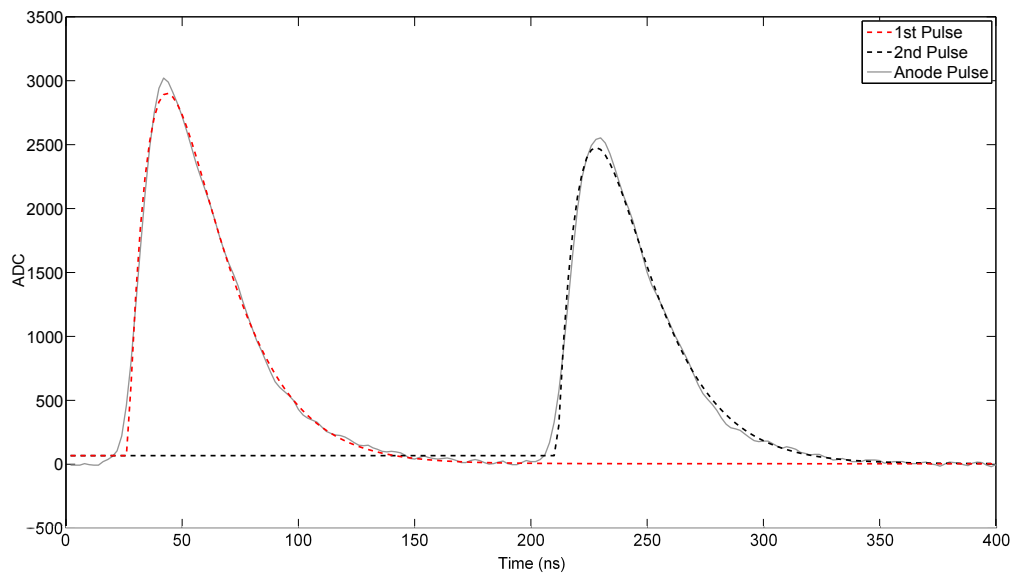
Figure 2.13: CeBr$_3$ trace window fit to the analytical model that describes the superposition of multiple pulses as shown in Eq. 2.12.

21

2.4.2 Pulse Height Spectrum

The PHS is final result of using the fitting algorithm to deconvolve multiple pulses in a trace window. In high count rate environments analog nuclear pulse processing systems can use rejection circuitry to omit piled up pulses. Without this rejection circuitry being used piled up pulses can cause shifts in the spectra and accidental coincidence sum peaks. In some cases the count rate can become so high that pulse pileup dominates the spectrum and destroys the accuracy of the spectrum.

By digitizing the anode pulse and using fitting algorithms, pulse parameters can be extracted and utilized to build a PHS that eliminates pileup. Having an analytical model of these pulses, degradation of the spectra can be mitigated by correcting spectrum distortion through deconvolution of piled up pulses. Since the PHS is a histogram of the charge collected (Q) values from each pulse, Eq.2.8 can be integrated to solve for Q:

$$Q_n = \int_0^\infty \frac{V_n(t)}{R} dt \propto \int_0^\infty V_n(t) dt, \tag{2.13}$$

which becomes:

$$Q_n \propto A_n \frac{\lambda_{r_n}}{\lambda_{r_n} - \lambda_{f_n}} \left(\frac{1}{\lambda_{f_n}} - \frac{1}{\lambda_{r_n}} \right), \tag{2.14}$$

$$Q_n \propto A_n \tau_{f_n}. \tag{2.15}$$

From Eq.2.15 a PHS can be built from the individual pulses fit amplitudes (A_n) and PMT decay times (τ_{f_n}).

2.5 Floating Averaging Low Pass Filter

A simple floating average low pass filter was applied to trace windows to smooth out radio frequency noise on the anode signal. In the analog nuclear pulse processing system this phe-

nomenon will usually just manifest itself as an increased baseline that shifts the spectra a small amount. Due to the digitizer taking the anode pulse directly, this noise can be more problematic and give false triggers. Because of this, a filter was written to minimize this effect. This filter is shown below:

$$Y(t) = \frac{1}{2T+1} \sum_{i=t-T}^{t+T} y(i), \tag{2.16}$$

where $Y(t)$ is the filtered pulse value, $y(i)$ is the original pulse value, t is the time step value in the trace, and T is the half-width of the filter. Fig. 2.14 shows a digitized NaI(Tl) anode pulse with the filtered pulse overlaid. Due to the noise in the NaI(Tl) we used a 41 point ($T = 20$) floating average filter. Fig.2.15 shows a digitized CeBr$_3$ anode pulse overlaid with the filtered pulse. The CeBr$_3$ was not very noisy, but we opted to still use a 21 point ($T = 10$) floating average to smooth out any noise in very low amplitude pulses. In future work a smaller T will most likely be used. This filtered anode pulse traces were only used for identifying the time of maximum amplitudes, and not used for fitting.
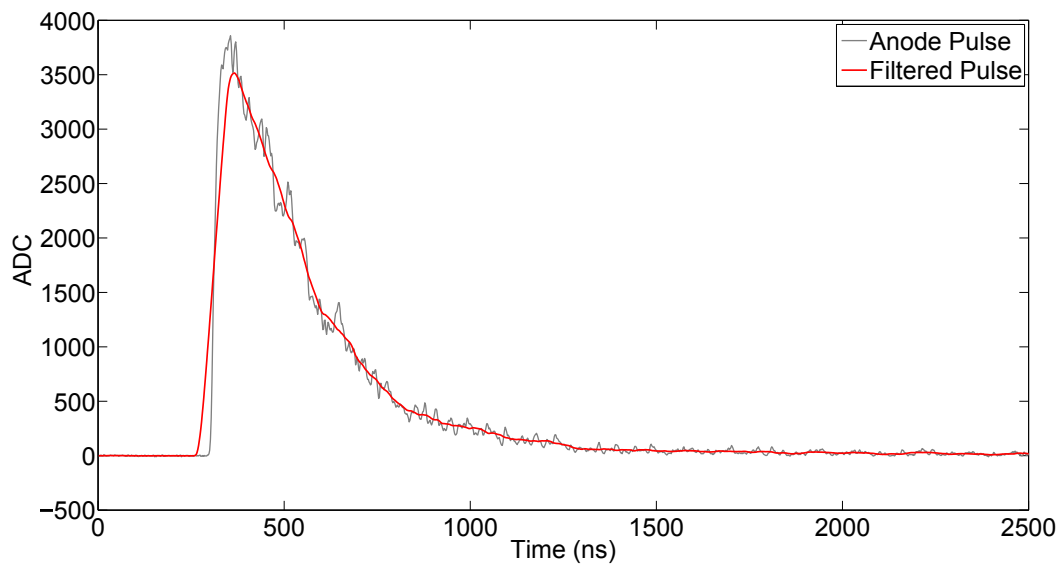
Figure 2.14: NaI(Tl) anode pulse overlaid with the filtered anode pulse.
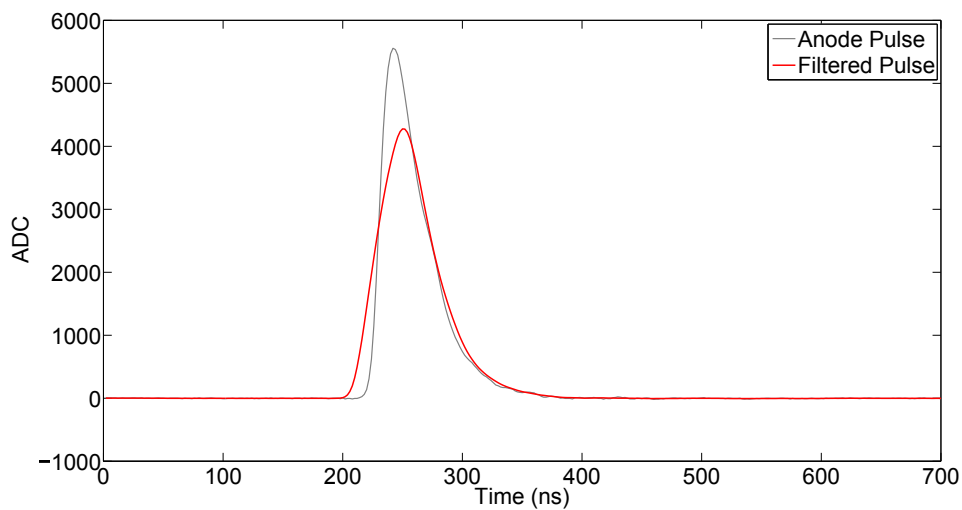
Figure 2.15: CeBr$_3$ anode pulse overlaid with the filtered anode pulse.

2.6 Fitting Algorithm

A trust-region algorithm was used for solving the nonlinear models created from Eq.2.8. The simple idea of this algorithm is that the parameters passed to it give a "region" of trusted values

24

around the values passed for fitting new parameters. Once the first parameters are passed to the fitter, the equation is evaluated and the sum of the squared errors (SSE) is computed. Once the SSE is evaluated the fitter begins solving a trial step where small changes in fitting parameters are applied. Each subproblem has the SSE evaluated. The Hessian matrix (square matrix of the second derivatives) is used to determine a vector to move each fitted parameter toward a local or global minimum. Once these changes are tested and their SSE evaluated the fitting parameters are moved only when the SSE decreases. Once changes in fitting parameter only increase or do not change the SSE, the "best" fit parameters are returned. This method was used so constraints could be placed on the fit parameters. For a detailed look at the workings of this algorithm please read Refs.[14, 15, 16, 17, 18, 19]. This method was chosen over Levenberg-Marquardt due to its ability to have constraints placed upon the algorithm. Unconstrained minimization sometimes yielded non-physical values for some parameters or outright failed to converge.

Chapter 3

Experimental Procedures and Methods

3.1   Experimental Setup

All of the collected data was taken inside a Faraday cage to reduce RF noise. The equipment used is shown in Table 3.1.

Table 3.1: Instruments and equipment used for this research. Equipment used in the CeBr$_3$ system is annotated with the † superscript. Equipment used in both systems is annotated with a †† superscript.

Instrument	Manufacturer	Model Number
High Voltage Power Supply	ORTEC	556
Low Voltage Power Supply†	BK Precision	1550
38.1mm × 38.1mm CeBr$_3$†	Scionix	38B38/2M-HV-CEBR-X2
50.8mm × 50.8mm NaI(Tl)	ORTEC	905-3
Pre-Amplifier†	Canberra	2005
Pre-Amplifier	ORTEC	276
Amplifier††	ORTEC	572A
NIM Bin††	ORTEC	4001A
2K Multi-Channel Analyzer††	ORTEC	EASY-MCA-2K
Fast Waveform Digitizer††	XIA-National Instruments	Pixie - 500
Oscilliscope††	Tektronix	DPO2012

3.2 Sodium Iodide and Cerium Bromide Setup

To create a potential difference at each dynode and the anode in the PMT, a high voltage (HV) power supply was used. It is important to correctly set the HV to a level that provides enough electron multiplication for sufficient current to pass through the anode. Increasing the HV causes higher current pulses which will shift the PHS to the right. Having the HV setting too low may not provide enough potential in the PMT for sufficient electron multiplication and current flowing from the anode will be very small.

The NaI(Tl) detector used a standard adjustable HV power supply connected directly to the detector. The CeBr$_3$ detector used a low voltage (LV) power supply connected to a self-contained HV power supply that could be adjusted on the detector. The LV power supply fed 5V to the HV power supply and a simple potentiometer to adjust the HV settings.

Fig. 3.1 shows the setup of the NaI(Tl) analog and digital nuclear pulse processing system used to collect data, and Fig. 3.2 shows the setup of the CeBr$_3$ system.

Our analog nuclear pulse processing system used an HV setting of 700V for the NaI(Tl)

Analog NaI(Tl) Nuclear Pulse Processing System
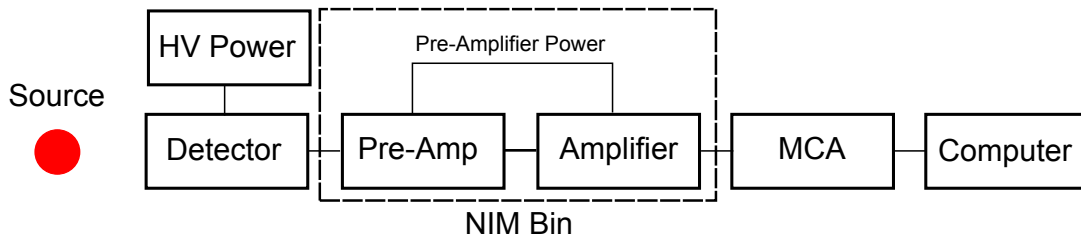
Digitial NaI(Tl) Nuclear Pulse Processing System
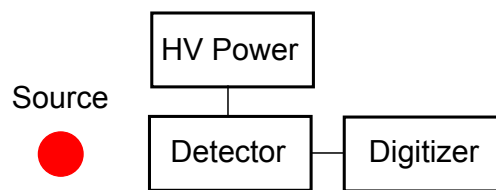
Figure 3.1: NaI(Tl) nuclear pulse processing system setup.

Analog CeBr$_3$ Nuclear Pulse Processing System
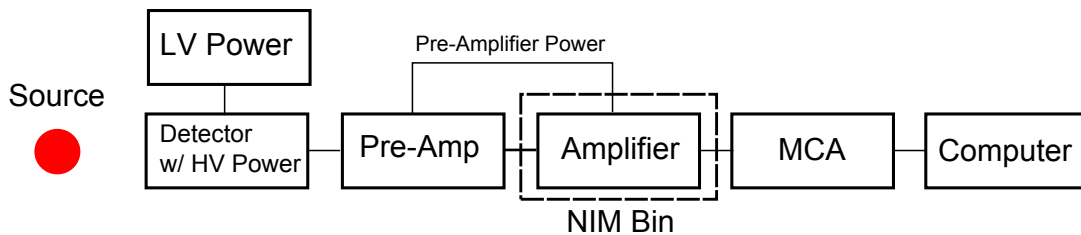
Digitial CeBr$_3$ Nuclear Pulse Processing System
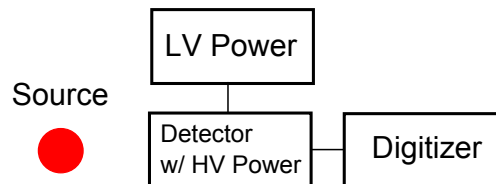
Figure 3.2: CeBr$_3$ nuclear pulse processing system setup.

www.manaraa.com

detector, and an HV setting of 850V for CeBr$_3$. Since our digitizer is sampling from the anode with no amplification, sufficient electron multiplication from the PMT must occur. Since typical anode pulses are in the millivolt range, the HV of the detectors was kept at 1000V to maximize current, but not create overly high current pulses when we directly digitized the anode signal.

3.3 Pixie-500 Setup

This section of the research was not meant to completely resolve the best settings for the Pixie-500, merely to obtain values that allow the research to be completed correctly so the fitting algorithm can be built and tested. Commentary about the Pixie-500 and its settings can be found in Appendix A. Some of these settings were used from pulse shape discrimination research done by Zachary Bailey[20].

The Pixie-500 uses a leading edge trigger to capture incoming waveforms. Since each detector is different, the leading edge thresholds must be set for each detector. In noisy detectors stray signals may cross the leading edge trigger in the digitizer and cause it to digitize noise more than actual gamma ray scintillation events. The NaI(Tl) detector used for these experiments needed an leading edge threshold setting of 200 ADC channels to mitigate this noise. The CeBr$_3$ detector only needed a leading edge threshold setting of 25 ADC channels to accomplish this.

The Pixie-500 has internal memory called a "buffer" where it stores digitized waveforms. It can store a maximum of 8K words of data in a buffer before it is considered full. A "spill" is a term used for when the data stored in the buffer is transferred to the external memory. The Pixie-500 has 3 modes for "List Mode Run," the setting used for these experiments was 32 events per buffer. This means a maximum of 32 events were captured in one buffer, and only after 32 events were captured or the buffer was full did the data in the buffer transfer to the external memory card.

The polling time is a timed function that is used by the Pixie-500 to check the buffers against the list mode run setting to see if a data spill is required. From trial runs the polling time setting used was 0.1 s.

29

The trace window length was also something that varied for each detector. NaI(Tl) has a longer scintillation decay time and PMT decay time and needed a longer trace window to capture the full waveform. The appropriate setting found for our NaI(Tl) detector used a total trace window length of 2,500 ns with a 200 ns pre-trigger trace as shown in Fig.3.3.
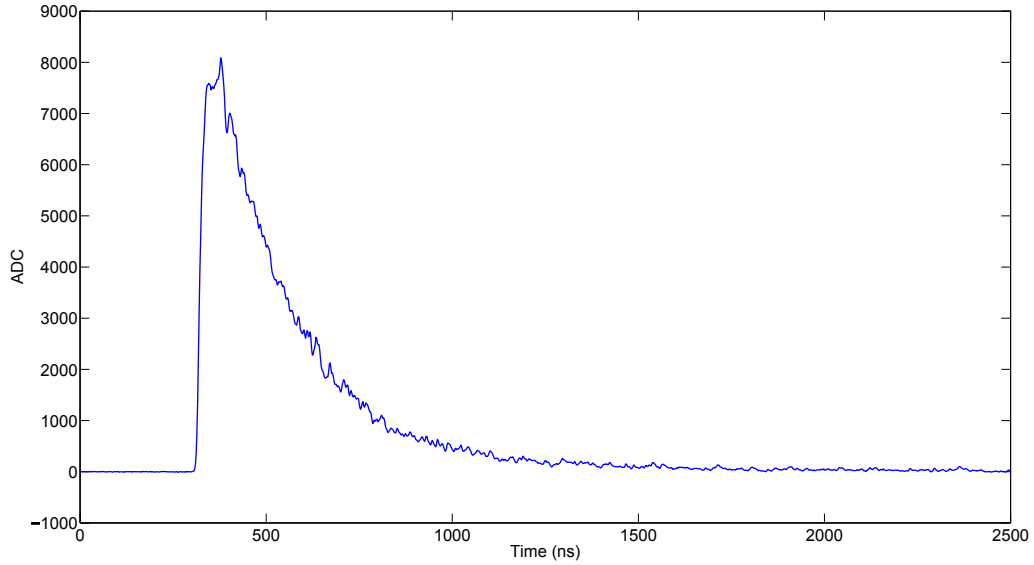
Figure 3.3: 2,500 ns NaI(Tl) trace window width.

For CeBr$_3$ the total trace window length was 700 ns with a 200 ns pre-trigger trace as shown in Fig. 3.4.

30
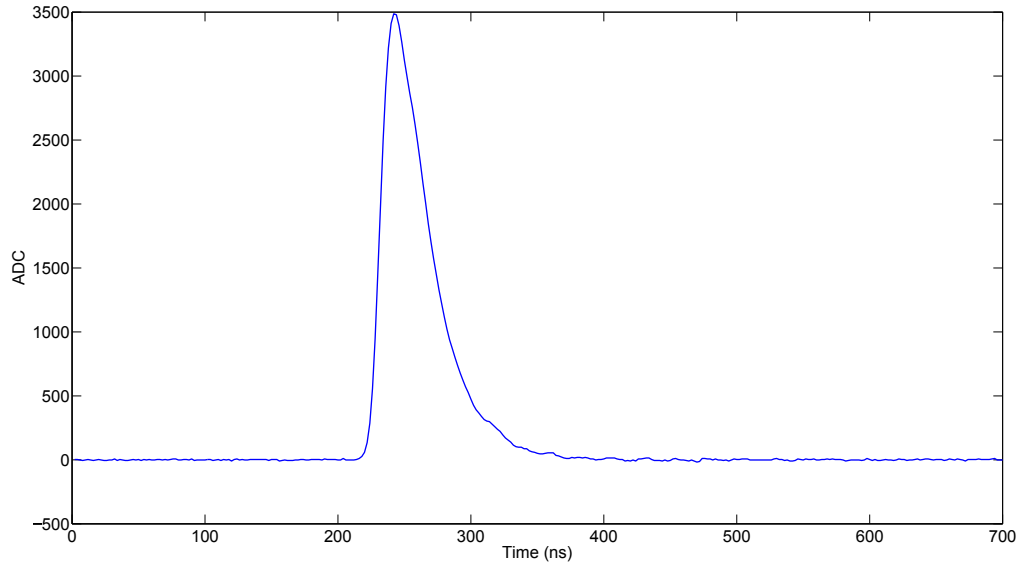
Figure 3.4:   700 ns CeBr$_3$ trace window width.

3.4   Baseline Subtracting Pulses

Although the Pixie-500 does calculate an average baseline when digitizing the anode pulse, a more rigorous algorithm was developed to accurately set the baseline of the trace windows as close to zero as possible. In low count rate environments it can be as simple as averaging the baseline of the pre-trigger trace and then subtracting that value from the entire window. This breaks down when an arriving pulse has a pulse in the pre-trigger trace as shown in Fig. 3.5.

Due to this phenomenon, the fitting algorithm was modified to fit a pre- and post-trigger baseline which the algorithm averages a pre-trigger and post-trigger baseline value.

For NaI(Tl), the data showed that it took a long time before the tail of the pulse decayed back to the pre-trigger baseline levels. The trace windows needed to be kept long enough to capture the entire anode pulse and not clip the tail. This phenomenon was very evident in the NaI(Tl) detector, but was not as evident in the CeBr$_3$ detector due to its short pulse decay time. The NaI(Tl) algorithm first calculates the pre-trigger baseline by the mean of the first

31
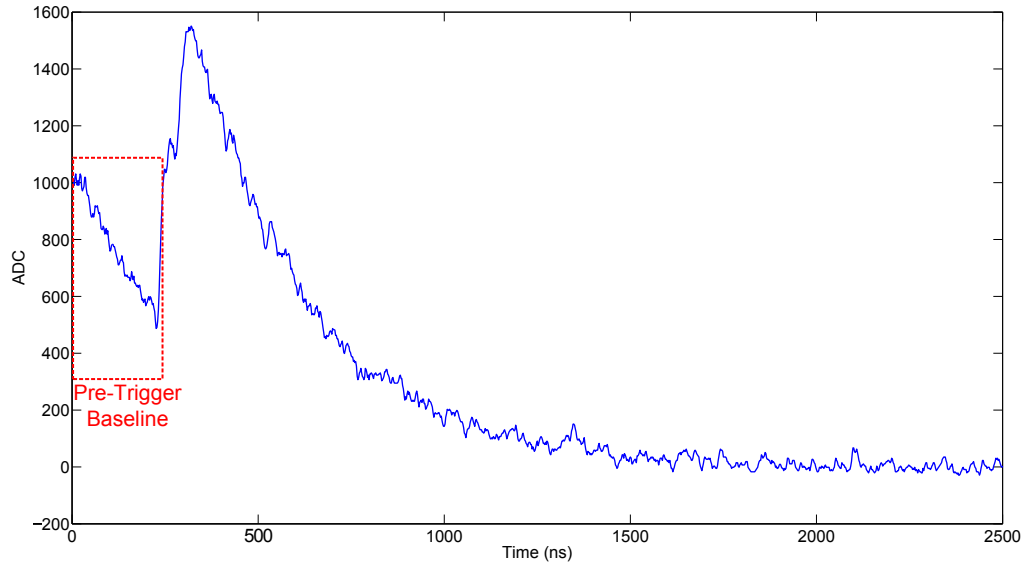
Figure 3.5: NaI(Tl) pulse with a pulse in the pre-trigger baseline region.

100 digitized samples in the trace window, and the post-trigger baseline by the mean of the last 100 digitized samples in the trace window. Due to the possibility of multiple pulses arriving in the pre- and post-trigger baseline regions, checks were used to calculate the most accurate baseline values from the trace window. Fig. 3.6 shows the regions where the baseline values are extracted from in NaI(Tl) pulse windows.

The general checks for determining the baselines are shown in Fig. 3.7. The specific baseline value checks for each detector are described below. As a note, the determination of what constituted a "good" initial guess of baseline values was done through experimentation. Values above 10 ADC most likely corresponded to a pulse in the trace in those regions. The ideal pre- and post-trigger baselines should be 0 ADC. So by setting a threshold less than 1 ADC for "good" initial guesses of pre- and post-trigger baseline values yielded better results for initial guesses.

The baseline value checks for NaI(Tl) are:
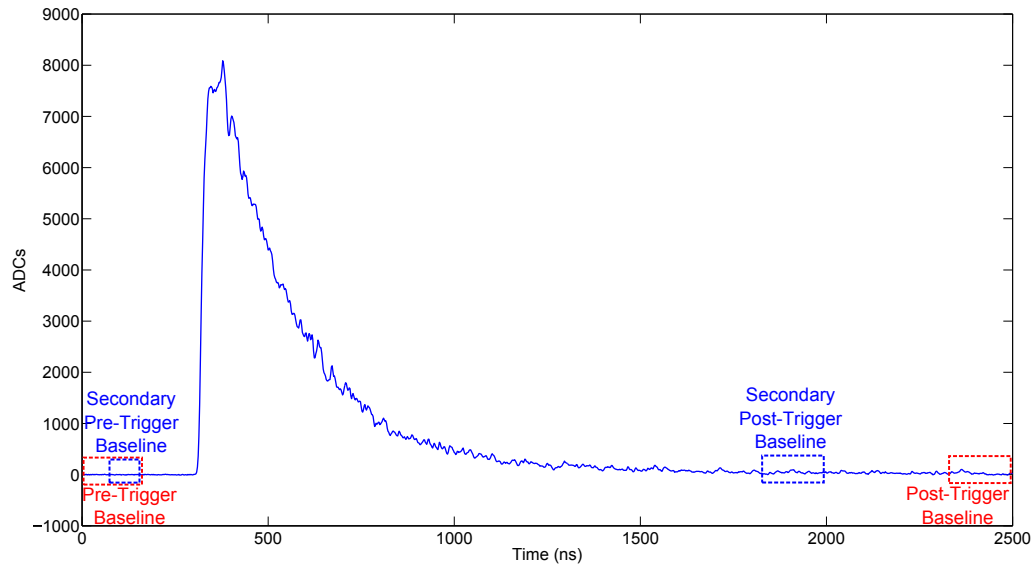
Figure 3.6: NaI(Tl) trace window with baseline regions shown.

1. If pre-trigger baseline value < 1 ADC

   (a) The pre-trigger baseline value is subtracted from the entire trace window

   (b) Pre- and post-trigger baseline values are recalculated for initial guesses for fit parameters

   (c) Pre-trigger baseline value is accepted for initial guess

   (d) If post-trigger baseline value < 10 ADC

      • Post-trigger baseline value is accepted for initial guess

   (e) If post-trigger baseline value > 10 ADC

      i. Recalculate post-trigger baseline in 1800 ns to 2000 ns secondary post-trigger region

      ii. If post-trigger baseline value < 10 ADC

         • Post-trigger baseline value is accepted for initial guess

Starting Point
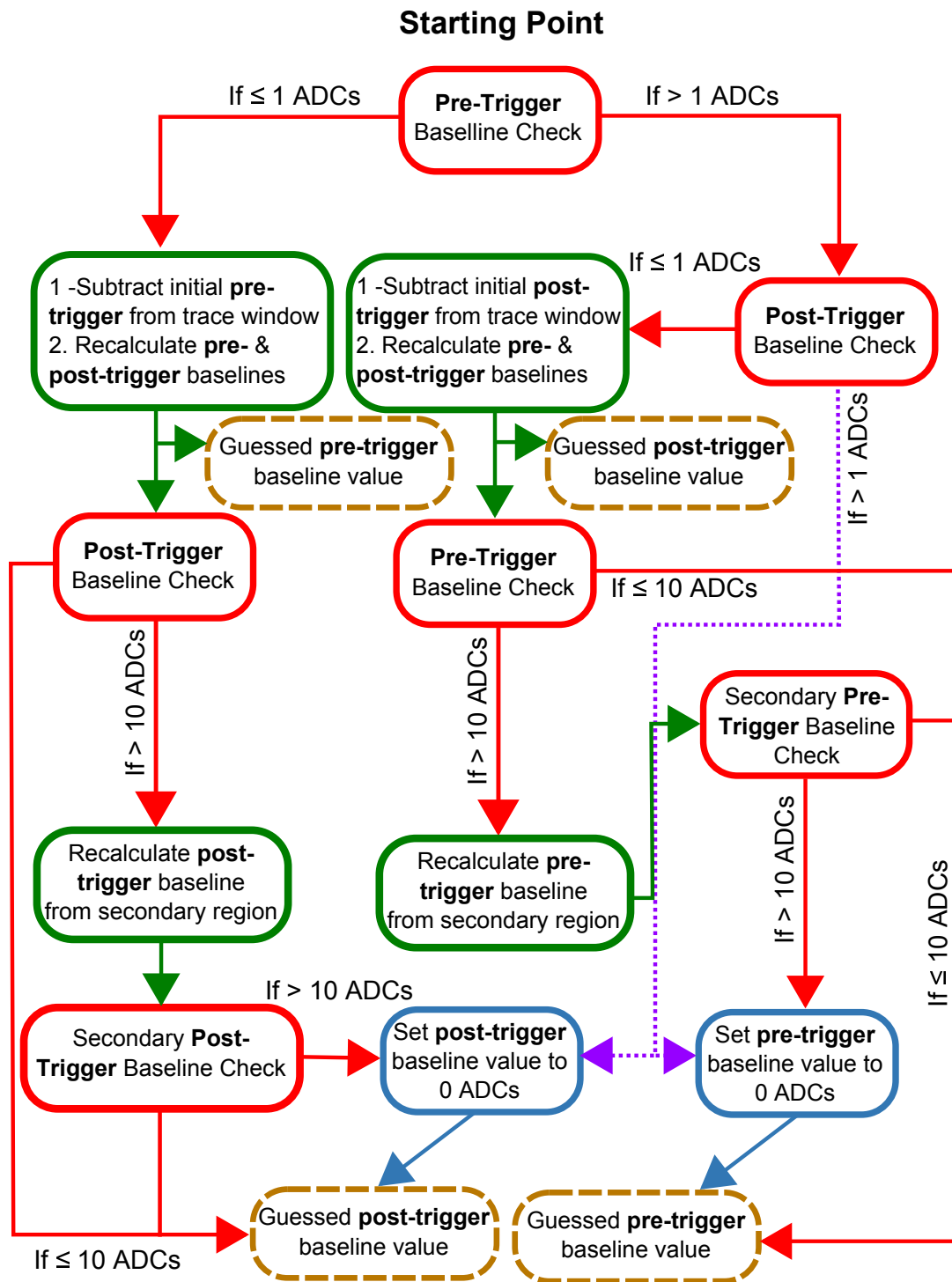
Figure 3.7: Baseline determination checks.

iii. If post-trigger baseline value > 10 ADC

- Post-trigger baseline value is set to 0 ADCs for initial guess

2. If pre-trigger baseline value > 1 ADC and post-trigger baseline value < 1 ADC

   (a) The post-trigger baseline value is subtracted from the entire trace window

   (b) Pre- and post-trigger baseline values are recalculated for initial guesses for fit parameters

   (c) Post-trigger baseline value is accepted for initial guess

   (d) If pre-trigger baseline value < 10 ADC

   - Pre-trigger baseline is accepted for initial guess

   (e) If pre-trigger baseline value > 10 ADC

      i. Recalculate pre-trigger baseline in 100 ns to 200 ns secondary pre-trigger region

         A. If pre-trigger baseline value < 10 ADC

         - Pre-trigger baseline is accepted for initial guess

         B. If pre-trigger baseline value > 10 ADC

         - Pre-trigger baseline value = 0 ADC

3. If pre- and post-trigger baseline values are > 1 ADC

   - Pre- and post-trigger baseline values set to 0 ADC for initial guess

For CeBr$_3$ the algorithm works exactly the same, only the regions for the secondary pre-baseline region is between 80 ns to 180 ns, and the secondary post-trigger baseline region is between 450 ns to 550 ns. Fig. 3.8 shows the regions where the baseline values are extracted from in CeBr$_3$ pulse windows.
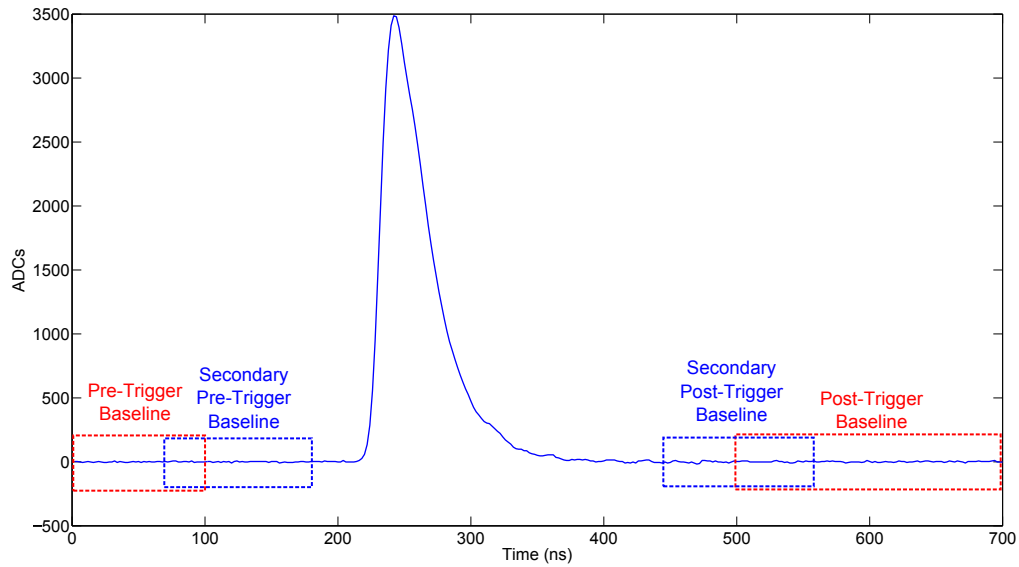
Figure 3.8: CeBr$_3$ trace window with baseline regions shown.

3.5   Flat-Topped Pulses

The Pixie-500 has an internal oscilloscope that can be used to set the gain offsets of the incoming channels. The ADC has an input range of 2V and this gain adjustment tunes the dynamic range of the channel. Due to flat-topping, there can be some saturation of high current pulses. From experimentation the NaI(Tl) and CeBr$_3$ both had this floating "flat-top" to these high current pulses as shown in Fig.3.9 and Fig 3.10.

Due to this, the algorithm looked for pulses that had over 6 occurrences of values equal to the maximum value of the trace window. These trace windows were then logged and then removed from the data set.
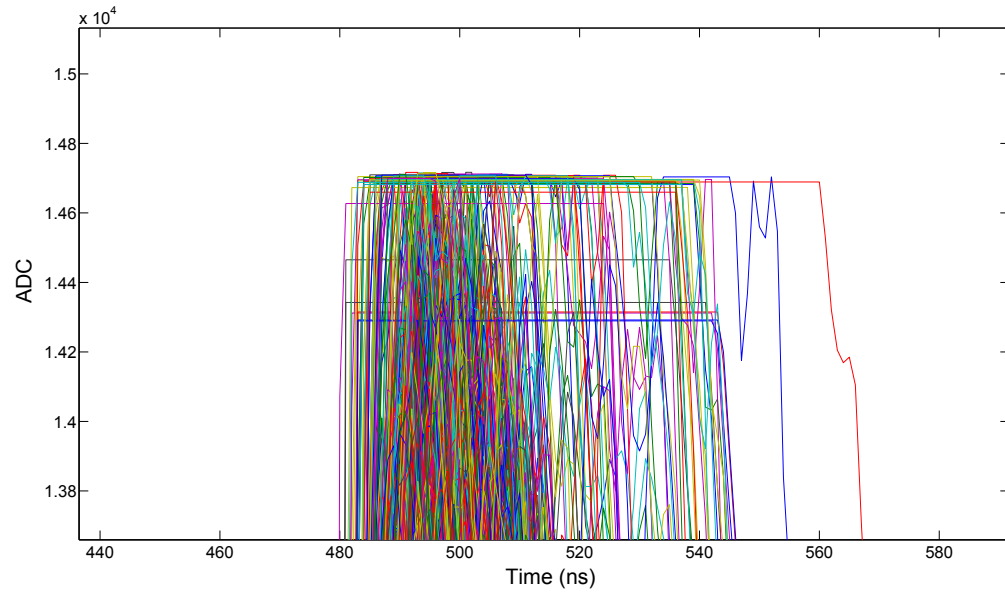
Figure 3.9: NaI(Tl) flat-top pulses.
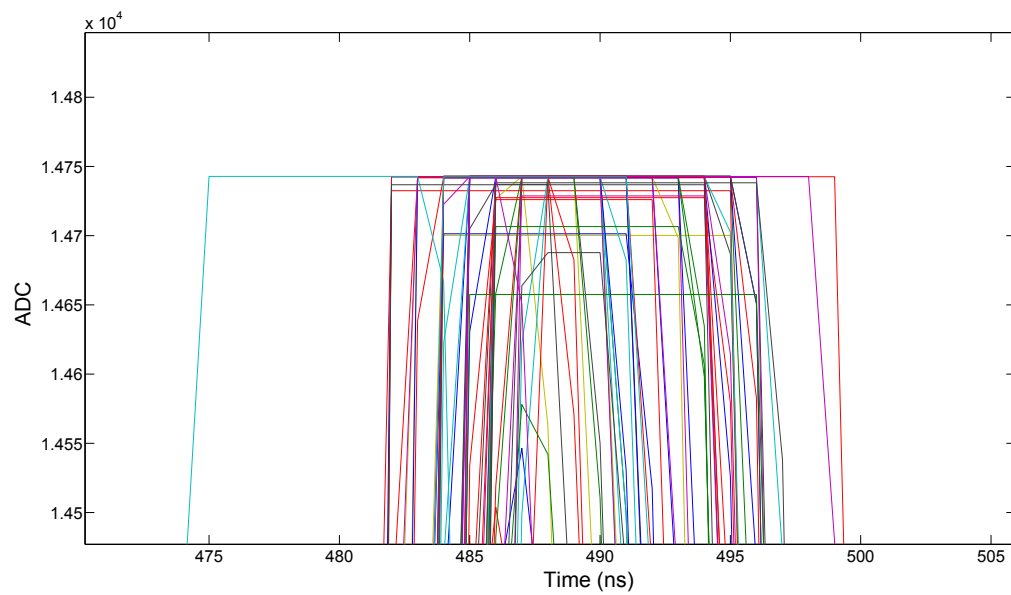
Figure 3.10: CeBr$_3$ flat-top pulses.

37

3.6 Identifying Maximum Pulse Amplitude and Time of Maximum Amplitude

The next two initial guess values that need to be determined to pass to the fitting algorithm are the maximum amplitude of the pulse and the time that the maximum amplitude arrived. Since the NaI(Tl) detector used for these experiments had a lot of signal noise, a floating average low pass filter was applied to all the trace windows to smooth out the digitized anode signal; a 41 point floating average was used. CeBr$_3$ had little to no noticeable noise in the traces, so a 21 point floating average was used to smooth out its data. These filtered pulses were then differentiated to find the maximum amplitudes and times. Since differentiating these trace windows will show a zero crossing at local maxima and minima, a threshold trigger was used to start looking for zero crossings in the derivatives of the trace windows. Due to the floating point averaging filter, false maxima were shown in the differentiated trace windows at two specific points. Since NaI(Tl) used a 41 point floating average, the starting point was 21 digitized sample into the trace window, and ended 21 digitized samples before the end of the window. In CeBr$_3$ the first and last 10 digitized samples were omitted due to this floating point averaging filter. From experimentation a differentiated pulse trigger level of 19 ADC was used to look for pulses in NaI(Tl), and 6 ADC in CeBr$_3$. Once a value in the trace goes above the trigger threshold, it starts to look for the data point value to go below zero. Once below zero, the digitized sample value was recorded, and the algorithm continued searching the rest of the window for values above the trigger level. Fig.3.11 shows a NaI(Tl) anode pulse with the differentiated pulse overlaid with the zero crossings marked. Fig.3.12 shows a CeBr$_3$ anode pulse with the differentiated pulse overlaid with the zero crossings marked.

After the zero crossing times were stored, the maximum amplitudes were stored by taking the ADC value at the zero crossing times. If multiple pulses were found, multiple amplitudes were stored. After this, another variable was calculated that determined the number of pulses in the trace window. This value will determine the first analytical model used for fitting the
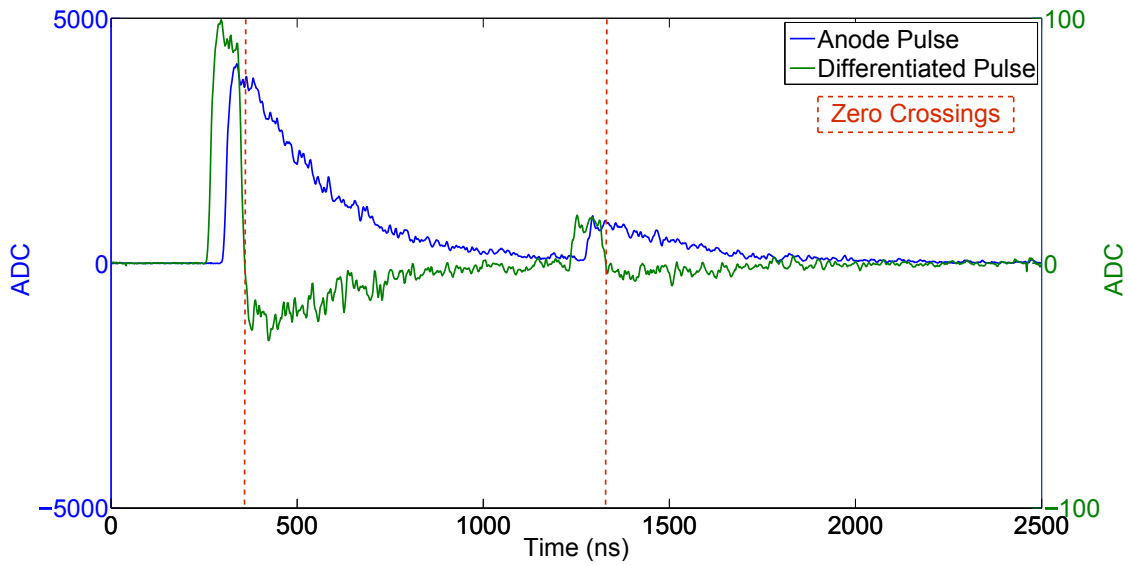
Figure 3.11: NaI(Tl) trace window with 2 anode pulses overlaid with the differentiated trace window. The dashed red lines show where the differentiated trace window crosses zero.
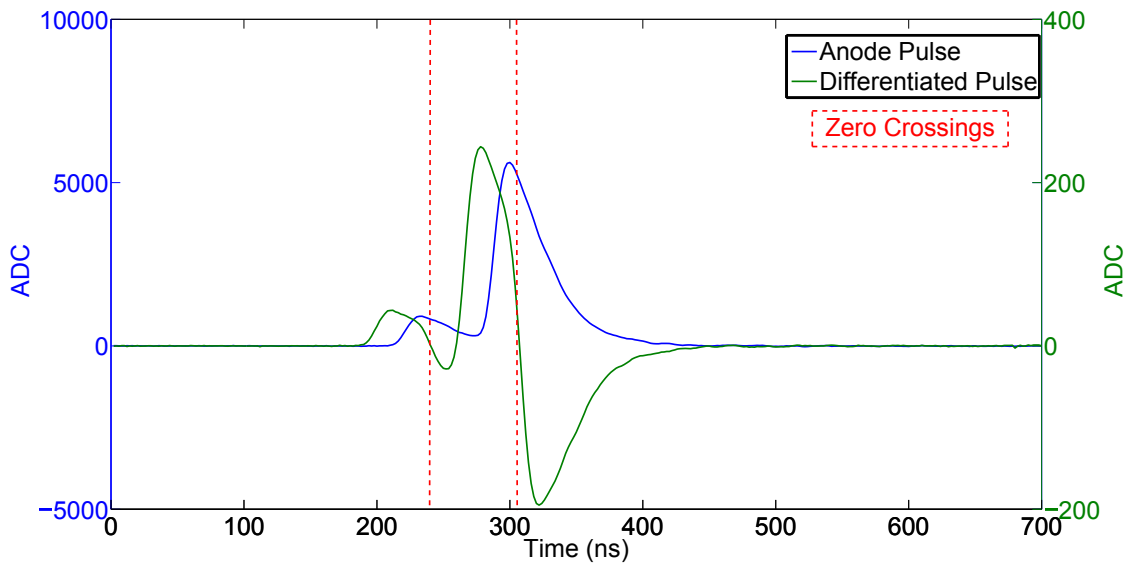
Figure 3.12: CeBr$_3$ trace window with 2 anode pulses overlaid with the differentiated trace window. The dashed red lines show where the differentiated trace window crosses zero.

39

trace window.

3.7 Fitting of Trace Windows

To improve the efficiency of fitting, a correction to the initially guessed amplitudes was needed. Since the stored amplitude parameter is convolved with τ_r and τ_f values (see Eq. 2.8) from the analytical model, a correction factor was applied to the initial guess of the amplitude to make the initial guess value closer to the real amplitude value. Plotting the originally guessed amplitudes to the fit amplitudes, it was found that they all followed a nearly linear trend. Due to this, all the amplitudes for NaI(Tl) were multiplied by 1.3533, and CeBr$_3$ by 1.7970.

It was found that the zero crossing times also needed to be corrected to pass better initial guesses for pulse arrival times to the fitter. It was found for NaI(Tl) that the average zero crossing times were approximately 60 ns ahead of the pulse arrival times. For CeBr$_3$ the average zero crossing times were approximately 25 ns ahead of the fit pulse arrival times. So each zero crossing time had its pulse arrival time adjustment subtracted from it to give us our pulse arrive time initial guesses.

The next step after these corrections were made was to calculate initial guesses for the scintillator decay time (τ_r) and PMT decay time (τ_f). This was done by correlating single fit pulse amplitudes to fit pulse scintillation and PMT decay times. These values were then used to linearly interpolate guessed amplitudes to reasonable guessed τ_r and τ_f values. Now all the required fit initial guesses have been determined, and fitting can be started on the trace windows.

Fig.3.13 and Fig. 3.14 show the values used to obtain the initial guesses for the τ_r and τ_f for NaI(Tl). Fig.3.15 and Fig. 3.16 show the values used to obtain the initial guesses for the τ_r and τ_f for CeBr$_3$.

Fig. 3.17 is a flow chart for the fitting algorithm. The first step in starting the fitting algorithm was to examine the guessed number of pulses in the trace window. This value was used to determine which model to use in fitting the trace window. Models with one, two, and three pulses per trace window were used. This is done on all the trace windows, and then the fit results are extracted along with their uncertainties. Relative uncertainties are calculated from

41
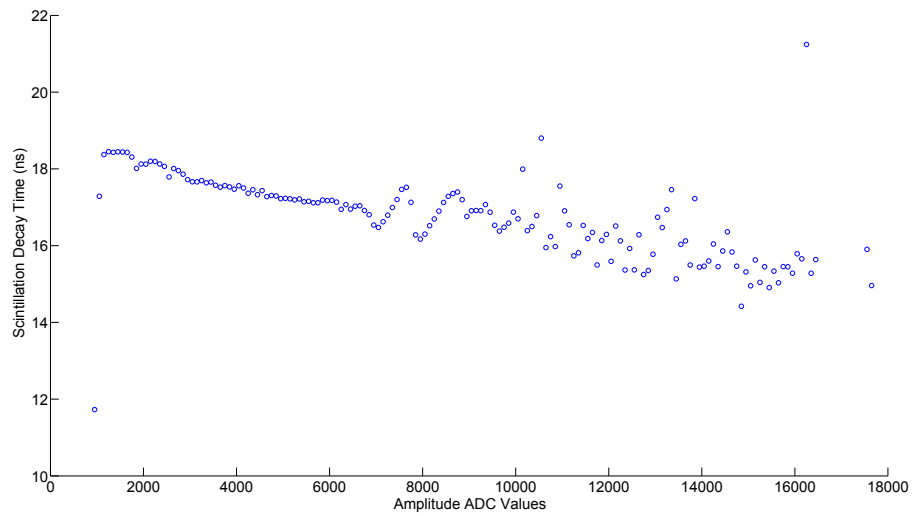
Figure 3.13: τ_r vs. amplitude. Values used for estimating initial guesses for NaI(Tl) scintillation decay times based on pulse amplitude.
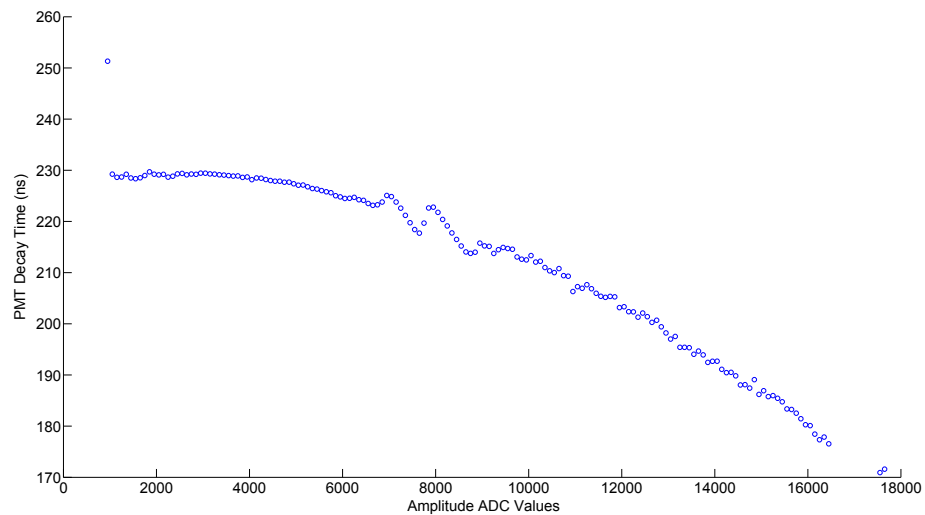
Figure 3.14: τ_f vs. amplitude. Values for estimating initial guesses for NaI(Tl) PMT decay times based on pulse amplitude.

42
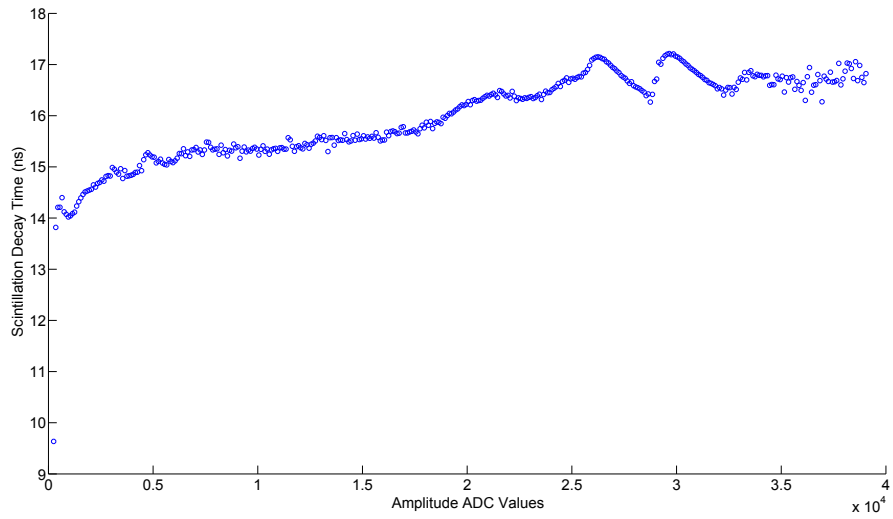
Figure 3.15: τ_r vs. amplitude. Values used for estimating initial guesses for CeBr$_3$ scintillation decay times based on pulse amplitude. These are on a Log-Linear scale.
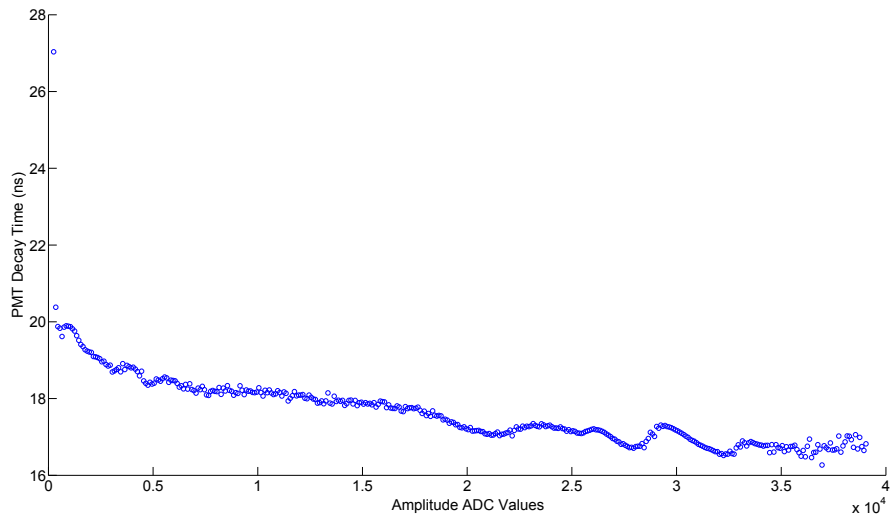
Figure 3.16: τ_f vs. amplitude. Values for estimating initial guesses for CeBr$_3$ PMT decay times based on pulse amplitude. These are on a Log-Linear scale.

43
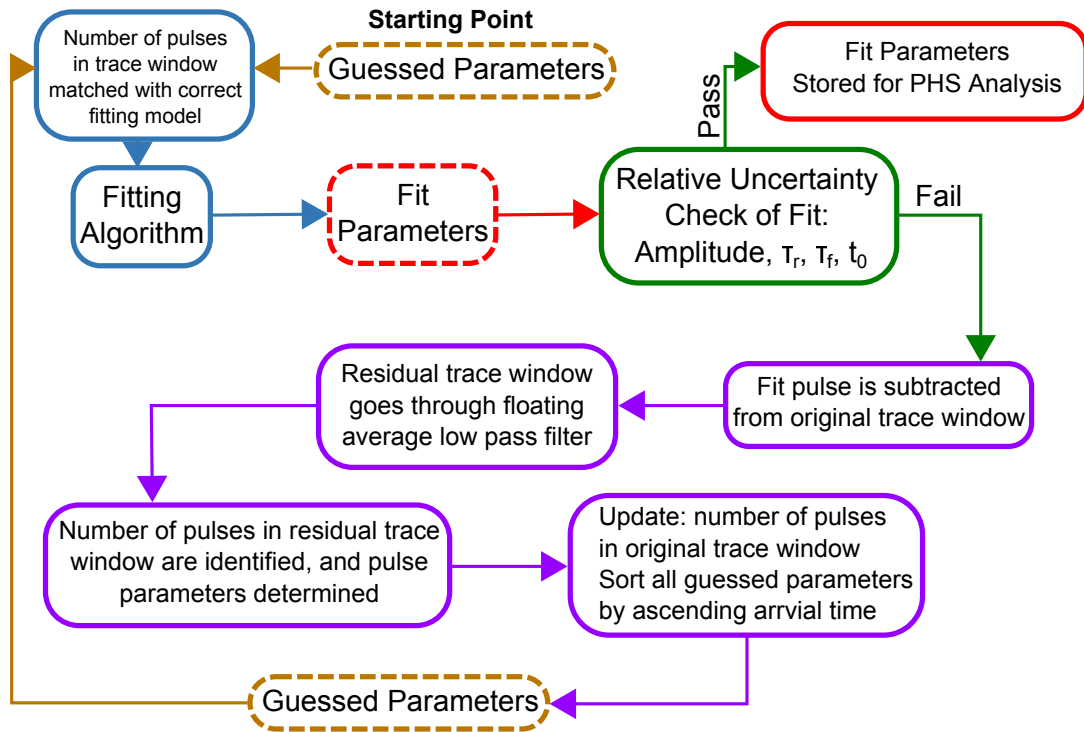
Figure 3.17: Deconvolution algorithm flow chart.

the fit values uncertainty divided by the fit value.

The next step is to determine what pulses had relative uncertainties below thresholds set for each A, τ_r, and τ_f values. These were determined from experiments that showed where most of the uncertainties lie for each fit value. The baseline values were not examined since it should be close to 0, and is not used for determining the PHS. Arrival times were examined only to see if pulse arrival times and their uncertainties overlapped other pulse's arrival times and their uncertainties. It was found that pulses below 1000 ADC had different relative uncertainties than those above 1000 ADC. Fig. 3.18 shows the relative uncertainties of the fit amplitudes above 1000 ADC. Fig. 3.19 are the relative uncertainties of the fit amplitudes below 1000 ADC. During these experiments it was found that lower amplitude pulses had accurate fits, but higher relative uncertainties associated with the fit parameters. Because of this, two separate relative uncertainty thresholds were used to check the goodness-of-fit of the pulse parameters. Fig. 3.20
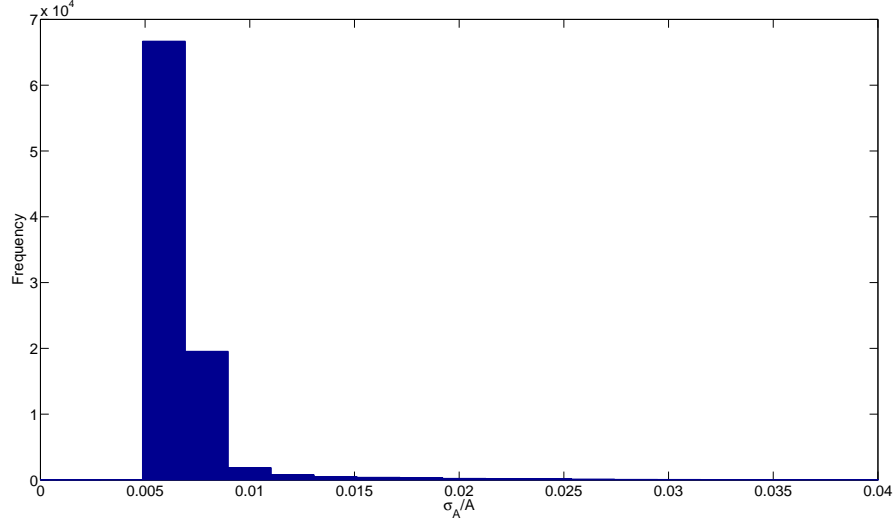
Figure 3.18:   NaI(Tl) relative uncertainties of the fit amplitude values above 1000 ADC.

Table 3.2:   Relative uncertainties for NaI(Tl) fit values.

Rel. Uncertainties	$\leq$ 1000 ADC	$>$ 1000 ADC
σ_{amp}/A	2	0.03
σ_{τ_r}/τ_r	2	0.1
σ_{τ_f}/τ_f	2	0.07

shows the relative uncertainties of the τ_r fit parameter with pulse amplitudes above 1000 ADC, and Fig. 3.21 shows the relative uncertainties of the τ_r fit parameter with pulse amplitudes below 1000 ADC. Fig. 3.22 shows the relative uncertainties of the τ_f fit parameter with amplitudes above 1000 ADC. Fig. 3.23 shows the relative uncertainties of the τ_f fit parameter with pulse amplitudes below 1000 ADC. The refitting threshold values for NaI(Tl) are shown in Table 3.2. It was found these values accepted enough well fit pulses while omitting poorly fit ones.

The same relative uncertainties were examined to find good threshold values for CeBr$_3$. The thresholds were increased to allow higher relative uncertainties to not trigger refitting.

45
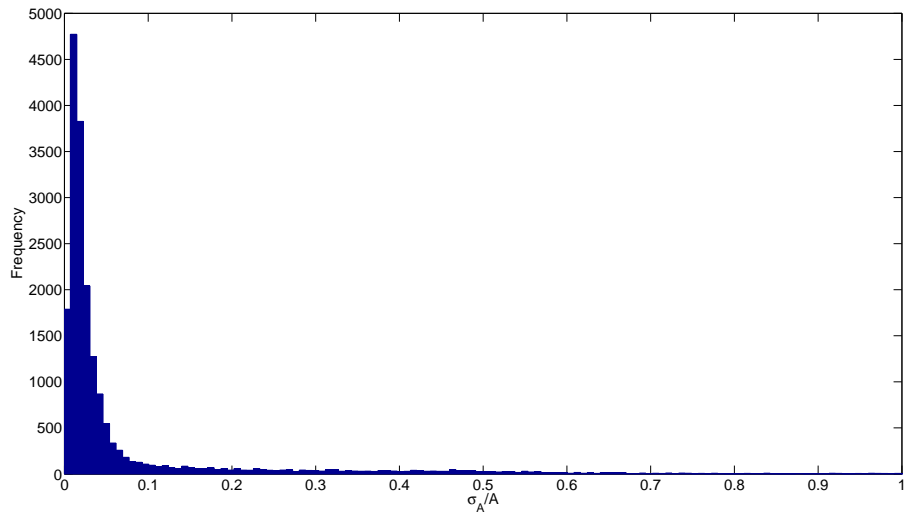
Figure 3.19: NaI(Tl) relative uncertainties of the fit amplitude values below 1000 ADC.
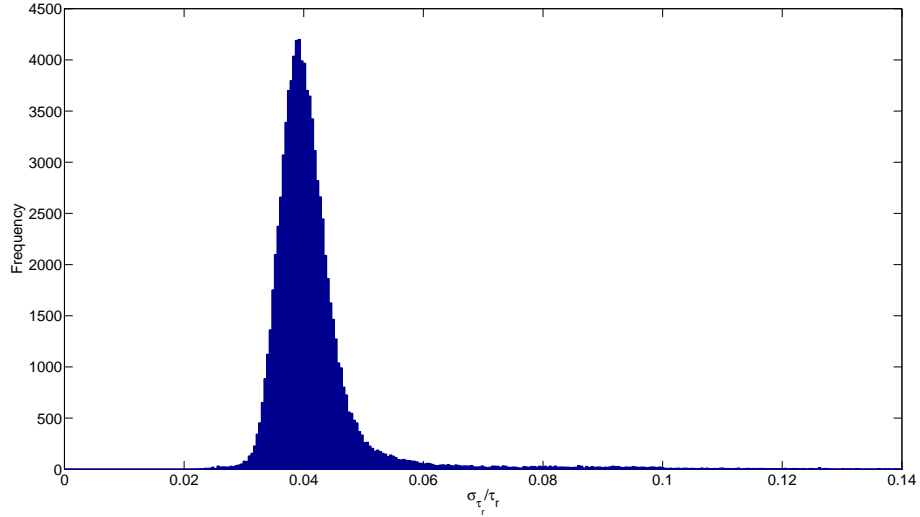
Figure 3.20: NaI(Tl) relative uncertainties of the fit τ_r values with fit amplitudes above 1000 ADC.

46
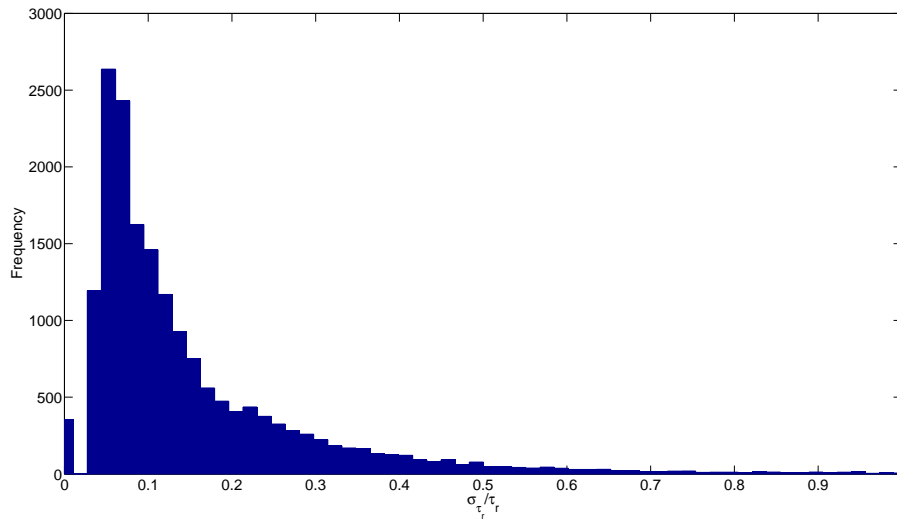
Figure 3.21: NaI(Tl) relative uncertainties of the fit τ_r values with fit amplitudes below 1000 ADC.
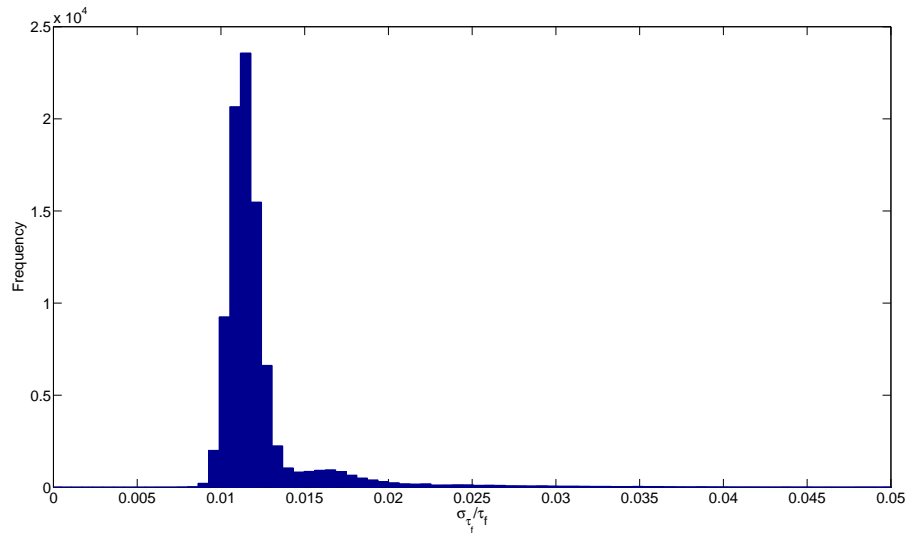
Figure 3.22: NaI(Tl) relative uncertainties of the fit τ_f values with fit amplitudes above 1000 ADC.

47
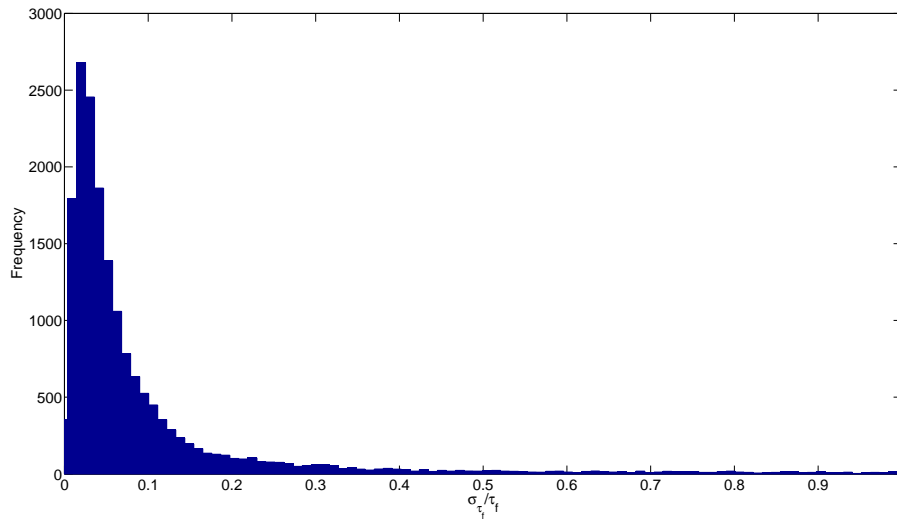
Figure 3.23: NaI(Tl) relative uncertainties of the fit τ_f values with fit amplitudes below 1000 ADC.
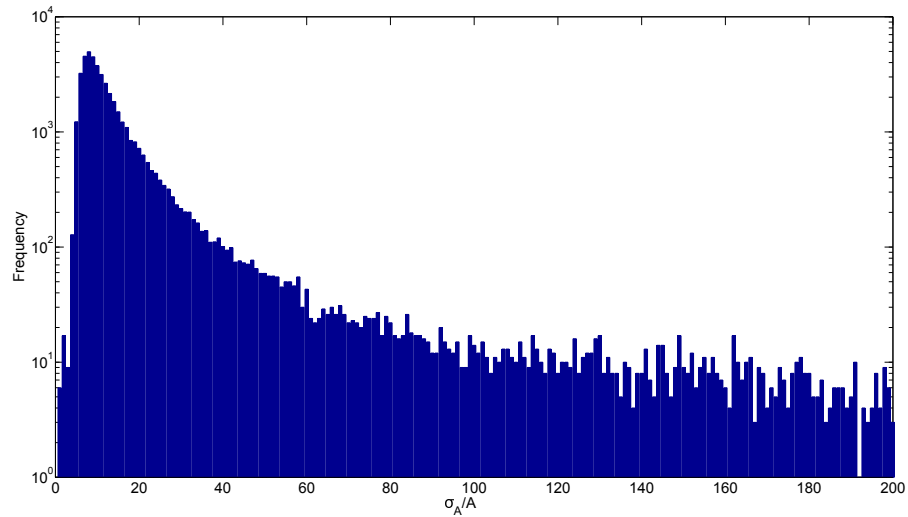
Figure 3.24: CeBr$_3$ relative uncertainties of the fit amplitude values above 1000 ADC. These are on a log-linear scale.

48
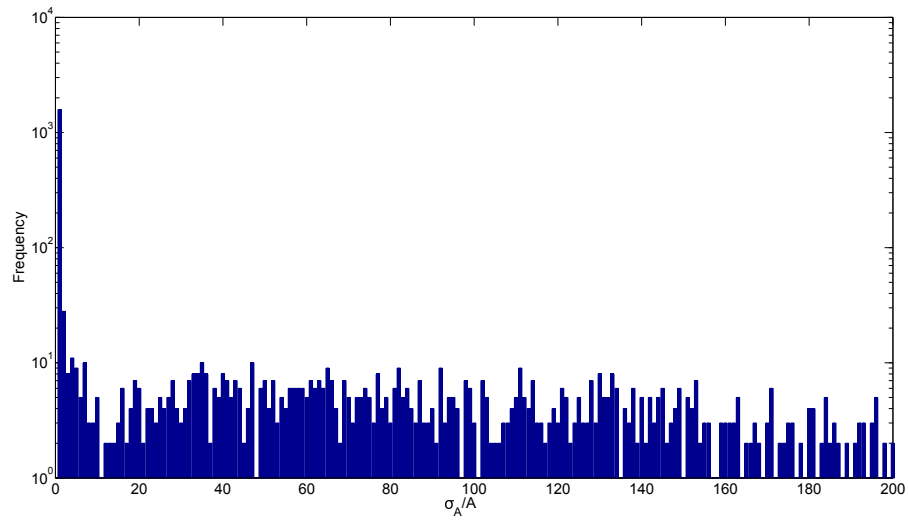
Figure 3.25: CeBr$_3$ relative uncertainties of the fit amplitude values below 1000 ADC. These are on a log-linear scale.
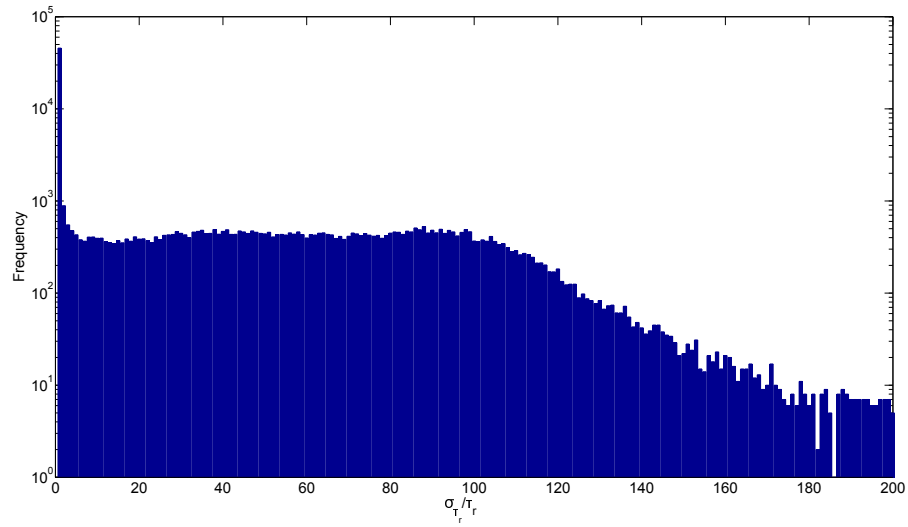
Figure 3.26: CeBr$_3$ relative uncertainties of the fit τ_r values with fit amplitudes above 1000 ADCs. These are on a log-linear scale.

49
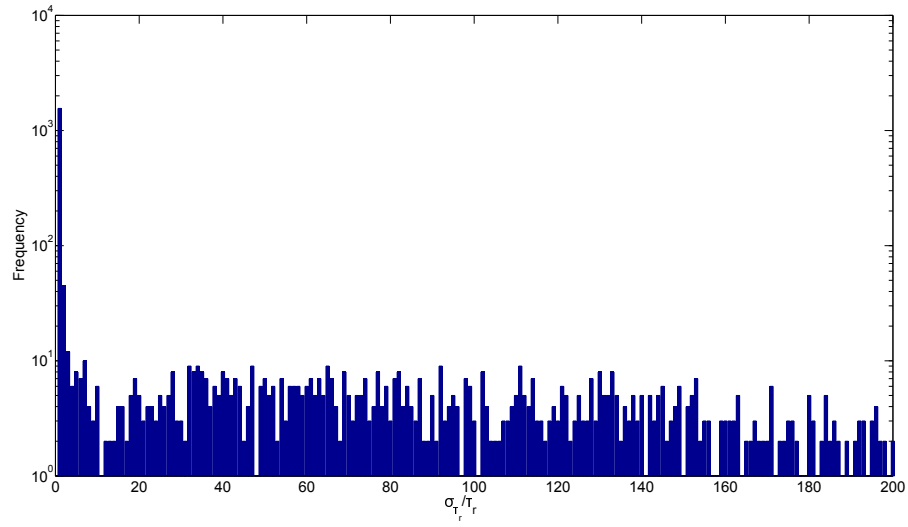
Figure 3.27: CeBr$_3$ relative uncertainties of the fit τ_r values with fit amplitudes below 1000 ADC. These are on a log-linear scale.
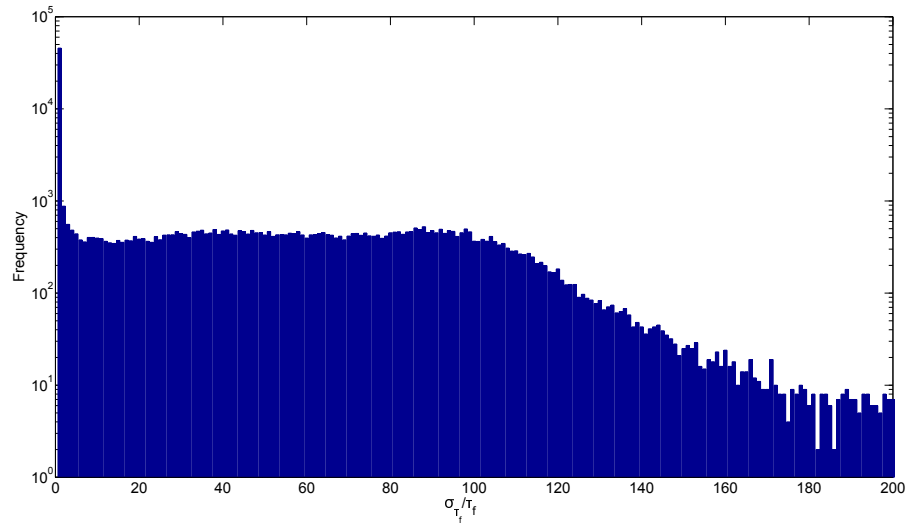
Figure 3.28: CeBr$_3$ relative uncertainties of the fit τ_f values with fit amplitudes above 1000 ADC. These are on a log-linear scale.
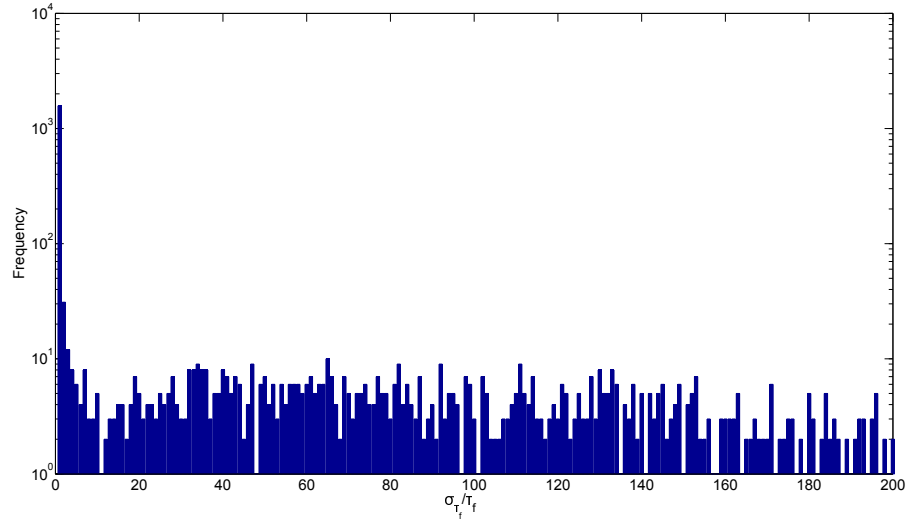
Figure 3.29: CeBr$_3$ relative uncertainties of the fit τ_f values with fit amplitudes below 1000 ADC. These are on a log-linear scale.

Table 3.3: Relative uncertainties for CeBr$_3$ fit values.

Rel. Uncertainties	≤ 1000 ADC	> 1000 ADC
σ_{amp}/A	150	150
σ_{τ_r}/τ_r	150	150
σ_{τ_f}/τ_f	120	120

Figs. 3.24 - 3.29 show the histograms of the relative uncertainties and are on log-linear scales. A threshold value of 150 was used for the amplitude, and τ_r fit parameters, and a threshold value of 120 was used for τ_f fit parameter. These refitting threshold values for CeBr$_3$ are shown in Table 3.3.

Fit parameters were then checked against these values. Fit parameters that passed the check were stored for PHS analysis. Pulses with relative uncertainties above these threshold values were identified for a secondary fitting. These trace windows identified for a secondary

51

refitting had the fit results from the first fitting subtracted from the trace window to remove the previously identified pulses. From here, these residual traces had the floating averaging low pass filter applied, differentiated, and maximum amplitudes and pulse arrival times determined from the residuals of the trace window. See subsection 3.6 for the complete workings. After these values are determined, a check is done to see if any of the amplitudes are below 150 ADC. If the value of the maximum amplitude is below the threshold, the amplitude and corresponding maximum time value are removed from the list of values. After this step, the number of pulses in the trace window is again determined and stored to be passed to the fitter. The new fit amplitudes are used to linearly interpolate their τ_r and τ_f. Now that these parameters have been determined, the total number of pulses in the trace window is calculated by the original number of pulses in the trace window added to the secondary number determined. The original fit values are passed again as fit parameters along with the secondary parameters. Once all of these values have been set, they are all sorted by ascending arrival times. The smallest time value is sorted to have its fit parameters passed as the first pulse, and the other values sorted accordingly. The updated fit parameters are passed to the fitter with the determined fit model.

The next step is to test the fit parameters relative uncertainties. If they pass the check, the values are stored for PHS analysis. If one or more of the fit parameters fails this check this then begins a tertiary fitting process. It follows the same pattern as above in the secondary refitting. Since the deconvolution algorithm only searches for at most 3 pulses per trace window, pulses poorly fit after the tertiary refitting were removed from the data set.

3.8 PHS Code

Once all of the trace windows have been processed through the deconvolution algorithm the fit parameters stored for PHS analysis are used to create a PHS. Using Eq. 2.15, the fit amplitude and τ_f parameters from each pulse can be used to calculate the charge collected (Q) from the pulse. Once all of Q values from the individual pulses have been calculated, a histogram of the values can be created which is the PHS.
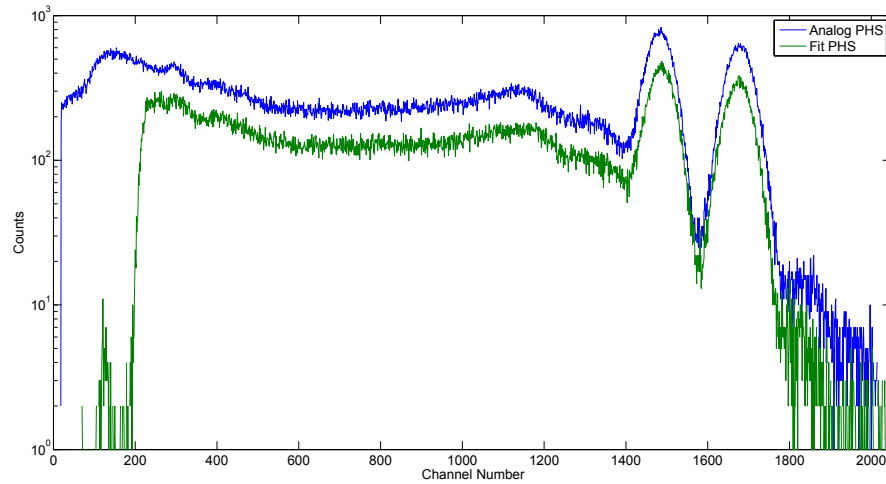
Figure 3.30: NaI(Tl) analog PHS compared to the fit PHS from a 5μCi ^{60}Co source.

Table 3.4: Fit values for PHS calibration. Y corresponds to the charge collected and x is the channel number.

$Y(x) = ax^2 + bx + c$			
Detector	a	b	c
NaI(Tl)	-0.04457308176	1201.94631814947	14710.0562660875
CeBr$_3$	0.0043305007	285.9852850946	63.2119085304

Using three analog PHS from 5μCi ^{60}Co, ^{22}Na, and ^{137}Cs check sources (see Figs. 3.30 - 3.35), a calibration was done with the fit PHS to allow the histogram binning to equate the two pulse height spectra. A polynomial fit was done between the channel numbers (x) in the analog PHS and the charge collected ($Y(x)$) in the fit PHS. Table 3.4 gives the polynomial values of these fits from NaI(Tl) and CeBr$_3$.

This now allows the data from the analog PHS to be compared and evaluated against the digitized PHS.
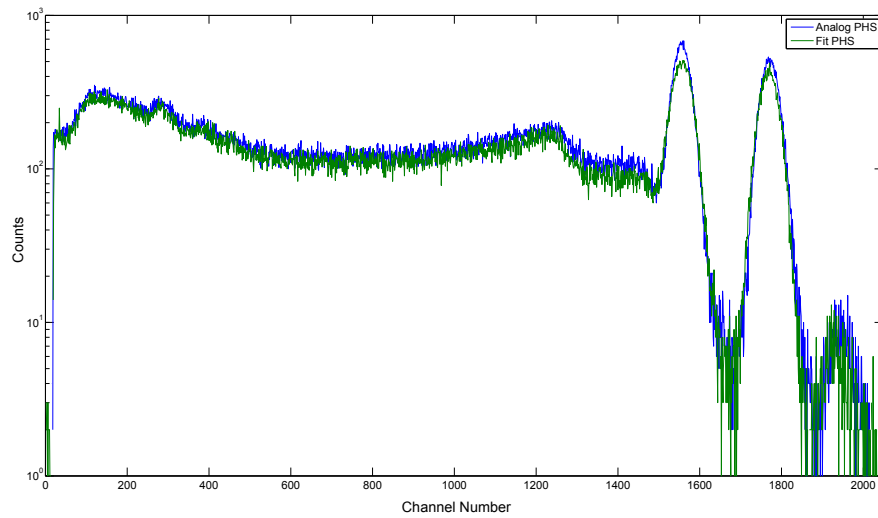
Figure 3.31: CeBr$_3$ analog PHS compared to the fit PHS from a 5μCi ^{60}Co source.
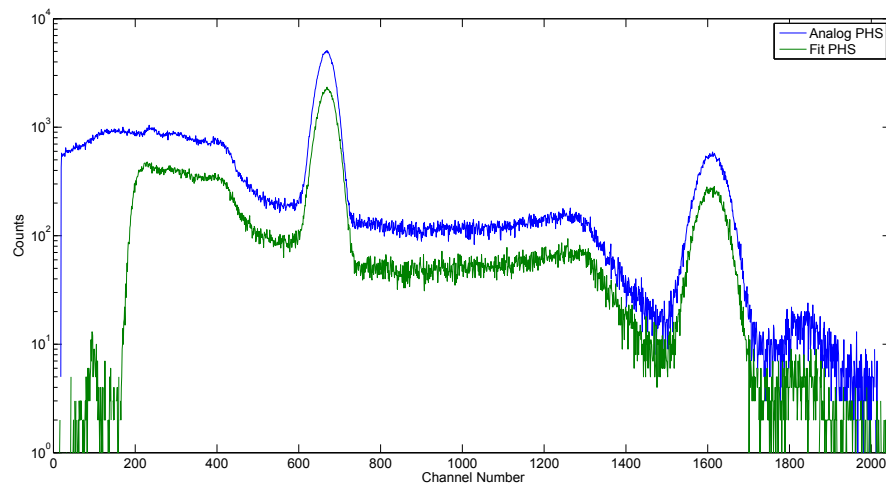
Figure 3.32: NaI(Tl) analog PHS compared to the fit PHS from a 5μCi ^{22}Na source.

54
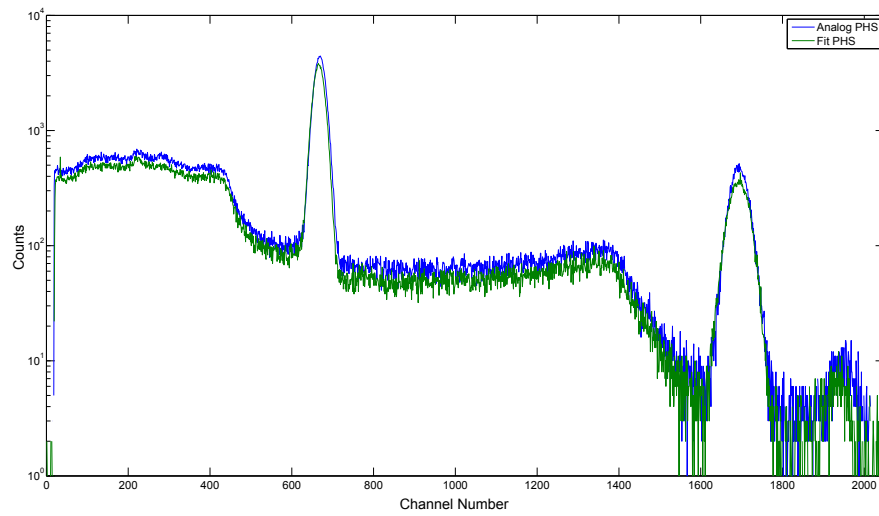
Figure 3.33: CeBr$_3$ analog PHS compared to the fit PHS from a 5μCi ^{22}Na source.
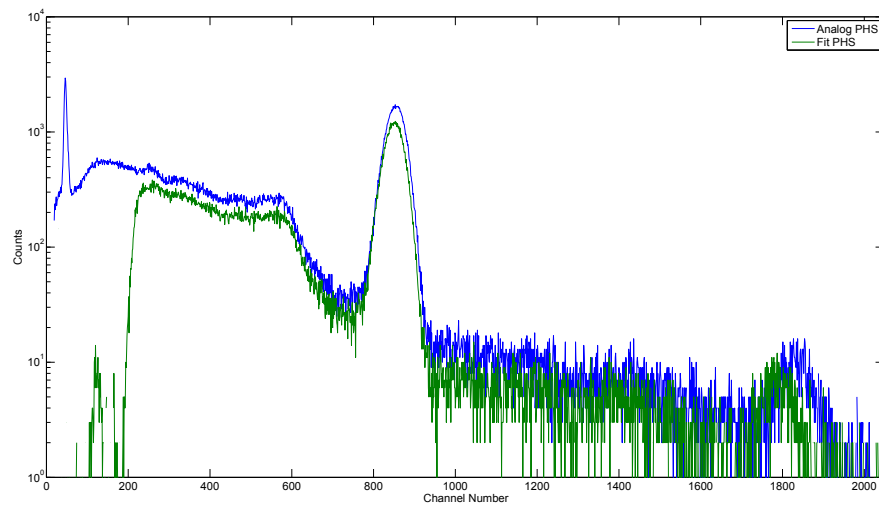
Figure 3.34: NaI(Tl) analog PHS compared to the fit PHS from a 5μCi ^{137}Cs source.

55
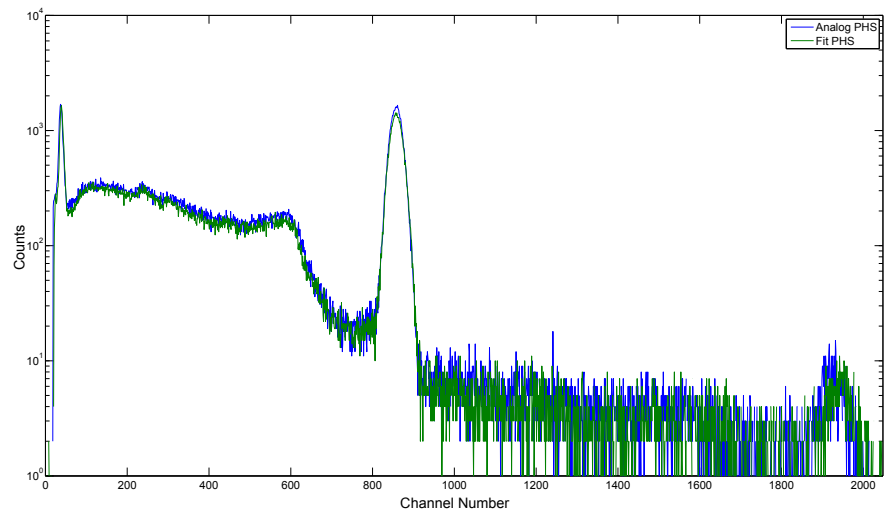
Figure 3.35: CeBr$_3$ analog PHS compared to the fit PHS from a 5μCi ^{137}Cs source.

Chapter 4

Development of Deconvolution Algorithm Analysis Method

This chapter will discuss some different ideas that were tested during the building of the deconvolution algorithm. Some ideas were tested and found that they did not adequately yield accurate estimates, or were not robust enough to strengthen the reliability of the algorithm. The methods used for building this algorithm were determined from trial and error to allow this algorithm's building method to be implemented into other possible fitting algorithms.

4.1   Baseline Values

Initially a model was developed that fit one overall baseline value to the trace window. It was found that this method worked well, but it did not yield precise enough values that captured the pulse shape in NaI(Tl). This method is shown in Fig. 4.1.

A possible reason was that the NaI(Tl) detector had a decay time longer than the length of the trace window before the baseline returned back to zero could be due to the phosphorescence (afterglow) in the crystal. Due to this, a model was developed that fit **each** pulse with a *pre-* and *post-trigger* baseline, but this just added additional computational time to fit each pulse,

57
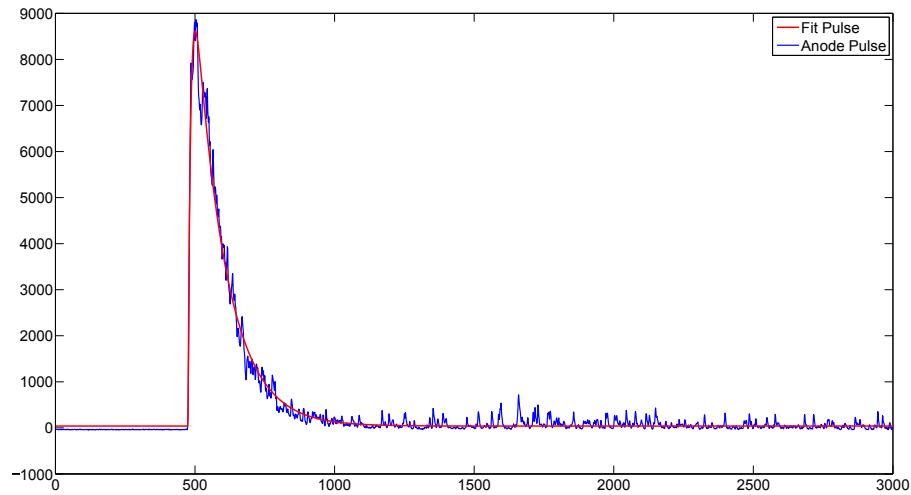
Figure 4.1: Deconvolution algorithm utilizing one baseline value for the entire trace window.

and would give wildly inaccurate baseline values for pulses close in arrival times. When pulses arrived close in time, the algorithm had too much freedom in estimating the multiple baselines and was not suitable for this work. From this result one pair of pre- and post-trigger baseline values were added to the **entire** trace window. The pre-trigger baseline occurs before the arrival time of the first pulse, and this initial pulse will carry a post-trigger baseline through the rest of the trace window. In detectors that have very fast decay times this might not be necessary (i.e. CeBr$_3$), but it still creates a more robust fitting model. Although it was not added into this algorithm, fitting a post-trigger baseline of each additional pulse could more accurately correct the excess charge associated with the baseline under each pulse.

Another important step in correcting the anode pulses for fitting was subtracting the overall baseline from the trace window. This was done by subtracting the pre-trigger baseline from the trace window. The step after baseline subtracting the pulses was to re-evaluate the pre- and post-trigger baseline values to initially guess more accurate fitting parameters. We discussed subtracting both pre- and post-trigger baselines from the pulse, but did not incorporate this into the algorithm yet. In future developments of the algorithm, this will be investigated further

58

and possibly incorporated to correct for the excess charge associated with the piled up baseline of multiple pulses.

The last update to finding correct baseline values was to determine if the baseline values passed were correct. The original algorithm just determined a pair of pre- and post-trigger baselines from the two regions in red in Fig. 3.6 (NaI(Tl)), and Fig. 3.8(CeBr$_3$). In high count rate environments, pulses may come in at the beginning or the end of a trace window as is shown in Fig. 3.5 and Fig. 2.7. Because of this, a more robust check of the baseline values was needed. Although there is no way to capture every possible scenario, the method described in Section 3.4 was found to work very well.

4.2   Constant Fraction Discriminator vs. Differentiator

To extract the maximum amplitude and arrival time of pulses in the trace windows, a constant fraction discriminator (CFD) was used. Fig. 4.2 shows that the CFD could resolve convolved pulses that were separated by approximately 300 ns. This was not robust enough for high count rate applications.

Next, differentiation of the trace windows was applied to find the maximum amplitudes and arrival times of pulses. This method was able to resolve multiple pulses in a trace window that were close in arrival time. For NaI(Tl), using the analytical model with an average $\tau_r = 20ns$ and $\tau_f = 230ns$, with varying amplitudes and arrival times, this method could differentiate pulses separated by approximately 57 ns. This is shown in Fig. 4.3. This is an "ideal" example since the analytical model has no noise in the signal.

For CeBr$_3$, the analytical model used an average $\tau_r = 17ns$ and $\tau_f = 20ns$, with varying amplitudes and arrival times. This method could differentiate pulses approximately 20 ns apart. This is shown in Fig. 4.4. Again, this is an "ideal" example since the analytical model has no noise in the signal.

59
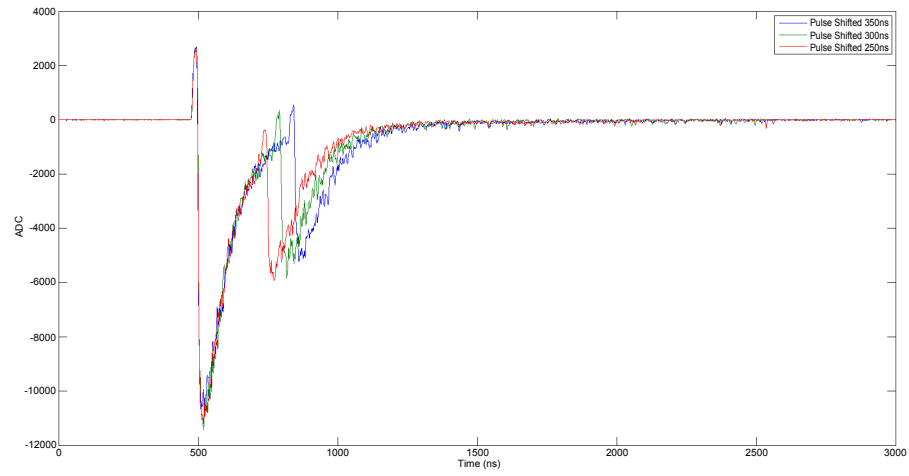
Figure 4.2: Minimum separation time using a CFD on convolved pulses.
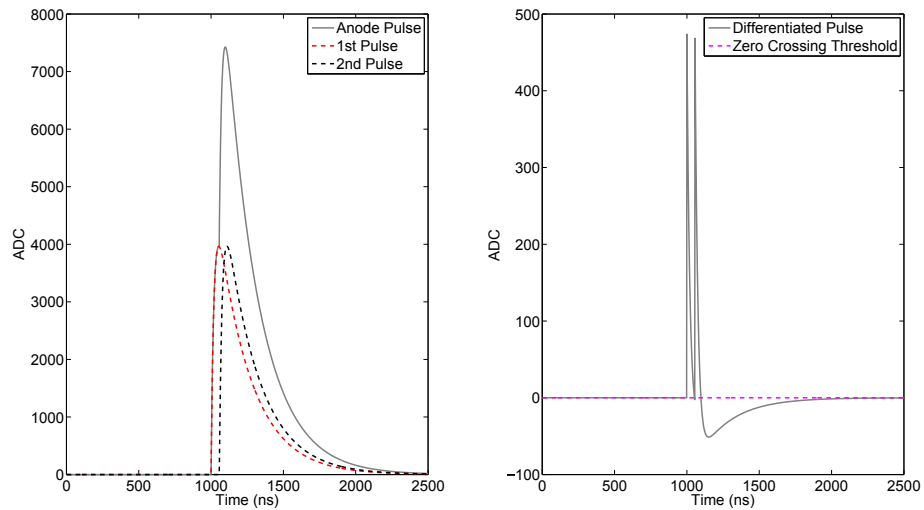
Figure 4.3: Left: NaI(Tl) analytical model of two pulses arriving 57 ns apart. Right: Differentiated pulses crossing zero

60
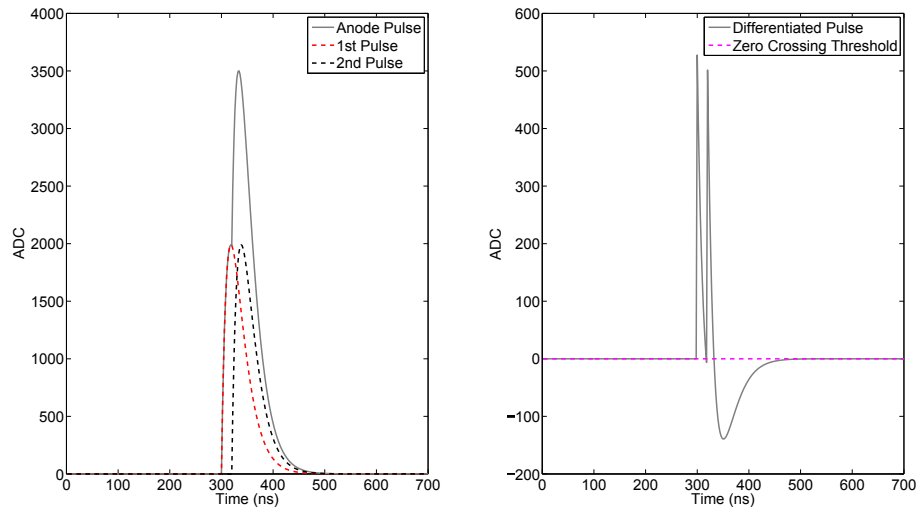
Figure 4.4: Left: CeBr$_3$ analytical model of two pulses arriving 20 ns apart. Right: Differentiated pulses crossing zero

4.3 Pulse Template Fitting vs. Analytical Model Fitting

When this deconvolution algorithm was first being developed, it was initially assumed that each pulses shape was identical and just varied by amplitude. Since, in theory, the system components do not change capacitance or resistance, the only changing variable is the amount of electrons coming from the last dynode of the PMT which is proportional to the energy deposited by the gamma-ray in the crystal. After testing different sources, and separating pulses into different amplitudes, template pulses were created. Fig. 4.5 shows the results of these experiments.

Fig. 4.6 shows a close up of the trailing edges of these templates. It was easily seen that pulses do exhibit longer decay times proportional to the energy of the absorbed gamma-ray. One possibility is that as the energy of the gamma-rays increase, more electrons arrive at the anode at the same time. The increased amount of electrons arriving at the anode may cause a space charge around the anode that does not permit the constant flow of electrons from the last dynode through the anode. This could be the phenomenon that causes the PMT decay time to

61
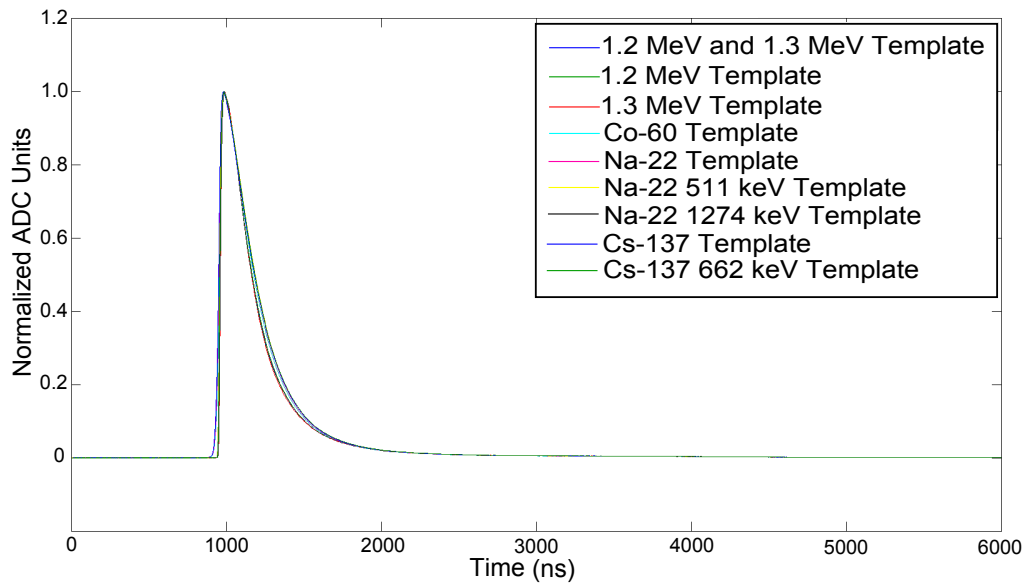
Figure 4.5: Comparison of the NaI(Tl) normalized template spectra taken from different sources and energy ranges.
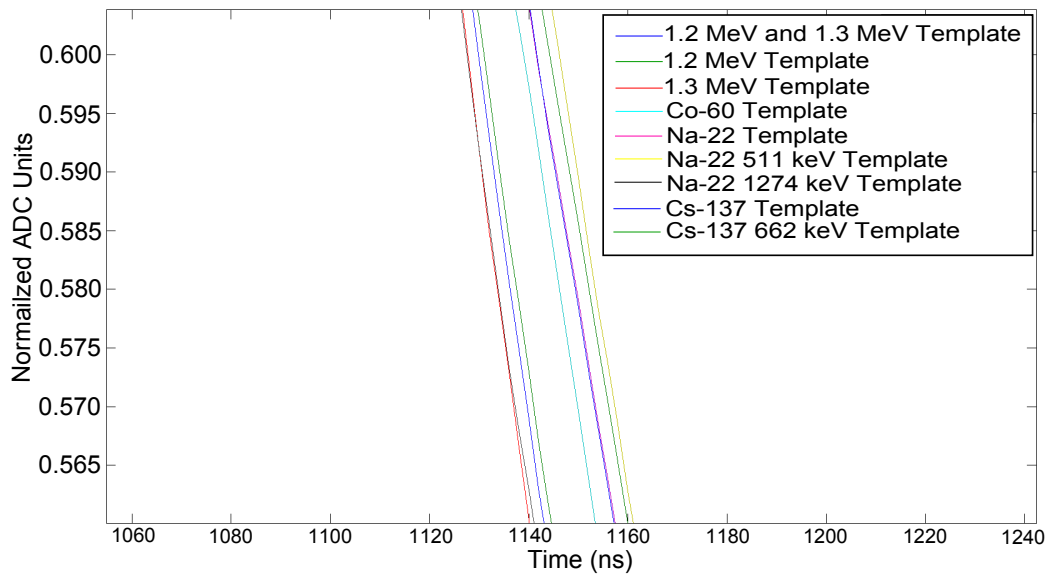
Figure 4.6: A zoom on the trailing edge of the normalized template spectra derived from different radionuclei and their characteristic gamma-ray peaks.

62

appear to increase as pulse amplitude increases.

4.4   Fitting of Analytical Model to NaI(Tl) Pulses

It was important to check the accuracy of the analytical models of the pulse shapes. In Fig.4.7 a single trace window with a single pulse shows the accuracy of the analytical model and fit parameters to the digitized anode pulse. Fig.4.8 shows the accuracy of the algorithm to fit two pulse inside one trace window. In Fig.4.9 the fit of three pulses in one trace window is shown. These figures validate the fit models ability to replicate to the digitized anode pulses from NaI(Tl).
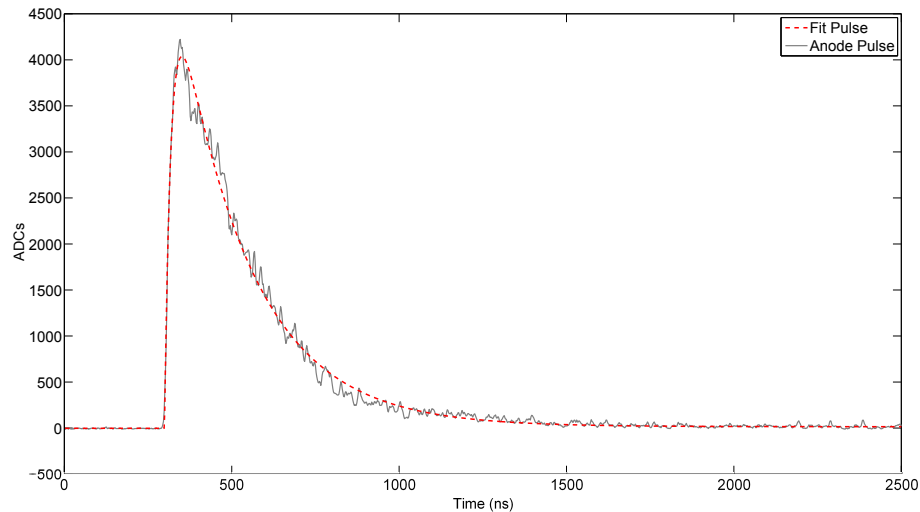
Figure 4.7:   Analytical model fit of a single pulse from NaI(Tl).

In Chapter 2 it was mentioned that NaI(Tl) has an "afterglow". Although much of this "afterglow" just adds a baseline to the pulses some may cause misshaped pulses as seen in Fig. 4.10. Fig. 4.10 was taken from an experiment where a 4mCi ^{137}Cs was 1 foot from the detector. There was only a small number of these pulses, but it still was another issue found using NaI(Tl) in high count rate environments.
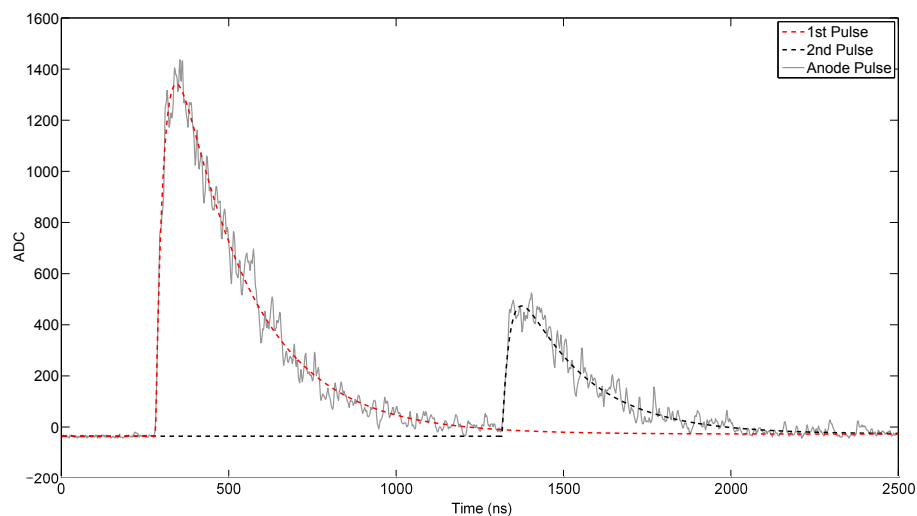
Figure 4.8: Analytical model fit of a double pulse from NaI(Tl).

Another issue with the NaI(Tl) used during this research was the noise in the anode signal. Pulses with higher amplitudes exhibited higher signal-to-noise ratios. Fig. 4.11 shows this noise. The left side of the figure has the higher amplitude pulse and the left side of the figure has the lower amplitude pulse.

The noise was not proportional to the amplitudes, but constant. This put higher uncertainties in the fit parameters of lower amplitude pulses.

65
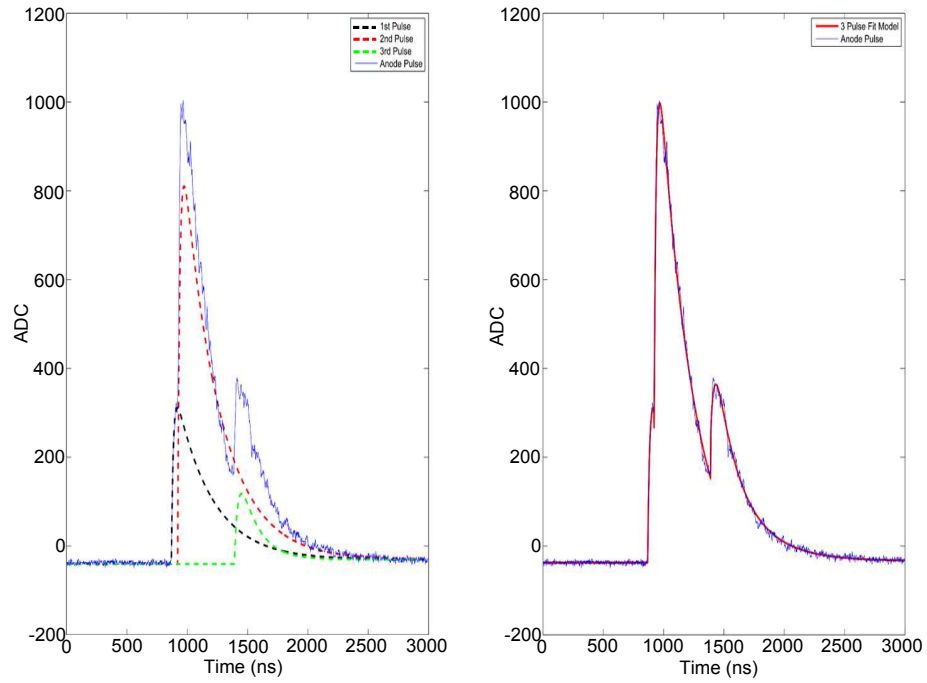
Figure 4.9: Analytical model fit of a triple pulse from NaI(Tl).
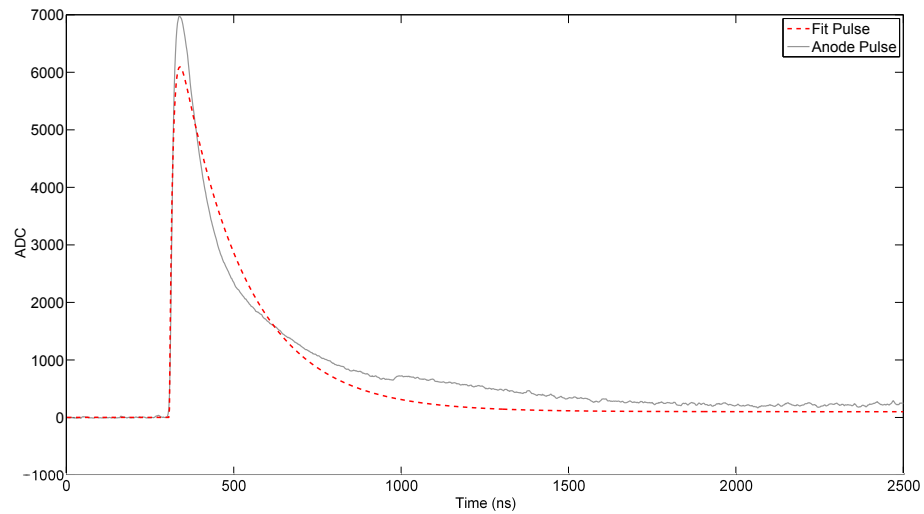
Figure 4.10: Poor pulse fit from NaI(Tl) with 4mCi ^{137}Cs at 1 foot.
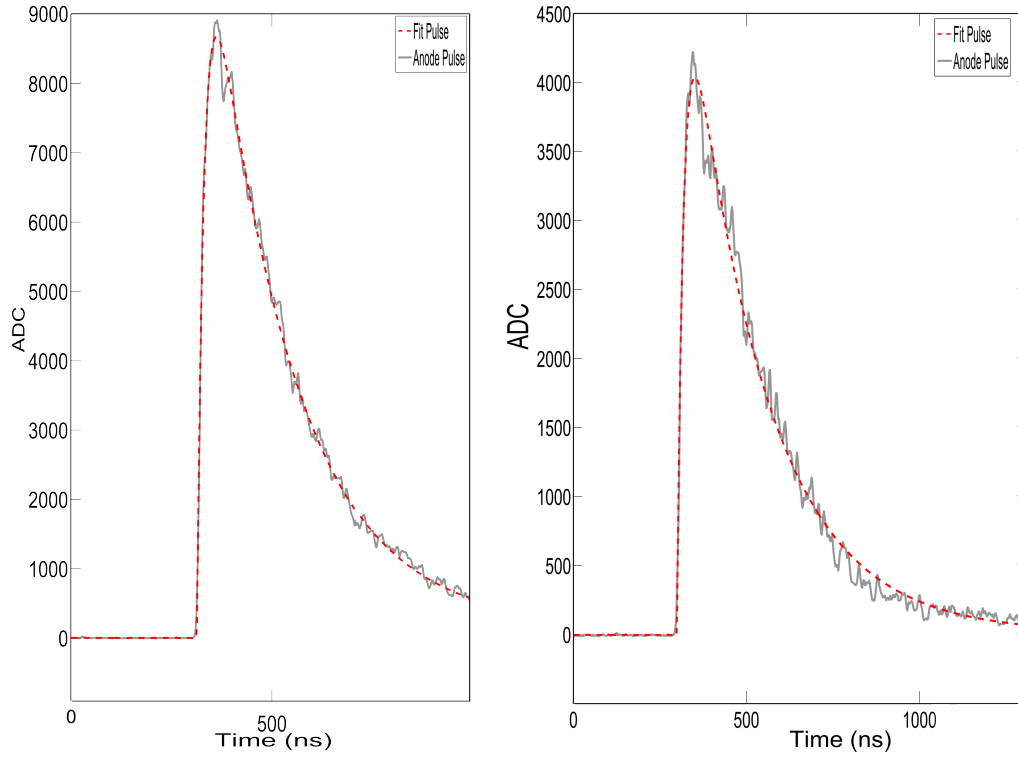
Figure 4.11: Noise comparison of different amplitude NaI(Tl) pulses. Left: High amplitude pulse. Right: Lower amplitude pulse.

4.5 Fitting of Analytical Model to CeBr$_3$ Pulses

Although the analytical model worked well to fit the NaI(Tl) pulses, my research concluded it was not completely correct for CeBr$_3$. It calculated charge (Q) values that were very close, but do miss the complete areas under the pulse, because the analytical model does not correctly capture the pulse shape from this fast detector. Fig. 4.12 shows where the analytical model does not accurately fit the pulse shape from CeBr$_3$. The blue dashed boxes are the regions where the analytical model does not accurately describe the flow of electrons coming from the anode. Recall from Chapter 2 at Eq.2.1, the pulse shape model made the assumption that, "If the spread in transit time of the PMT is small compared to the scintillation decay time, then a realistic model of the electron current arriving at the PMT anode is...[6]" Our CeBr$_3$ uses a Hamamatsu R6231 PMT. The PMT has a typical spread in transit time of 6.9 ns[21]. This means that the Cebr$_3$ scintillation decay time is slightly over two times faster than the typical spread in transit time of the PMT. This is possibly why the leading edge of the pulse shape shows an exponential rise.

The figures from the CeBr$_3$ pulses show the poorly fit pulses from the analytical models. Fig.4.13 shows the single pulse fit model. The poor fit is evident in the leading edge of the pulse and the amplitude of the pulse. Fig.4.14 is a double pulse in one trace window. The fit is very close to the pulse shape, but still lacks the accuracy wanted for this deconvolution algorithm. Fig.4.15 shows the three pulse fit model. Although its poor fit to the analytical model was thought to have 3 pulses in one window, only 2 pulses can be seen. With a better analytical model this might correct this issue with the fitting of the pulses.

Fig.4.16 was fit three times. When the fitter found the minimum values in the residuals, it left a large area above the pulse that was refit two more times due to the residuals left from the poor fittings.

Another pulse shape model was found from research done by M. Nocente, et.al[1, 22]. They used a cerium doped, lanthanum bromide (LaBr$_3$(Ce)) detector, which analogous to CeBr$_3$ is a fast scintillation detector. They digitized the signal from a fast pre-amplifier for fitting. The
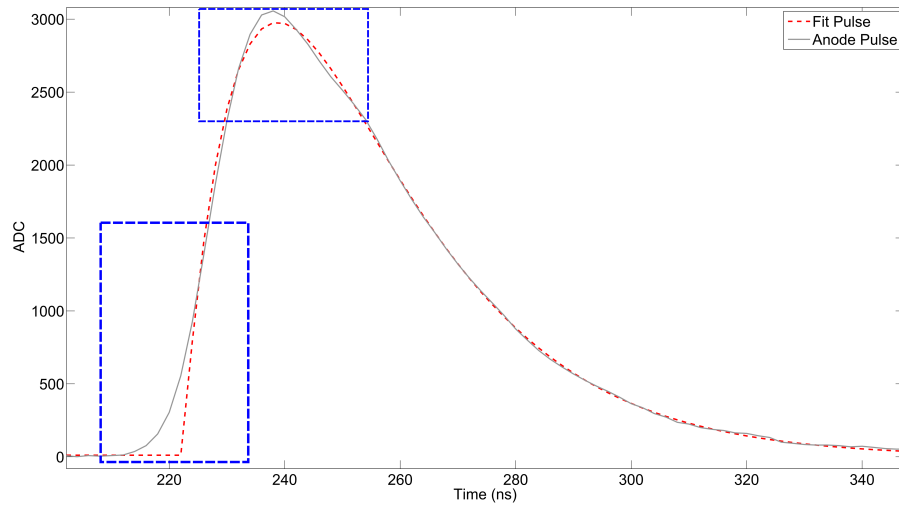
Figure 4.12: CeBr$_3$ pulse overlaid with fit analytical model. The blue dashed boxes on the leading edge and the peak of the pulse show where the analytical model does not fit the pulse shape accurately.
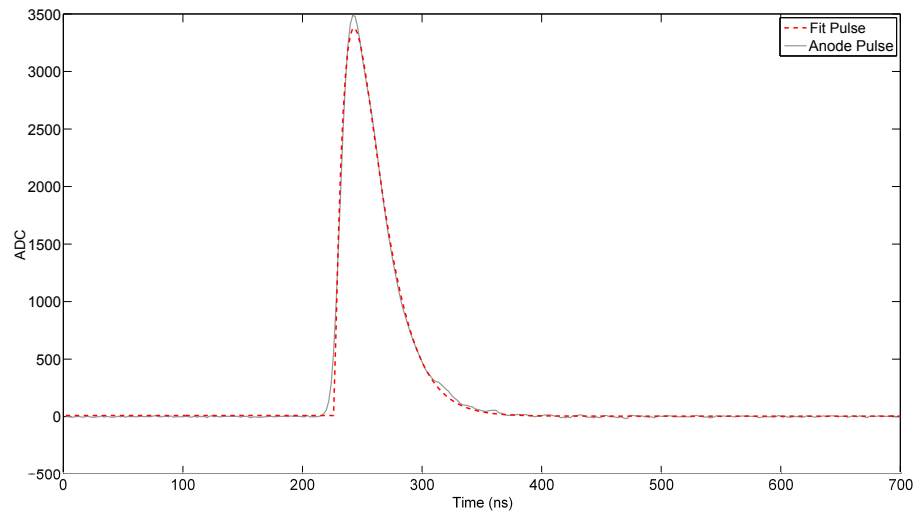
Figure 4.13: Analytical model fit of a single pulse from CeBr$_3$.

69
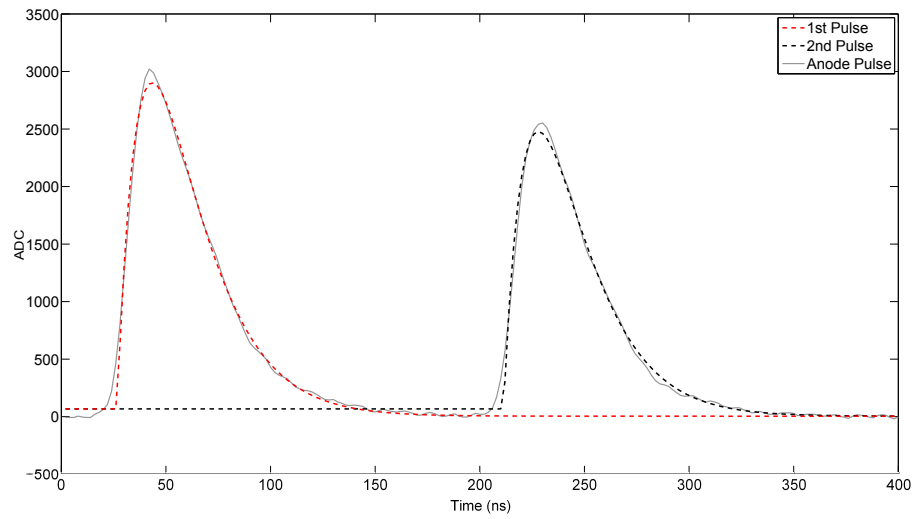
Figure 4.14: Analytical model fit of a double pulse from CeBr$_3$.
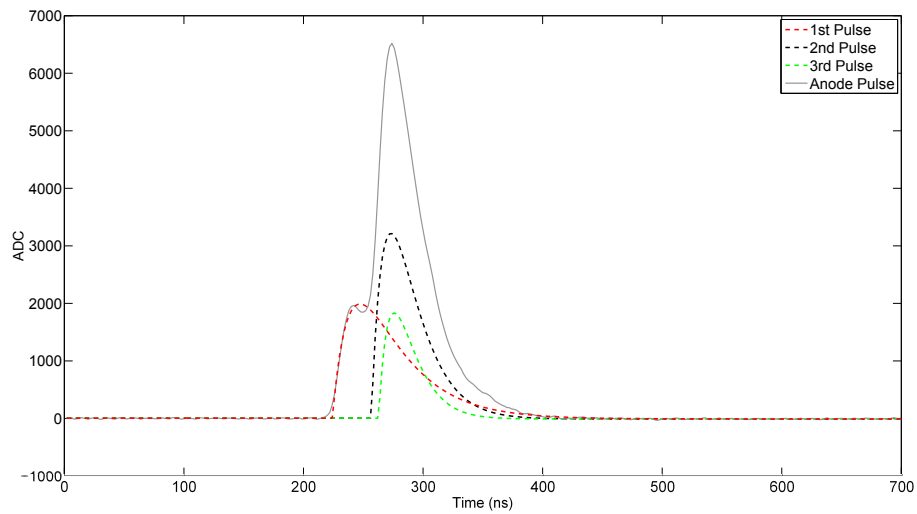
Figure 4.15: Analytical model fit of a triple pulse from CeBr$_3$.

analytical model they used was:
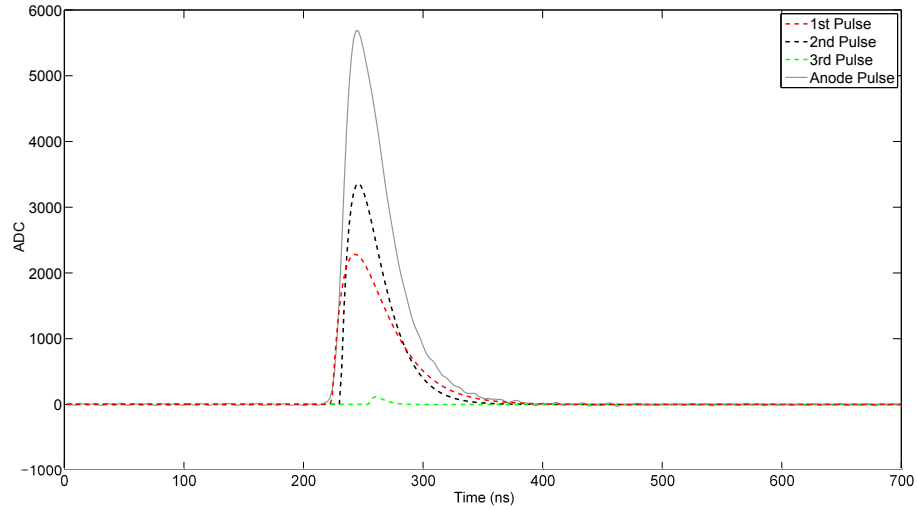
Figure 4.16: Poor analytical model fit of a triple pulse from CeBr$_3$.

$$S(t) = \begin{cases} y_0 & t < t_0 \\ y_0 + N\{1 - e^{-\frac{t-t_0}{\tau_1}}\}^P e^{-\frac{t-t_0}{\tau_2}} & t > t_0. \end{cases} \tag{4.1}$$

Nocente's models used fixed values for τ_1, τ_2 and P, the fit the parameters y_0, N, and t_0. His model fits the pulse shape, but to do this Nocente utilized a mathematical equation that fit the pre-amplified pulse shape, but contained a value P that has no physical relation to the scintillator, PMT, or pre-amplifier dynamics. His assumptions concluded that pulse shape does not depend on incoming gamma-ray energy, and therefore he and his colleagues could fix some values that our research fit independently. Fig.4.17, and Fig.4.18 shows Nocente's model fit to the anode pulse from CeBr$_3$. It can be seen that both fits lack a proper analytical model that captures the waveform from the anode. They are both similar, but still not completely accurate. It was also evident that Nocente's model does not accurately describe the values used in the model, but simply uses a model that incorporates scintillation and detector characteristics and then uses some mathematical manipulations to create a shape that resembles the waveform. In

71

Table 4.1: Nocente Pulse Shape Model Fit Parameters for Fig.4.17 and Fig.4.18. Values annotated with a * are constants.

Fit Parameter	Fig.4.17	Fig.4.18
y_0	0	0
N	35,000	10,000
$t_0(ns)$	214	208
$\tau_1^*(ns)$	17	20
$\tau_2^*(ns)$	17	20
P^*	3.5	3.5

Fig.4.17 the values passed from Eq.4.1 are shown in Table 4.1.

The N values shown in Table 4.1 seem to not correspond to the ADC values from the digitizer. Although the pulse shape is similar, Nocente's analytical model does not capture the true values of the anode pulse.
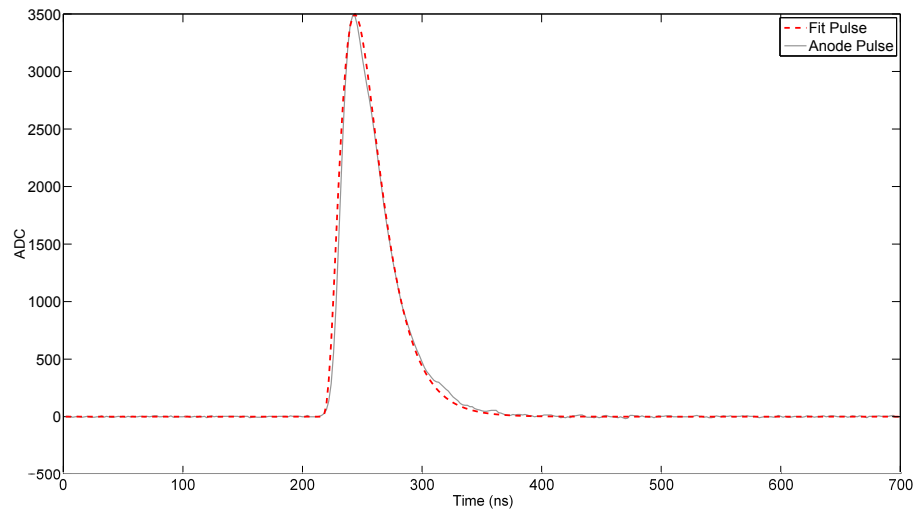
Figure 4.17: Nocente pulse shape model fit of a single pulse from CeBr$_3$.
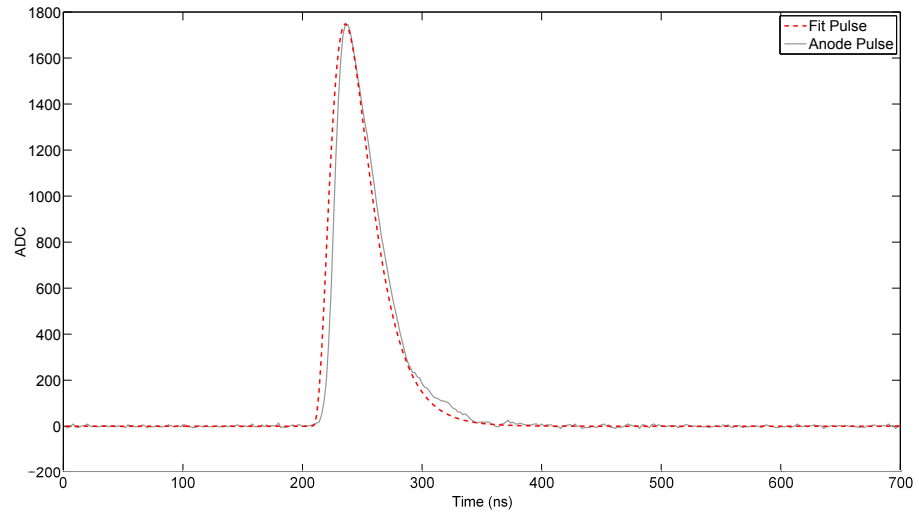
Figure 4.18: Nocente pulse shape model fit of a single pulse from CeBr$_3$.

73

4.6 Levenberg-Marquardt vs. Trust Region Reflective Algorithm

When fitting multiple pulses in a single window using the Levenberg-Marquardt (L-M) algorithm, it was found that this method sometimes failed to converge or produce physical solutions for some parameters. L-M is an unconstrained, damped nonlinear least squares fitting algorithm[23, 24]. This became problematic when some guessed parameters led the solver to produce infinite values which crashed the algorithm. Although our research showed that pulse shapes do not have constant decay times, it did show that there is a region of values that the pulse shapes will take depending on the pulses amplitude. For this reason a trust-region reflective (TRR) algorithm was used instead[14, 15, 16, 17, 18, 19]. This allowed for constraints to be placed on the fit parameters to allow enough freedom to accurately shape the pulse and not produce unrealistic pulse parameters. Table 4.2 shows the constraints used for each parameter in the TRR algorithm. The parameters constraints could be optimized to lessen the amount of computational time, but for the purposes of this research more freedom was given to see how the fitting algorithm would handle these types of solutions.

Table 4.2: TRR pulse parameter constraints for NaI(Tl) and CeBr$_3$.

Parameter Upper/Lower Limits	NaI(Tl)	CeBr$_3$
Amplitude (ADCs)	0/50000	0/40000
Baseline (ADCs)	-100/100	-200/200
Time (ns)	1/2500	1/700
τ_r (ns)	10/80	1/50
τ_f (ns)	100/600	1/100

4.7 Root Mean Square Error vs. Relative Uncertainty

The first check used the root mean squared error (RMSE) from the goodness-of-fit results from the first trace window fitting. When the RMSE was below a threshold level, it indicated a good fit from the model to the digitized pulse. It became evident early in the deconvolution algorithm development that this check was not robust enough to determine the goodness-of-fit for some parameters. The RMSE is a value that is derived from the residual left between the digitized pulse and fit model. Trials showed that trace windows with multiple pulses could contain low RMSEs, but yielded inaccurate pulse parameters. Some pulses could be fit with "unlikely" fit parameters, but still pass the RMSE check. This prompted the use of the checking the relative uncertainties of some of the fit parameters. This allowed individual fit parameters to be checked for their precision. Fig. 4.19 shows where the fit parameters from the first pulse are unlikely to be correct. The first pulse had a PMT decay time well above an acceptable value.

If this method was similar to the work of Nocente, the RMSE check would be sufficient since the only fit parameters are amplitude, baseline, and pulse arrival time. The RMSE could accurately determine whether the trace window contained a good fit. Since the deconvolution algorithm is fitting τ_r and τ_f using values that are not constant, but "live" in a range that can be seen in Fig. 3.13 and Fig. 3.14 for NaI(Tl) and in Fig. 3.15 and Fig. 3.16 for CeBr$_3$. This gives credence to the use of using the relative uncertainties for determining the goodness-of-fit of trace windows over the use of the RMSE for the goodness-of-fit.
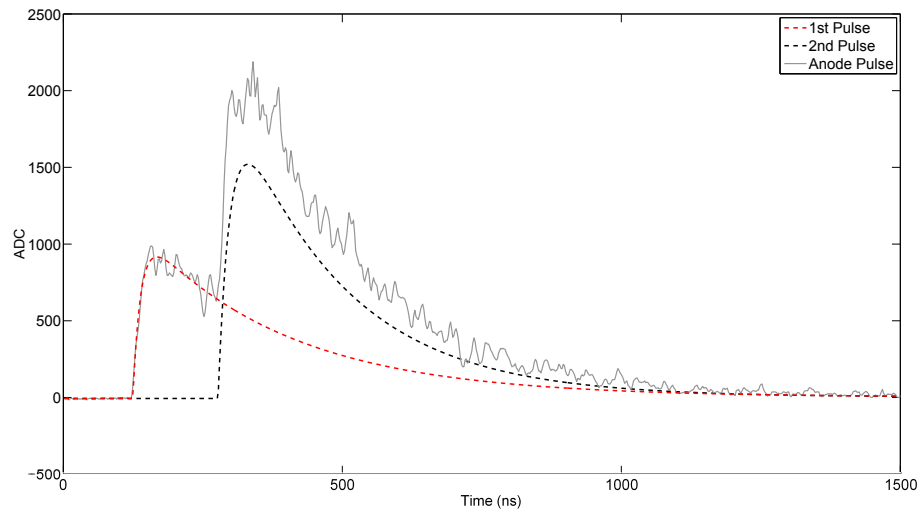
Figure 4.19: Poor pulse fitting using the RMSE to check the goodness-of-fit.

Chapter 5

Results

5.1   Results

The first experiments conducted used 5μCi ^{60}Co, ^{22}Na, and ^{137}Cs calibration sources. These were used to verify that the analog PHS collected matched the fit PHS collected from the Pixie-500. Each of these measurements used a source-to-detector distance of 5 inches and ran for 5 minutes. In each figure the analog PHS is colored blue and the fit PHS is colored green.

To verify the deconvolution algorithm a 4mCi ^{137}Cs source was used. The analog PHS had live run times of 600 s. Fit PHS had live run times of 300 s. This source emits approximately $1.48 \times 10^{8} \gamma/s$. Since the source has isotropic emission distribution, Table 5.1 has the approximate gamma-ray currents at each distances based on the solid angle subtended by a 50.8mm (diameter) $\times$ 50.8mm (long) detector and a 38.1mm (diameter) $\times$ 38.1mm (long) detector.

Table 5.1: Approximate gamma-ray currents at different distances from a 4mCi ^{137}Cs source seen by a 50.8mm (diameter) × 50.8mm (long) detector and a 38.1mm (diameter) × 38.1mm (long) detector.

	Average Current (γ/s)	
Source-to-Detector Distance (Feet)	50.8mm × 50.8mm	38.1mm × 38.1mm
Detector Type	NaI(Tl)	CeBr$_3$
5	10,300	5,800
3	28,550	16,050
1	255,600	144,110

5.2   5μCi Calibration Source Spectra using NaI(Tl)

Fig. C.2 in Appendix C shows the setup of the 5μCi experimental runs. Figs. 5.1 - 5.3 shows the NaI(Tl) spectra from the MCA in blue, and the fit spectra in green. Although the number of counts is lower in the fit spectra than the MCA's spectra, the important features of the fit spectra have been preserved. Therefore the deconvolution algorithm effectively fit individual pulses and re-created a PHS from the data.

One area where the spectra differ is in the lower energy region. This was due to the NaI(Tl) detectors being used having noise in the signal. To eliminate these noise triggers, a higher energy threshold was set on the Pixie-500 which omitted these low amplitude noise pulses. This created a loss in information at low energies in the PHS.
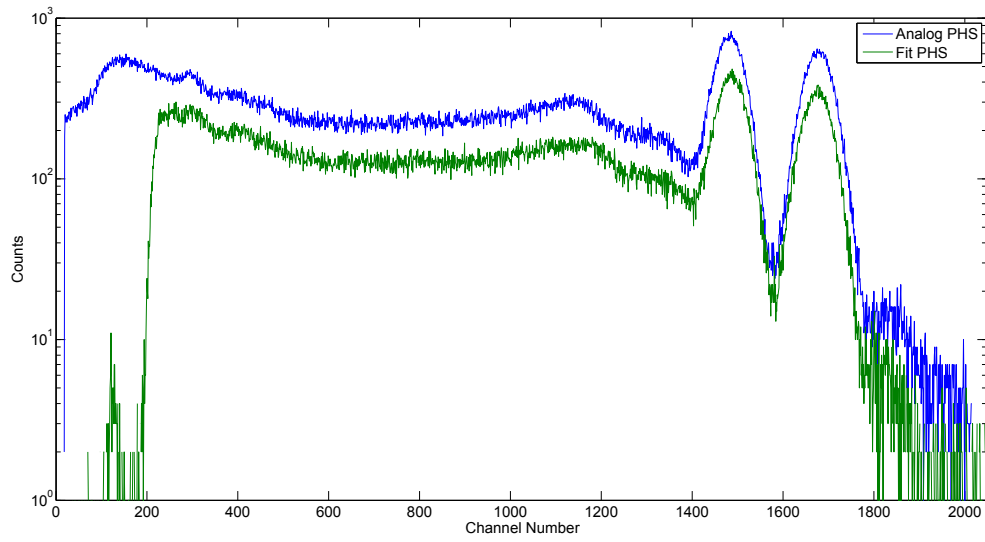
Figure 5.1: Comparison of analog NaI(Tl) PHS to fit PHS of 5μCi ^{60}Co at 5 inches.
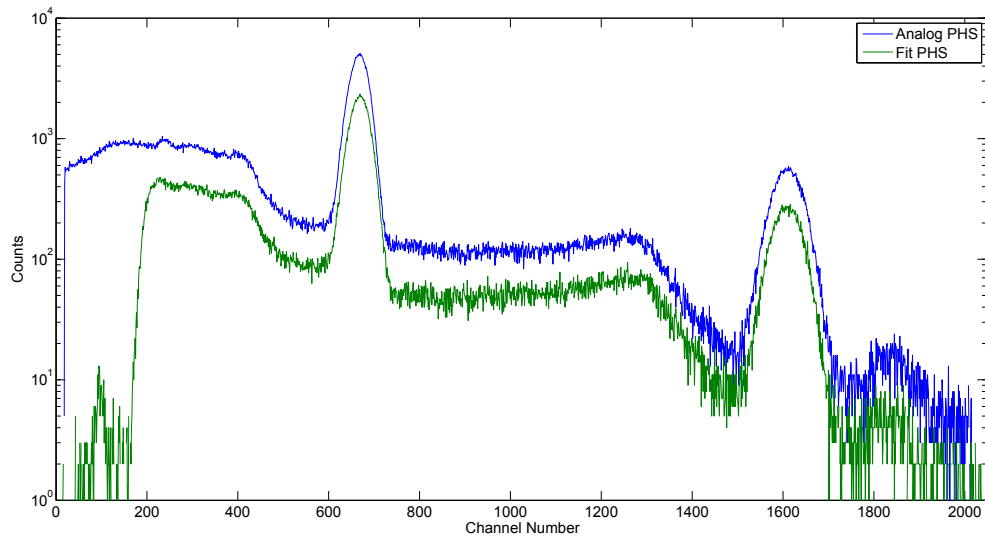
Figure 5.2: Comparison of analog NaI(Tl) PHS to fit PHS of 5μCi ^{22}Na at 5 inches.

www.manaraa.com
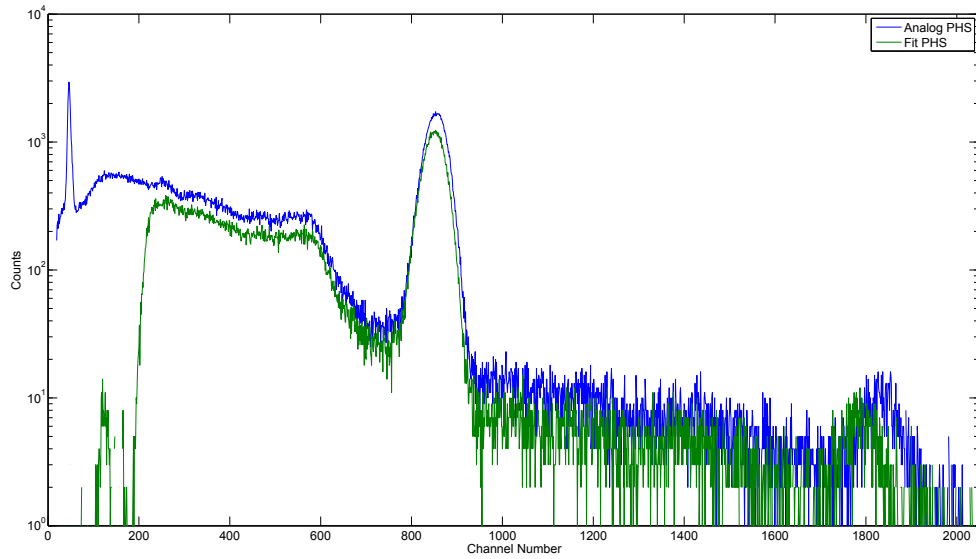
Figure 5.3: Comparison of analog NaI(Tl) PHS to fit PHS of 5μCi ^{137}Cs at 5 inches.

5.3 5μCi Calibration Spectra on CeBr$_3$

Figs. 5.4 - 5.6 show the CeBr$_3$ spectra from the MCA in blue, and the fit spectra in green. Unlike the NaI(Tl) detector, the CeBr$_3$ had little to no noise and this allowed a lower energy threshold to be used on the Pixie-500 that allowed a more complete PHS to be created at lower energies. Although the number of counts is again lower in the fit spectra than the MCA's spectra, the important features of the fit spectra have been preserved. These figures credit the ability of the deconvolution algorithm to effectively fit individual pulses and re-create a PHS from the data.

80
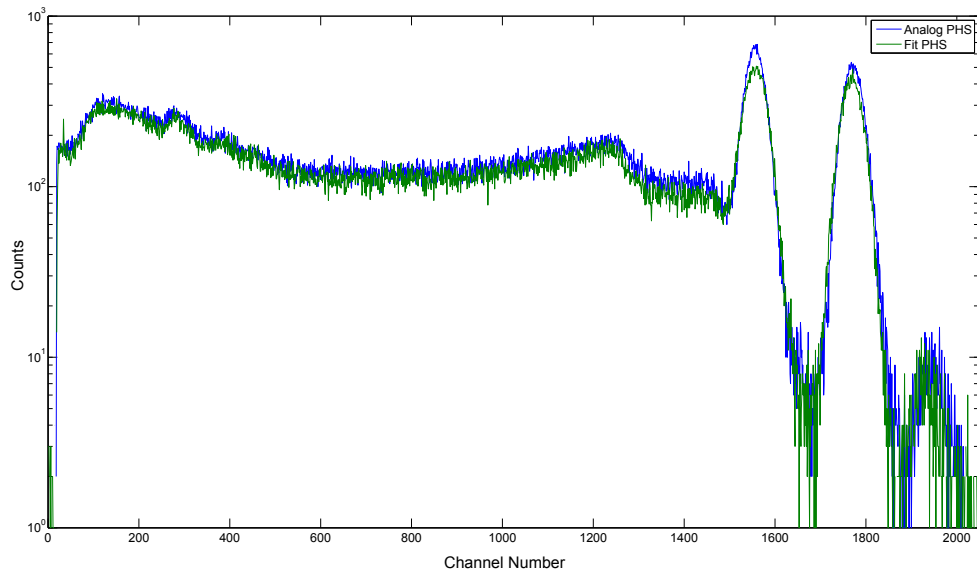
Figure 5.4: Comparison of analog CeBr$_3$ PHS to fit PHS of 5μCi ^{60}Co at 5 inches.
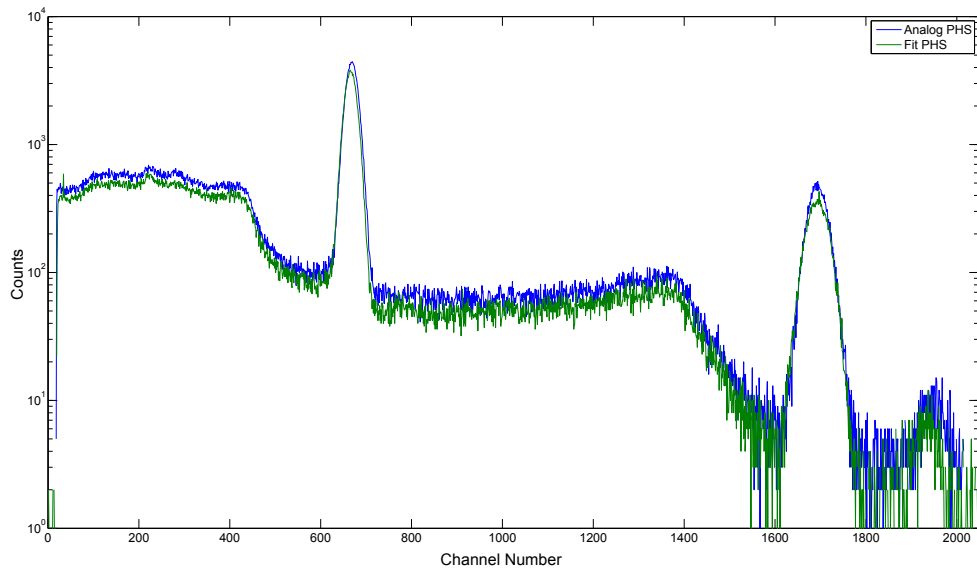
Figure 5.5: Comparison of analog CeBr$_3$ PHS to fit PHS of 5μCi ^{22}Na at 5 inches.

81
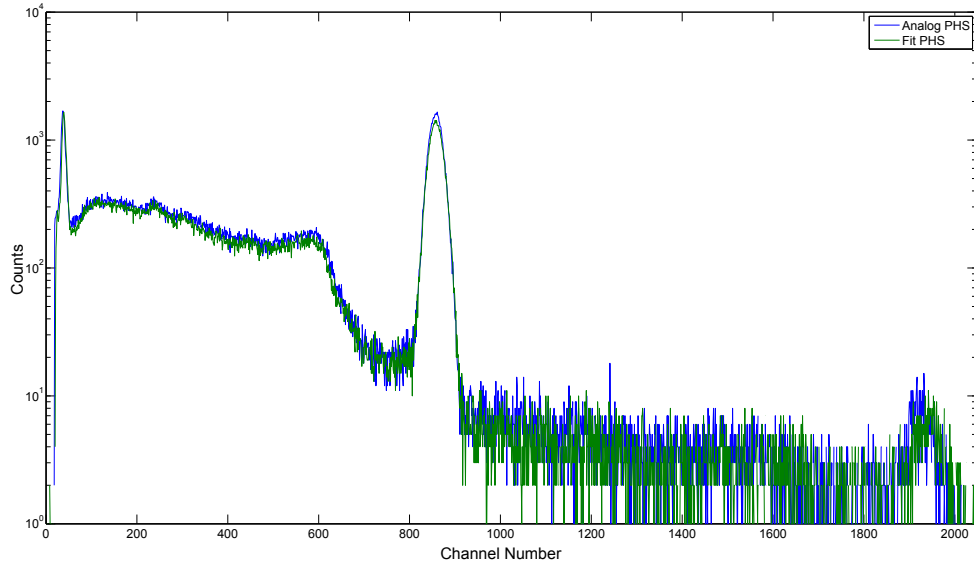
Figure 5.6: Comparison of analog CeBr$_3$ PHS to fit PHS of 5μCi ^{137}Cs at 5 inches.

5.4 4mCi ^{137}Cs on NaI(Tl)

Table 5.2 shows the number of trace windows with 1, 2, and 3 pulses per window from the 4mCi ^{137}Cs, NaI(Tl) runs.

Fig.5.7 shows the analog PHS and fit PHS at 5 feet are similar, and the fit PHS contains very little pileup as is shown in the analog PHS. The analog PHS contained 5,386,936 pulses where the fit PHS contained 566,845 pulses.

As the source-to-detector distance is shortened to 3 feet, Fig.5.8 shows the characteristic ^{137}Cs peak shifting higher in the fit PHS, but with no piled up pulses. The analog PHS shows that the characteristic 662 keV peak has not shifted. Due to the higher count rates, the afterglow associated with the NaI(Tl), and effects from increased amount of electrons in the PMT, it seems reasonable to conclude that the algorithm is correctly fitting. In an analog PHS the afterglow usually just manifests itself as a gain shift in the spectrum. Due to the non-linearity in light emission of NaI(Tl) and the phosphorescent states of NaI(Tl) it is very possible that the shifting

82

Table 5.2: Number of trace windows containing single, double, and triple pulses per window for the 4mCi ^{137}Cs runs with NaI. Distance here refers to the source-to-detector distance.

Distance (Feet)	5	3	1
Original Number of Windows	567,552	570,240	570,816
Fitted Number of Windows	566,845	569,045	554,354
Percentage of Rejected Windows (%)	0.125	0.210	2.88
Single Pulse Windows	562,827	563,113	499,336
Double Pulse Windows	3,797	5,422	51,699
Triple Pulse Windows	221	510	3,319
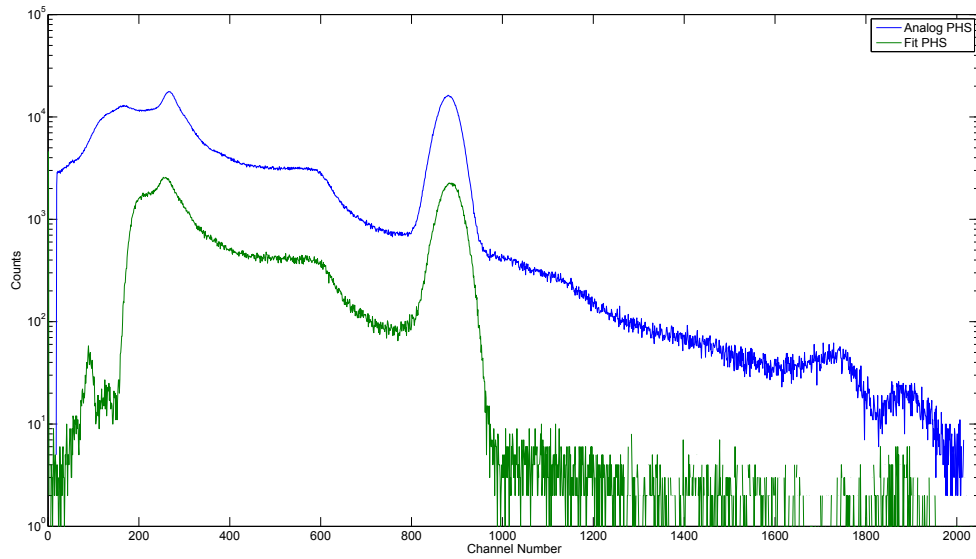
Figure 5.7: Comparison of 10 minute analog NaI PHS to 5 minute fit PHS of 4mCi ^{137}Cs at 5 feet.
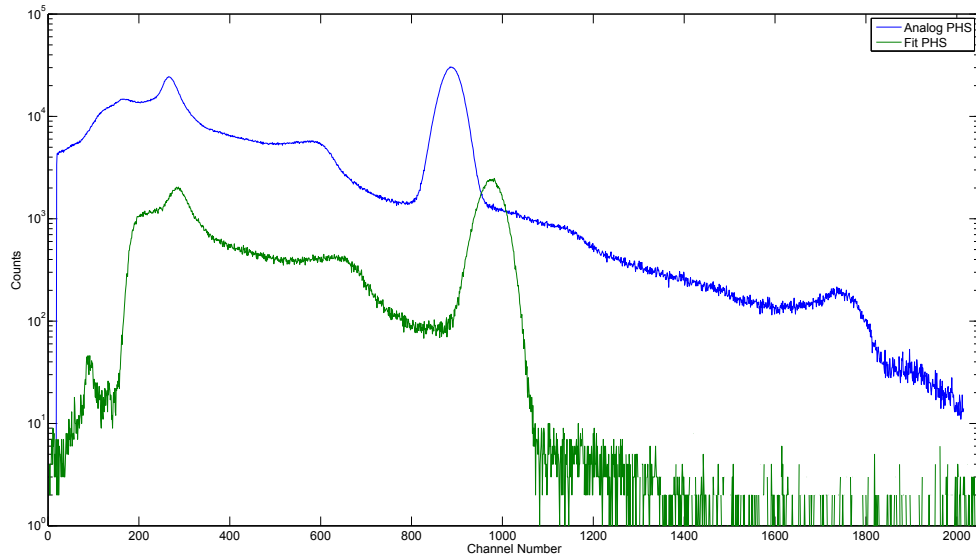
Figure 5.8: Comparison of 10 minute analog NaI PHS to 5 minute fit PHS of 4mCi ^{137}Cs at 3 feet.

peak in the fit PHS were fit correctly and our NaI(Tl) detector is just not suitable in high count rate environments. The analog PHS contained 8,268,543 pulses where the fit PHS contained 569,045 pulses.

When the source is moved to 1 foot, Fig.5.9 shows the analog PHS becoming overwhelmed with pulse pileup due to the higher number of counts above 662 keV than in previous analog PHS, and spectrum is shifted to the right which indicates more charge was collected for each incoming pulse. This shift could also be partly due to the afterglow associated with NaI(Tl) in high count rate environments. The fit PHS looks like it has broken down. A possibility is that the current limit was reached in the digitizer that caused a failure in the fitting algorithm. Dr. Hennig suggested that the Pixie-500 may have rejected most of the pulses due to flat-top rejection checks that were never digitized and recorded. Fig. 2.7 shows a sample from this experiment and the amount of low amplitude pulses in one trace window. For digitizing the NaI(Tl) signal with our settings, it looked like the Pixie-500 was limited to approximately

84
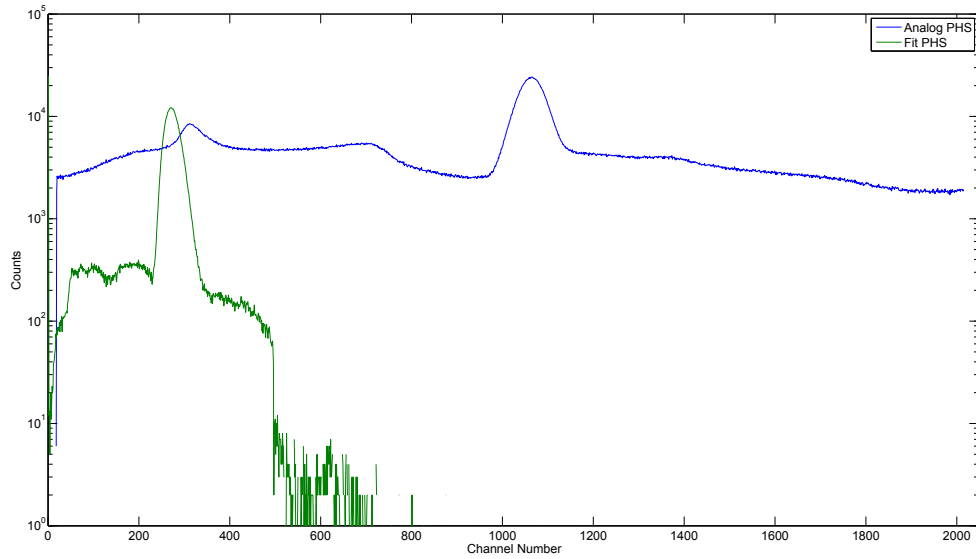
Figure 5.9: Comparison of 10 minute analog NaI(Tl) PHS to 5 minute fit PHS of 4mCi ^{137}Cs at 1 foot.

570,000 traces. The analog PHS contained 8,884,630 pulses and the fit PHS contained 554,354 pulses.

Fig.5.10 shows all the analog NaI(Tl) pulse height spectra for a comparison. Fig.5.11 is a comparison of all of the fit pulse height spectra. The PHS showed a steady increase in the Q values. This could be attributed to an increasing afterglow as the count rate increases. Another possibility is a gain shift in the PMT. Work done by S.M. Robinson, et.al states, " As the count rate increases, the late-stage dynode voltages may droop if the current generated in electron multiplication exceeds the bias network's ability to replenish the dynode, upsetting the voltage distribution throughout the divider network and thereby creating an effective gain shift in the measured spectrum[7]." This was also investigated by M. Tardocchi on LaBr$_3$(Ce) in high count rate environments[10]. Table 5.3 shows the analog and fit PHS's full width half maximum (FWHM) and resolution at 662 keV at varying distances and source strengths. Although the analog PHS looks to have a more stable resolution, it is somewhat false due to the amount of

85
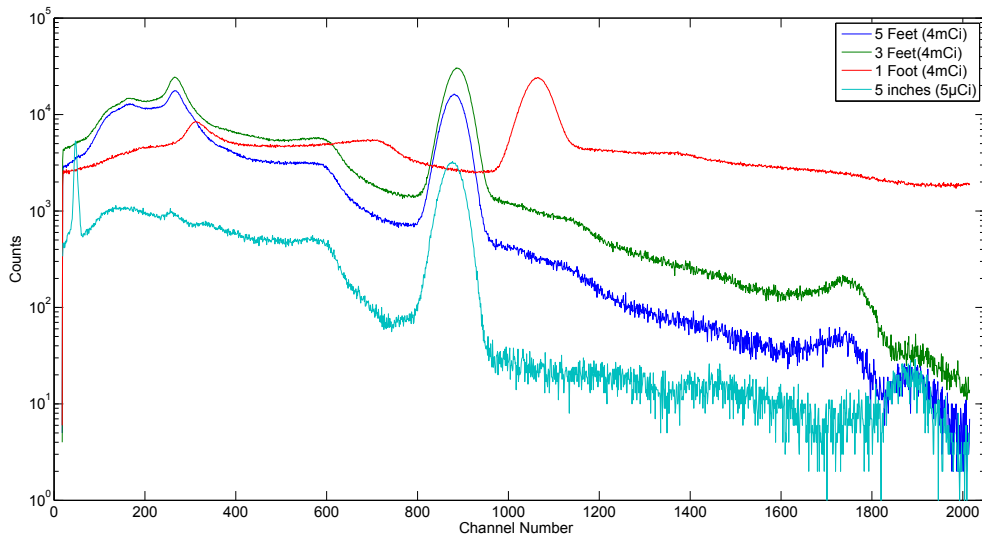
Figure 5.10: Comparison of analog NaI(Tl) PHS of 4mCi ^{137}Cs at 5 feet, 3 feet, and 1 foot along with a 5μCi ^{137}Cs at 5 inches.

pileup in the PHS making a true FWHM measurement correct. The fit PHS shows a marked improvement in the resolution at low count rates, but a lower resolution when medium to high count rates were measured. At one foot the captured waveforms did not provide useful or meaningful data for an accurate PHS. It was thought that the digitizer might have been overwhelmed with flat-top pulses that it rejected in its own algorithms that was never digitized and sent for post-processing.

www.manaraa.com

Figure 5.11: Comparison of fit NaI(Tl) PHS of 4mCi ^{137}Cs at 5 feet, 3 feet, and 1 foot.

Table 5.3: NaI(Tl) fit and analog PHS's FWHM and resolution at 662 keV with different source strengths of ^{137}Cs and varying source-to-detector distances.

	Analog PHS				Fit PHS			
Distance	5 inches	5 feet	3 feet	1 foot	5 inches	5 feet	3 feet	1 foot
Source Strength	5μCi	4mCi	4mCi	4mCi	5μCi	4mCi	4mCi	4mCi
FWHM (keV)	42.04	42.51	42.49	42.80	41.14	43.10	43.11	N/A
Resolution (%)	6.35	6.42	6.42	6.47	6.22	6.51	6.51	N/A

87

5.5   4mCi ^{137}Cs on CeBr$_3$

Table 5.4 shows the number of trace windows with 1, 2, and 3 pulses per window. As the count rate increases the collected counts increase along with multiple pulses per window.

Although some breakdown occurred in the NaI(Tl) at higher count rates, CeBr$_3$ showed a more positive result from the fit PHS. Although it was found that the CeBr$_3$ pulse shape did not as closely fit the analytical model derived in Chapter 2, the model was able to output the charge collected (Q) values very close to the actual Q values from the pulses.

Starting at 5 feet, Fig.5.12 shows good agreement between the analog PHS and the fit PHS. The analog PHS collected 3,301,274 pulses while the fit PHS contained 905,937 pulses.

At 3 feet Fig.5.14 shows where the analog PHS has a slight gain shift to the right. This is most likely due to the increased count rates not allowing the amplifier enough time to return to zero which causes an increased baseline that shifts the PHS. The high number of pulses can be seen in Fig. 5.13 which shows a screen capture from the amplifier signal.

The analog PHS contained 5,037,831 pulses and the fit PHS contained 1,058,090 pulses.

At 1 foot, Fig.5.17 the analog PHS has broken down and is dominated by low amplitude pulses. This was because the pre-amplifiers' current limit of 9μCoulombs/s[25] was exceeded. This caused the pre-amplifier signal to become low amplitude current pulses. Fig. 5.15 is the

Table 5.4: Number of trace windows containing single, double, and triple pulses per window for the 4mCi ^{137}Cs runs with CeBr$_3$.

Source-to-Detector Distance (Feet)	5	3	1
Original Number of Windows	908,038	1,061,040	1,995,168
Fitted Number of Windows	905,937	1,058,090	1,985,555
Percentage of Rejected Windows (%)	0.231	0.278	0.481
Single Pulse Windows	904,516	1,055,549	1,959,717
Double Pulse Windows	1,223	2,225	23,485
Triple Pulse Windows	198	316	2,353
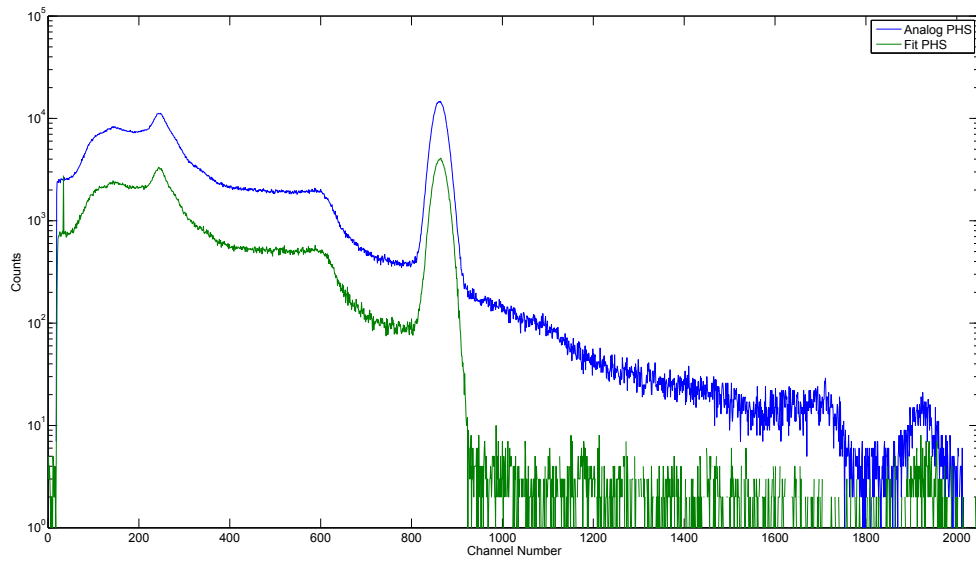
Figure 5.12: Comparison of 10 minute analog CeBr$_3$ PHS to fit PHS of 4mCi ^{137}Cs at 5 feet.
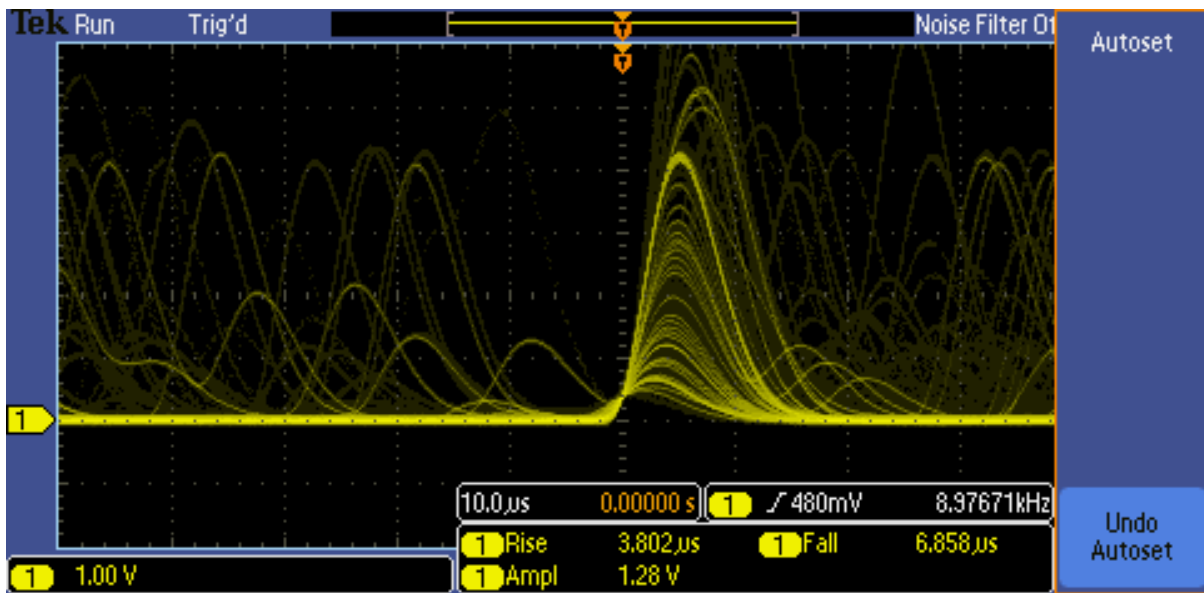
Figure 5.13: Screen capture from the oscilloscope of the amplifier's signal with the 4mCi ^{137}Cs at a source-to-detector distance of 3 feet.
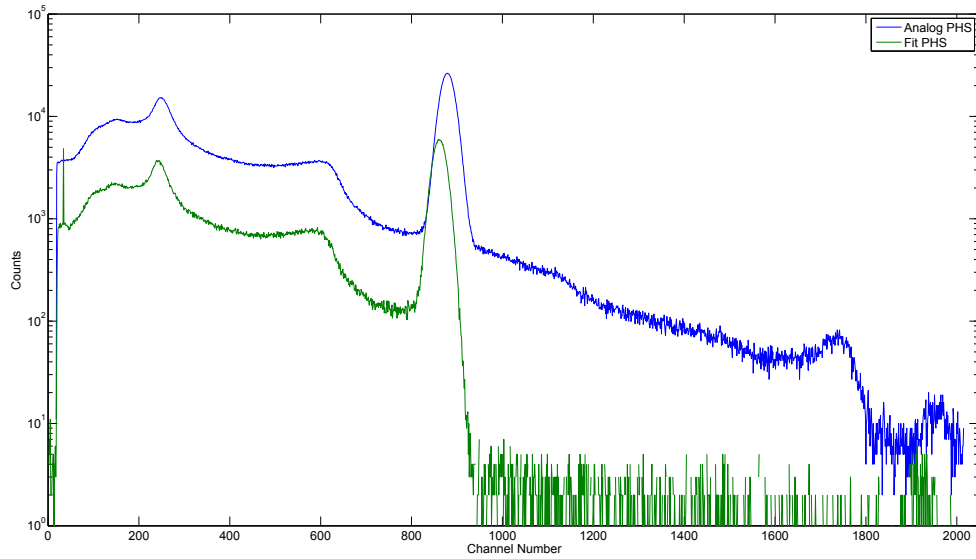
Figure 5.14: Comparison of 10 minute analog CeBr$_3$ PHS to fit PHS of 4mCi ^{137}Cs at 3 feet.

oscilloscope's trace from the pre-amplified signal. The amplified signal can be seen in Fig. 5.16. The analog PHS collected 15,976,087 pulses and the fit PHS contained 1,985,555 pulses.

Fig.5.18 shows the shifting in the PHS of the analog data by comparing the spectra to the others.

To show that the deconvolution algorithm has worked, Fig.5.19 shows that no matter what the input count rate was, the algorithm was able to extract the pulses and create an un-shifted PHS. Table 5.5 shows the full width half maximum (FWHM), and resolution of the 662 keV peak taken from the fit spectra shown in Fig. 5.19 and the analog spectra in Fig. 5.18. The fit spectra had a steadier resolution whereas the analog spectra were getting lower resolution more rapidly until a break down in the PHS.

90
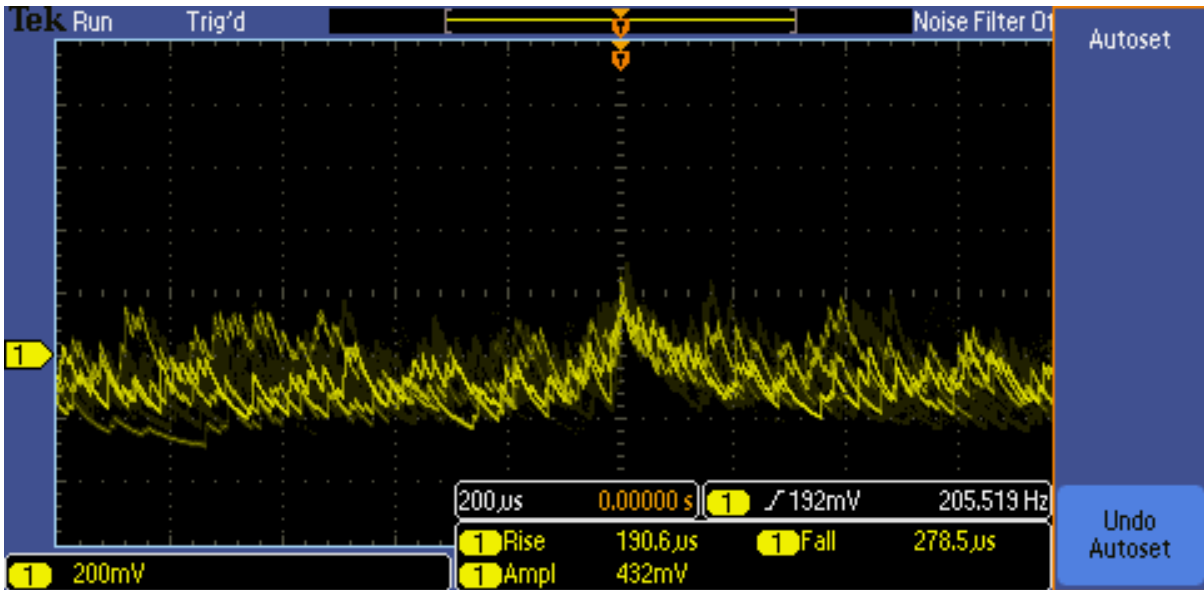
Figure 5.15: Screen capture from the oscilloscope of the pre-amplifier's signal with the 4mCi ^{137}Cs at a source-to-detector distance of 1 foot.
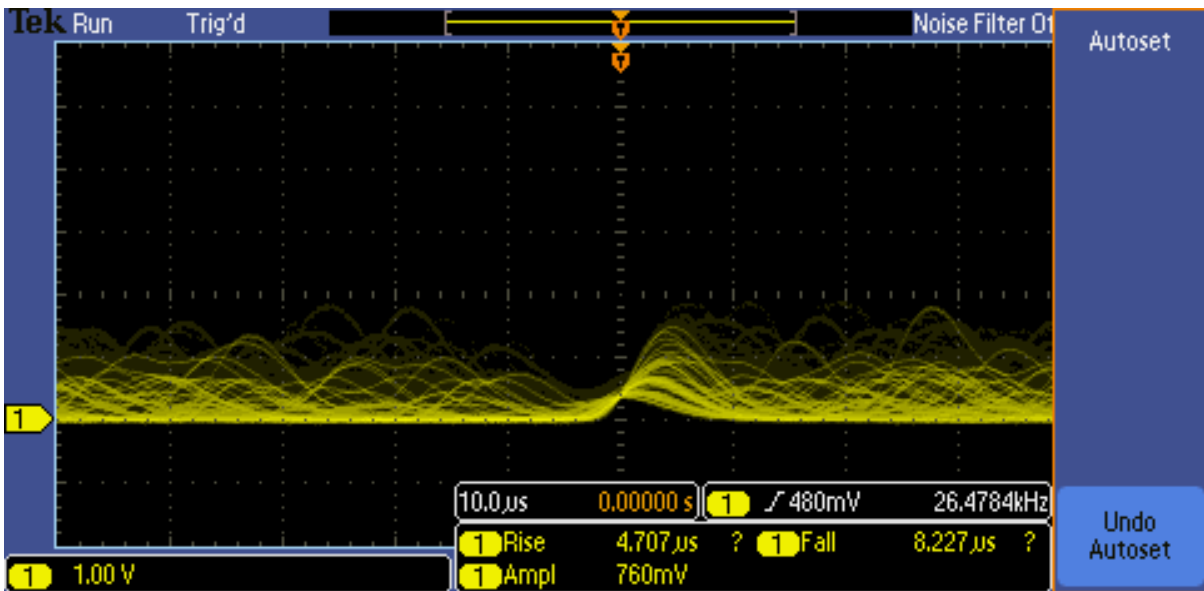
Figure 5.16: Screen capture from the oscilloscope of the amplifier's signal with the 4mCi ^{137}Cs at a source-to-detector distance of 1 foot.
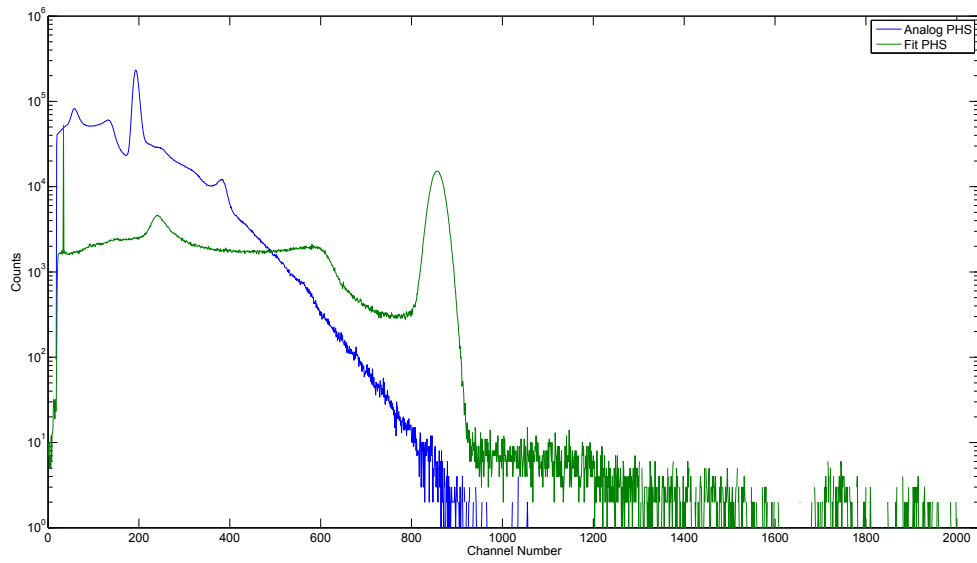
Figure 5.17: Comparison of 10 minute analog CeBr$_3$ PHS to fit PHS of 4mCi ^{137}Cs at 1 foot.
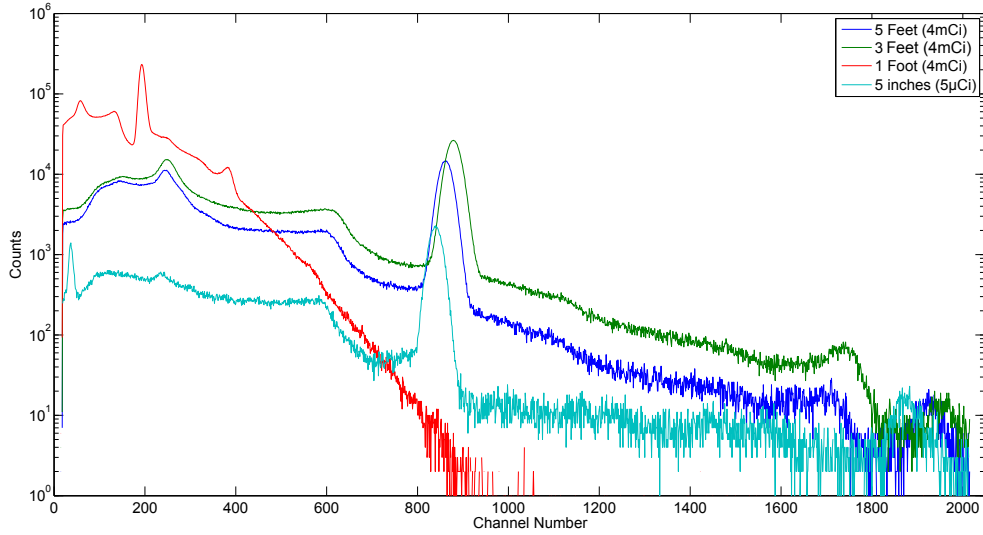
Figure 5.18: Comparison of analog CeBr$_3$ PHS of 4mCi ^{137}Cs at 5 feet, 3 feet, and 1 foot along with a 5μCi ^{137}Cs at 5 inches.
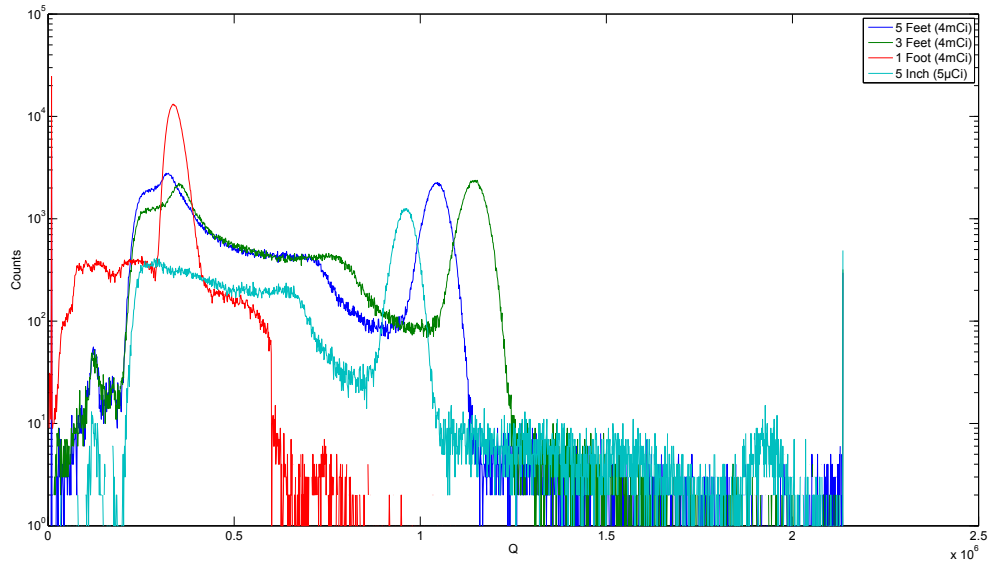
92

www.manaraa.com
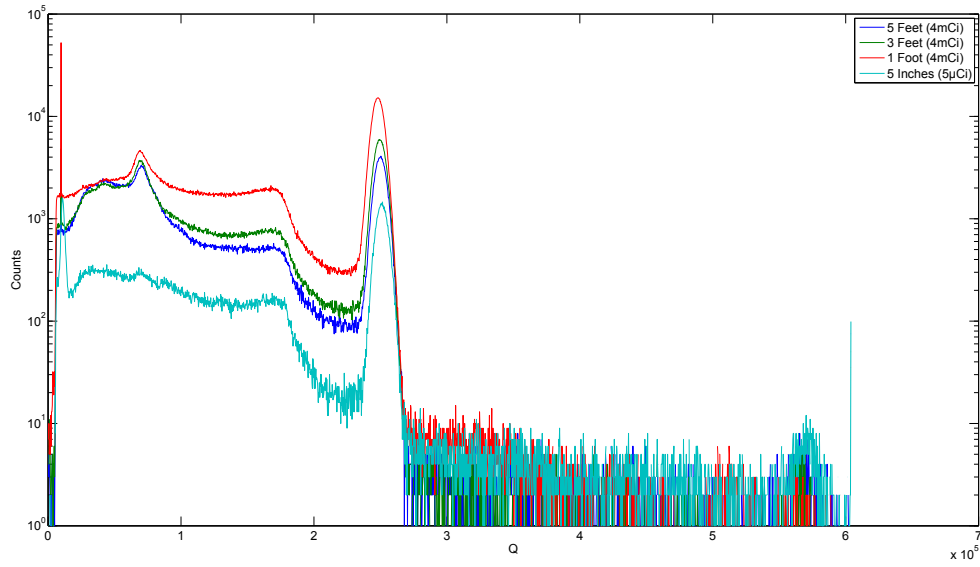
Figure 5.19: Comparison of fit CeBr$_3$ PHS of 4mCi ^{137}Cs at 5 feet, 3 feet, and 1 foot.

Table 5.5: CeBr$_3$ fit and analog PHS's FWHM and resolution at 662 keV with different source strengths of ^{137}Cs and varying source-to-detector distances.

	Analog PHS				Fit PHS			
Distance	5 inches	5 feet	3 feet	1 foot	5 inches	5 feet	3 feet	1 foot
Source Strength	5μCi	4mCi	4mCi	4mCi	5μCi	4mCi	4mCi	4mCi
FWHM (keV)	26.00	27.70	28.60	N/A	27.71	27.78	27.80	27.99
Resolution (%)	3.90	4.19	4.32	N/A	4.19	4.20	4.20	4.23

www.manaraa.com

Chapter 6

Conclusions

Digital pulse pileup deconvolution can be used in high count rate applications to acquire gamma-ray spectra with minimal distortion. Techniques to gather gamma-ray spectra like ours have applications in fusion research, active neutron interrogation, and oil well logging just to name a few.

Using a bright scintillator like $CeBr_3$ (68,000 photons/MeV) with a resolution of 3.9% at 662 keV, opposed to NaI(Tl) (38,000 photons/MeV) with a resolution of 6.4% at 662 keV; a high fidelity PHS can be created. Using digital pulse pileup deconvolution, $CeBr_3$ has an average pulse width of 150 ns, where the average pulse width from NaI(Tl) was above 1000 ns, which allows for more pulses to be captured with lower probabilities of pulse pileup.

The major accomplishments of this deconvolution algorithm developed and discussed in this thesis are:

- Incorporated a $CeBr_3$ scintillator to the nuclear pulse processing system

- Incorporating a 500 MS/s, 12-bit digitizer to the nuclear pulse processing system

- Digitized anode signals

- Deconvolve up to 3 pulse per trace window

94

- Analytical model that describes the pulse shape through physical properties of the scintillator and PMT

- All fit parameters are considered variables

  - Pre- & post-trigger baselines

  - Amplitudes

  - Pulse arrival times

  - Scintillation decay times

  - PMT decay times

- Trust-region reflective algorithm allows constrains on fit parameters

- Goodness-of-fit checks

  - Relative uncertainties of fit parameters allow for robust goodness-of-fit checks on variables

Digital pileup deconvolution was found to be very effective when high count rates saturated the pre-amplifier. Since our Canberra pre-amplifier had a maximum charge rate of 9μCoulombs$/s$, it was not the ideal pre-amplifier for working in high count rate environments[25]. The analog components used for this research worked very well in low to medium count rate environments with very little dead time. With these high count rates, our ORTEC amplifiers showed an increased baseline shift that manifested as gain shift into higher energies. This is not a problem with the digitizer since we are only sampling the detectors anode signal. We also saw in the NaI(Tl) detector the effects of high charge in the PMT from electron multiplication causing potential differences in the dynodes[10]. This was an issue that that was found during this research, but can also be corrected with the choice of the correct PMT for uses in high count rate environments.

The digitizer used in this research had a high sampling rate and voltage resolution, but created extreme dead times when transferring data between the buffers and onto hard disk.

Transferring data to the buffers took approximately 550 μs, and spilling data from the buffers to the hard disk took approximately 30 ms. With the implementation of a digitizer that can capture pulses with little or no dead time between sampling pulses and data transfer, there would be little no dead time associated with the digitizer. With respect to separating pulses, the pre-amplifier works well in low to medium count rate environments, where the digitizer can operate in very high count rates and has the ability to separate pulses arriving within a few nanoseconds of others with this algorithm.

Our algorithm contained models for a maximum of three pulses per trace window. We did find instances where there were more than three pulses in one trace window. This can be corrected with the addition of pulse models with more than three pulses, or by making the trace window length smaller to make less chances of pulse pileup. Another possibility is to do both solutions, decrease the trace window length and add more analytical models with greater number of pulses.

Digitizers are becoming faster and easier to implement into the nuclear pulse processing system. Being able to sample the detector anode signal every 2 ns gives the system the ability of very accurate and precise measurements. New scintillation materials like $CeBr_3$ have given rise to higher resolution room temperature gamma-ray spectroscopic systems. In conjunction, these two additions coupled with the pulse fitting algorithm described in this thesis have enabled medium resolution gamma-ray spectroscopy in high count rate applications without degradation of the PHS. The deconvolution algorithm was verified in low count rate environments, and showed high accuracy as the count rate increased. NaI(Tl) is not an ideal scintillation material in high count rates due to some characteristic properties of the material, but with the proper digitizer settings can create an accurate PHS. Experimentally $CeBr_3$ has performed very well in all count rate environments. Piled up pulses have been deconvolved allowing accurate PHS to be created with no shifting as seen in the analog PHS.

Future work will include a re-examination of the equation used for pulse fitting of $CeBr_3$. Research from others has shown promise in regards to the $CeBr_3$ pulse shape, but an exhaustive

search of the pulses and analytical models need to be worked out before proper fitting will be complete. Once these more accurate models are developed better relative uncertainties can be used for acceptance/rejection criteria of the pulses. Another change to the algorithm that has been noted is to change the way the baselines are used. After the first pulse, the post trigger baseline could be carried through another pulse if it arrives close in time. Experimentation on the proper way to implement this will be important. Adding more parameters to fit may just add unnecessary fitting times or lead to higher uncertainties in some values due to these parameters. The Pixie-500 is not the ideal digitizer for this work due to the high dead times associated with the transfer of data from the buffers to the hard disk, but its high sampling rate and resolution are ideal. Once a better fit has been found, a trial on real time pulse fitting can be explored. This will make a highly effective and efficient system for gathering PHS in high count rate environments.

Once a more complete analytical model has been developed a more accurate PHS will be created. This will also allow a closer look into the relative uncertainties values used for pass/fail thresholds on pulse parameters. With the proper pulse shape, these uncertainties will be able to be lowered given values that are more acceptable for pass/fail criteria. After these issues have been studied, building a prototype card that can be devoted to processing the digitized signals and fitting them will be next. From there the algorithm should be streamlined to remove excess processes that will not be necessary in a finished product. I expect once some of these things are accomplished, fitting times will decrease, relative uncertainties will be minimized, and very accurate PHS will be created from the data.

REFERENCES

[1] M. Nocente, M. Tardocchi, A.Olariu, and et al., "High resolution gamma ray spectroscopy at mhz counting rates with LaBr$_3$ scintillators for fusion plasma applications," *IEEE Transactions on Nuclear Science*, vol. 60, no. 2, pp. 1408–1415, 2013.

[2] H. Yu, "Compact neutron generators." `http://www.lbl.gov/tt/techs/lbnl1764.htm#minigenerator`, 2009. Accessed: May 2014.

[3] H. Yang, D. Wehe, and D. Bartels, "Spectroscopy of high rate events during active interrogation," *Nuclear Instruments and Methods in Physics Research A*, vol. A, no. 598, pp. 779–787, 2009.

[4] H. Yu, R. P. Gardner, J. Sun, and et al., "Accuracy and borehole influences in pulsed neutron gamma density logging while drilling," *Applied Radiation and Isotopes*, vol. 69, pp. 1313–1317, 2011.

[5] W. Guo, R. P. Gardner, and C. W. Mayo, "A study of the real-time deconvolution of digitized waveforms with pulse pile up for digital radiation spectroscopy," *Nuclear Instruments and Methods in Physics Research A*, vol. A, no. 544, pp. 668–678, 2005.

[6] G. F. Knoll, *Radiation Detection and Measurements 4th ed.* John Wiley & Sons, Inc., 2010.

[7] S. M. Robinson, S. Kiff, E. Ashbaker, and et al., "Effects of high count rate and gain shift on isotope-identification algorithms," *Nuclear Instruments and Methods in Physics Research A*, vol. A, no. 610, pp. 509–514, 2009.

[8] K. S. Shah, J. Glodo, W. Higgins, and et al., "CeBr$_3$ scintillators for gamma-ray spectroscopy," *IEEE Transactions on Nuclear Science*, vol. 52, no. 6, pp. 3157–3159, 2005.

[9] S. Koički, A. Koički, and V. Ajdačií, "The investigation of the 0.15s phosphorescent component of NaI(Tl) and its application in scintillation counting," *Nuclear Instruments and Methods*, vol. 108, pp. 297–299;, 1973.

[10] M. Tardocchi, L. Proverbio, G. Gorini, and et. al., "Gamma ray spectroscopy at high energy and high time resolution at JET," *Review of Scientific Instruments*, vol. 79, no. 10E524, 2008.

[11] ORTEC, *EASY-MCA-2k/8k*, 2014. `http://www.ortec-online.com`.

[12] W. Hennig, S. J. Asztalos, D. Breus, and et al., "Development of 500 MHz multi-channel readout electronics for fast radiation detectors," *IEEE Transactions on Nuclear Science*, vol. 57, no. 4, pp. 2365–2370, 2010.

[13] XIA, *User's Manual Digital Gamma Finder (DGF) Pixie-4*, January 2011.

[14] A. Vardi, "A trust region algorithm for equally constrained minimization: Convergence properties and implementation*," *Society for Industrial and Applied Mathematics Journal of Numerical Analysis*, vol. 22, no. 3, pp. 575–591, 1985.

[15] M. Branch, T. Coleman, and Y. Li, "A subspace, interior, and conjugate gradient method for large-scale bound-constrained minimization problems," *SIAM Journal on Scientific Computing*, vol. 21, no. 1, pp. 1–23, 1999.

[16] R. Byrd, R. Schnabel, and G. Shultz, "Approximate solution of the trust region problem by minimization over two-dimensional subspaces," *Mathematical Programming*, vol. 40, pp. 247–263, 1988.

[17] T. Steighaug, "The conjugate gradient method and trust regions in large scale optimization," *SIAM Journal on Numerical Analysis*, vol. 20, pp. 626–637, 1983.

[18] D. Sorensen, "Minimization of a large scale quadratic function subject to an ellipsoidal constraint," Tech. Rep. TR94-27, Rice University, 1994.

[19] T. Coleman and A. Verma, "A preconditioned conjugate gradient approach to linear equality constrained minimization," *Computational Optimization and Applications*, vol. 20, no. 1, pp. 61–72, 2001.

[20] Z. T. Bailey, "Pulse shape discrimination with the Pixie-500 data-acquisition system and EJ309 liquid organic scintillators," Master's thesis, North Carolina State University, Raleigh, NC, 2013.

[21] H. Photonics, *Photomultiplier Tubes and Assemblies for Scintillation Counting and High Energy Physics*, September 2012. `http://www.hamamatsu.com`.

[22] M. Nocente, M. Tardocchi, I. Chugunov, and et al., "Energy resolution of gamma-ray spectrometer of jet plasmas with a $LaBr_3$ scintillator detector and digital data acquisition," *Review of Scientific Instruments*, vol. 81, no. 10D321, 2010.

[23] K. Levenberg, "A method for the solution of certain non-linear problems in least squares," *The Quarterly of Applied Mathematics*, vol. 2, pp. 164–168, 1944.

[24] D. Marquardt, "An algorithm for least-squares estimation of nonlinear parameters," *SIAM Journal of Applied Mathematics*, vol. 11, pp. 431–441, 1963.

[25] I. Canberra Industries, *Model 2005 Scintillation Preamplifier*, 2014. `http://www.canberra.com`.

[26] W. Hennig, "Re: My thesis." Email to Noah Bullock, July 9, 2014.

[27] W. Hennig, "Re: Student research project." Email to Noah Bullock, April 24, 2014.

[28] W. Hennig, "Re: Student research project." Email to Noah Bullock, April 22, 2014.

[29] K. Reamer and K. Hanson, "Characterization of cerium(III) bromide scintillation detector as compared to sodium iodide," in *Proceeding to the annual INMM Conference*, July 2014. Accepted to be published.

[30] K. Hanson and K. Reamer, "Re: Data." Email to Noah Bullock, May 13, 2014.

[31] E. E. Limited, *51mm Photomultiplier: 9266B Series Data Sheet*, March 2013. `http://www.et-enterprises.com/`.

APPENDICES

Appendix A

Pixie-500 Settings

The Pixie-500 has a total of 32 buffers that can each hold 8K words of data. This allows for one long trace, or multiple shorter length traces. There are 3 settings for data readout mode known as "list mode run". The first setting is "1 event/spill." This digitizes one triggered event on the local I/O buffer and then transfers (or "spills") the local I/O buffer data to the external memory card. For a 700 ns trace length it takes approximately 14 μs to read into a buffer in the digital signal processor (DSP)[26]. During this 14 μs time the system will not capture any new pulses, so this is considered dead time. In this mode, once an event has been captured it is transferred into the buffer and then is takes approximately 550 μs to transfer the data in the buffer to external memory. The external memory can hold 256K words of data or 32 8K buffers. Once the data in external memory is full is takes approximately 30 ms to transfer data from the external memory to the hard disk [13]. The second setting allows for multiple events in each buffer. This allows for up to 32 events in the buffer. This setting was the most effective in our research to mitigate dead-time and collect the greatest number of pulses. The third method keeps 16 buffers in wait with 16 actively storing data. Once the first 16 are full, the second series of 16 starts storing data while the first group spills data out to hard drive. This method carries the same dead times for transferring data between modules, buffers, and hard disk. From experimentation it was found that an error exists in this list mode setting with

102

its final transfer of data. In a correspondence with one of the Pixie-500 inventors it was stated that, "The 16/16 mode is not really encouraged to use – we put it in at the request of one user and had a lot of trouble with it[27]."

The Pixie-500 also needs an input called the "polling time" that sets the time the buffers are checked against the list mode run. Setting a long polling time could let the system sit idle for large amounts of time, but setting too short of a polling time could cause problems in the user set running time. Since it takes the Pixie-500 a finite time to check the buffers, a value must be above that time to accurately reflect this task. The Pixie-500 also clocks itself by the polling tasks completed and its set value. If the polling time value is set too small it can cause the real time to be over the set run time input by the user[28]. In an experiment run with a polling time of 0.01 s the machine clocked 4 s, while the actual real time was approximately 13 s.

In an email from Dr. Hennig he states, "I would put a practical limit of the Pixie-500 as a "digitizer" to capture waveforms at about 50,000 traces per second for short traces[26]."

Another issue that was noticed using the Pixie-500 was the length of the runs that could be used. 5 minute runs in high count rate environments worked well, but at 10 minutes the data file would become corrupted before the last data transfer was completed from the buffers to the hard disk. Due to this only 5 minute runs were used to collect data from the Pixie-500.

IGOR Settings

- Trigger Tab

    - Rise Time (μs) = 0.048

    - Flat Top (μs) = 0.048

    - Enable Trigger = ✓

    - Good Channel = ✓

- Energy Tab

www.manaraa.com

- Rise Time (μs) = 3.584

- Flat Top (μs) = 0.704

- Advanced Tab

  - Histogram Control

    * "Enable"

    * Min. Energy = 0

    * Binning Factor = 1

    * Pileup Inspection = Disabled

  - Baseline Settings

    * Baseline Cut = 15

    * Baseline Averaging = 65534

Appendix B

CeBr$_3$ Characterization and PMT Data

This data was collected and analyzed by Kelsey Reamer[29, 30]. The source-to-detector distance was 8.5 inches. The measurements were taken on March 27, 2014. Energy calibration data points were between 81 keV and 1.33 MeV, the calibration sources used are shown in Table B.1. Fig.B.1 shows the characterization graphs, and Table B.2 gives the fit parameters for energy vs. channel and energy vs. resolution. Table B.3 give the fit parameters for the intrinsic efficiency of the detector.

Table B.1:   Calibration sources and original activity. All of these sources original activities were measured on February 15, 2013.

Calibration Source	Original Activity (μCi)
^{154}Eu	5.195
^{137}Cs	4.865
^{133}Ba	4.501
^{60}Co	4.545
^{22}Na	5.016
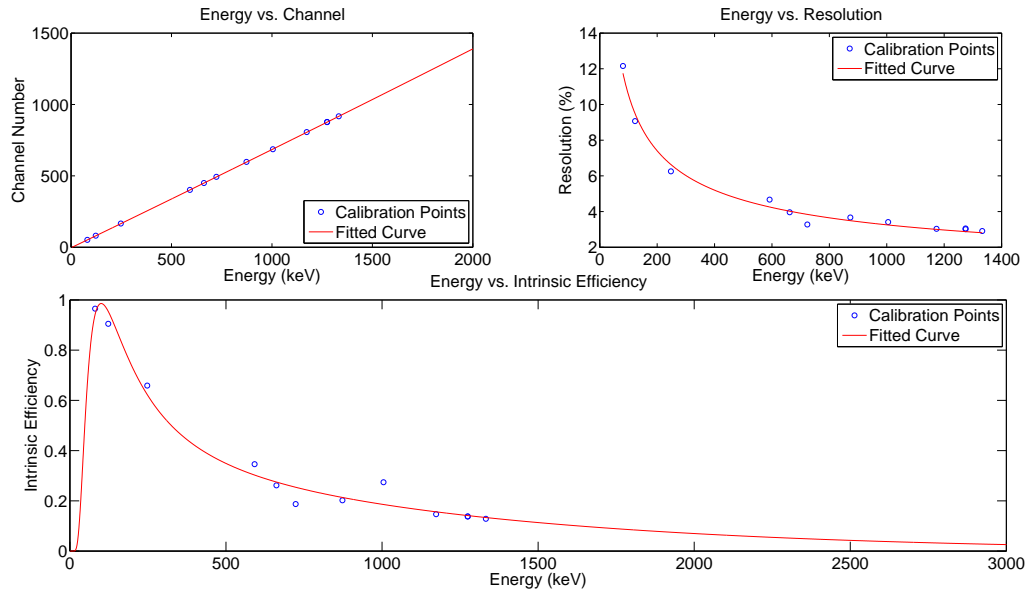
Figure B.1: CeBr$_3$ characterization data. Upper Left: Energy vs. Channel curve. Upper Right: Energy vs. Resolution curve. Bottom: Intrinsic efficiency curve.

Table B.2: Energy vs. channel and resolution fit coefficients and their goodness of fit values.

Fit Parameter	Energy vs. Channel	Energy vs. Resolution
	$y(x) = ax^2 + bx + c$	$y(x) = ax^b$
a	$8.66989854 \times 10^{-06}$	110.75260928
b	0.67919347	-0.51054637
c	-2.95686673	N/A
R^2	1.0	0.9882

Table B.3: Intrinsic efficiency fit coefficients and goodness of fit value.

Fit Parameter	Intrinsic Efficiency
	$y(x) = a \cdot \log(x)^4 + b \cdot \log(x)^3 + c \cdot \log(x)^2 + d \cdot \log(x) + e$
a	-0.06973108
b	1.68035289
c	-15.19397447
d	60.26441226
e	-88.06314625
R^2	0.9528

106

Figure B.2: CeBr$_3$ with calibration source setup to collect PHS to validate fitting algorithms PHS.

For the fitting code verification experiments, the CeBr$_3$ detector was setup as shown in Fig.B.2. The source-to-detector distance was 5 inches.

The data sheet supplied by Berkley Nucleonics Corporation gives some general information about CeBr$_3$ and some graphical data taken from their 25.4mm (diameter) X 25.4mm (long) CeBr$_3$ detector. An important graph to note is on the bottom right. It shows the background spectrum taken shows no significant intrinsic gamma-ray lines are associated with the crystal.

BNC

High Resolution, Low Background CeBr₃ Scintillation Crystals

$CeBr_3$ scintillation crystals offer an alternative to NaI(Tl) for high resolution gamma spectrometric applications. Above a gamma energy of about 200 keV, the energy resolution of $LaCl_3$:Ce is superior to NaI(Tl). CeBr3 scintillation detectors do not suffer from the intrinsic background typical for Lanthum Halide detectors like $LaCl_3$:Ce and $LaBr_3$:Ce

Properties

Density	:	5.2 g / cc
Emission wavelength	:	380 nm
Decay time	:	17 ns
Radiological background	:	Negligible
Hygrosopic	:	YES
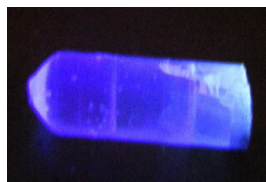
	NaI(Tl)	CeBr₃
Relative Photoelectron Yield	100	125

Energy [keV]	Typical Energy Resolution [%]	
30	18.	22
60	12	15
81	11	13.5
122	9	11
356	8	5
662	6.5	4
1332	4.9	3
2600	4.0	2
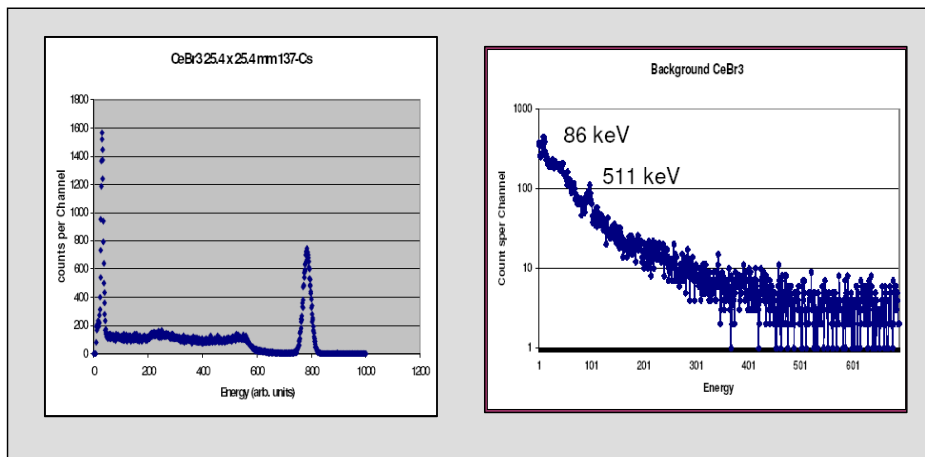
*** Note that no significant scintillation crystal related lines are observed in the background spectra**

SCIONIX Dedicated Scintillation detectors SCHOTT glass made of ideas

B.1   Hamamatsu R6231 PMT

Our CeBr$_3$ used a Hamamatsu R6231 PMT[21]. It has 8 stages of box and linear focused type dynodes. It has a maximum operating voltage of 1500V. Hamamatsu suggests at operating their PMTs at 100V-300V below the maximum operating voltage to omit field emission caused dark currents[21]. The typical dark current from all sources is 2 nA, with a maximum dark current of 20 nA[21]. Hamamatsu gives two values with respect to pulse linearity, $\pm 2\%$ and $\pm$ 5%. Pulse linearity is the proportionality between input light amount and output current in pulse operation mode.[21]. Pulse linearity at $\pm 2\% = 5\ mA$, and $\pm 5\% = 10\ mA$. The time it takes the anode output pulse to increase from 10% maximum amplitude to 90% maximum amplitude is known as the rise time. The R6231 has an anode 10% - 90% rise time of 8.5 ns. The amount of time between the arrival of the light pulse at the photocathode and the peak anode output amplitude is known as the electron transit time (transit time). The R6231 has a typical transit time of 48 ns. The transit time spread (TTS) is a variation in transit times between individual pulses and is measured by the FWHM of the frequency distribution of transit times[21]. The R6231 has a typical TTS of 6.9 ns. For more details and characteristics of the Hamamatsu R6231 PMT please read Ref. [21].

Appendix C

NaI(Tl) Detector Characterization Data

This data was collected and analyzed by Kalene Hanson[29, 30]. The source-to-detector distance was 8.5 inches. The measurements were taken on March 21, 2014. Energy calibration data points were between 81 keV and 1.33 MeV, the calibration sources used are shown in Table C.1. Fig.C.1 shows the characterization graphs, and Table C.2 gives the fit parameters for energy vs. channel and energy vs. resolution. Table C.3 give the fit parameters for the intrinsic efficiency of the detector.

Table C.1:   Calibration sources and original activity. All of these sources original activities were measured on February 15, 2013.

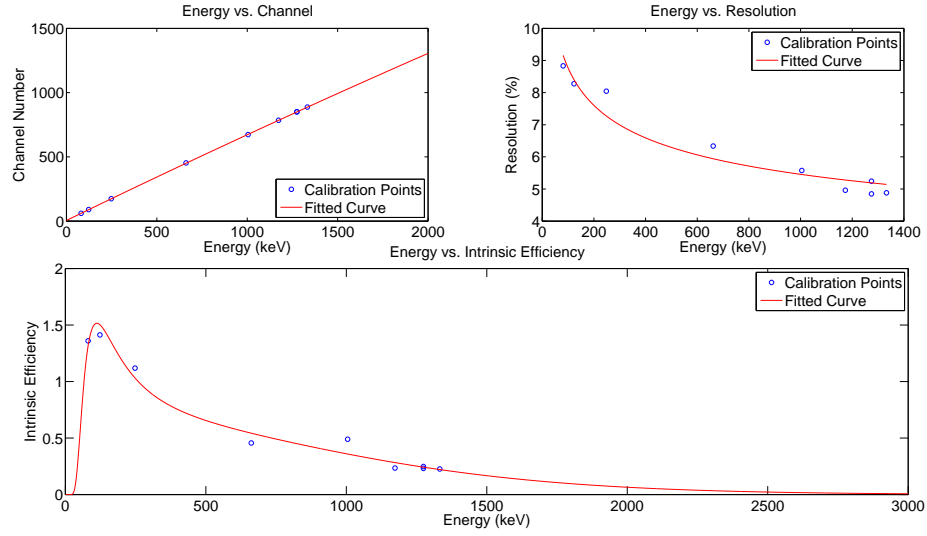| Calibration Source	Original Activity (μCi)
^{154}Eu	5.195
^{137}Cs	4.865
^{133}Ba	4.501
^{60}Co	4.545
^{22}Na	5.016

Figure C.1: NaI(Tl) characterization data. Upper Left: Energy vs. Channel curve. Upper Right: Energy vs. Resolution curve. Bottom: Intrinsic efficiency curve.

Table C.2: Energy vs. channel and resolution fit coefficients and their goodness of fit values.

Fit Parameter	Energy vs. Channel	Energy vs. Resolution
	$y(x) = ax^2 + bx + c$	$y(x) = ax^b$
a	$-1.69058280 \times 10^{-05}$	22.65880457
b	0.68389580	-0.20609809
c	5.90034455	N/A
R^2	1.0	0.9436

Table C.3: Intrinsic efficiency fit coefficients and goodness of fit value

Fit Parameter	Intrinsic Efficiency
	$y(x) = a \cdot \log(x)^4 + b \cdot \log(x)^3 + c \cdot \log(x)^2 + d \cdot \log(x) + e$
a	-0.16015098
b	3.71657103
c	-32.25978679
d	123.47711553
e	-175.02488942
R^2	0.9648

Figure C.2: NaI(Tl) with calibration source setup to collect PHS for validation of the fitting algorithms PHS.

For the fitting code verification experiments, the NaI(Tl) detector was setup as shown in Fig.C.2. The source-to-detector distance was 5 inches.

C.1   ET Enterprises 9266B PMT

Our ORTEC 905-3 NaI(Tl) used an ET Enterprises Limited (ETL) PMT[31]. It has 10 stages of linear focused type dynodes. It has a maximum operating voltage of 2000V. The typical dark current from all sources is 0.3 nA, with a maximum dark current of 3 nA[31]. ETL gives one value with respect to pulse linearity, $\pm$ 5%. Pulse linearity is the proportionality between input

light amount and output current in pulse operation mode.[21]. Pulse linearity at $\pm 5\%$ in divider A = 30 mA, and divider B = 100 mA. The 9266B has a multi electron rise time = 4 ns. The amount of time between the arrival of the light pulse at the photocathode and the peak anode output amplitude is known as the electron transit time (transit time). The 9266B has a typical transit time of 40 ns. The spread in the transit time is noted as the multi electron FWHM. The 9266B has a typical multi electron FWHM of 6.5 ns. For more details and characteristics of the ETL 9266B PMT please read Ref. [31].